POLITECNICO DI MILANO

Ph.D. Course in Environmental and Infrastructure Engineering

Department of Environmental, Hydraulic, Infrastructures and Surveying Engineering

VALIDATION AND FUSION OF DIGITAL SURFACE MODELS

Tutor: **Prof. Fernando Sansò**

Supervisor: **Prof.ssa Maria Antonia Brovelli**

Coordinator: **Prof. Fernando Sansò**

Ph.D. Thesis by

Sara Lucca

Student Id.: 738791

XXIV Cycle (2009-2011)

Contents

Introduction

In the latest years, acquisition and manipulation techniques for Digital Surface and Terrain Models (DSM and DTM) are improving rapidly, allowing the production of data with high resolution and accuracy; on the other hand the development of new sensors allowed the survey of wide portion of the Earth surface, providing free products such as the SRTM DSM and the ASTER global DEM.
Depending on the acquisition source the DEM may have different characteristics; in particular they can have various spatial resolutions and vertical precisions: for example DEMs from LiDAR or photogrammetric surveys are more dense and more accurate than DEM from SAR technologies or global DEMs.
The availability, on the same area, of different kind of models gives the possibility to combine different information to obtain more reliable models or to improve an existing one. However, it is advisable, before attempting to merge different information, to validate the models, that is to assess their accuracy; this step is necessary to know how much a model is reliable, and afterwards the precision of the model can be used as a weight in the merging procedure.
This work addresses to all these topics, dealing with DEM creation and validation. All the models under analysis cover an area around Como (Italy); the availability of data created with different techniques and characterized by different resolutions and accuracies permitted to set up and test various fusion procedures.
To validate the DEMs in the area two procedures were carried on in sequence: at first, each model was internally validated and its outliers were removed, then they were compared to a model representing the ground truth to assess their accuracies. The ground truth, in our case, is represented by a DSM obtained from a LiDAR survey; a raw LiDAR dataset, available in the area, was filtered with different software to produce a high resolution DSM and DTM.
Once validated, it is possible to merge the information provided by different models; the work proposes two main fusion strategies: the former consists in a weighted average fusion tested with different weights, assuming either

the accuracy of the model to be homogeneous or different accuracies of the model according to the terrain morphology. Those accuracies are estimated in different areas, previously classified according to their slope gradient and aspect. The latter procedure is based on the stochastic collocation prediction method tested in areas with different morphologies.
The whole procedure was at first tuned on to the SRTM and ASTER DSMs; once established, it was applied to radargrammetric data to assess which strategy is the most advisable to generate a unique DSM from a couple of dataset, one from ascending orbits and the other from descending ones.

The structure of the thesis is the following:

Chapter 1 presents a general introduction on digital elevation models, focusing on their acquisition sources, on the evaluation of their accuracies and on their derived products. The SRTM and the ASTER missions and products are described too.

Chapter 2 is focused on LiDAR data filtering. Two filtering procedures are taken in consideration, the former implemented within GRASS GIS, the latter within TerraScan: after a theoretical description of the algorithms, the results obtained from the two approaches when applied to the dataset covering Como are compared to assess their accuracies. The latest part of the chapter focuses on the interpolation method used to produce a DSM and a DTM from the LiDAR filtered datased.

Chapter 3 describes the digital model validation step and the results obtained on the available DEMs. Two validation approaches are applied to the data under analysis: an internal and an external one, the former procedure is performed using an algorithm developed within the GRASS GIS open source software, the latter is performed by comparing the digital elevation models with a LiDAR DSM considered as ground truth.

Chapter 4 presents the application of a two way ANalysis Of VAriance (ANOVA) to the SRTM and ASTER DSMs. The aim of this analysis is to detect if the models depend on the terrain characteristics, in particular on slope gradient and slope aspect. The results provide further information for validating the models and are used in the fusion step too.

Chapter 5 is dedicated to data fusion procedure. Different approaches are described, from both a theoretical and a practical point of view; in particular two main methods are considered: a weighted average and a collocation

approach. For both of them results in terms of DSM accuracy are provided.

Chapter 6 presents the validation and fusion steps applied to radargrammetric data provided by the La Sapienza University of Roma (Italy). In the former sections the radargrammetric method is described, while in the latter ones the results on two test regions are presented.

Chapter 1

Digital Elevation Model

A DEM can be defined as a digital model representing a surface; its applications are wide, in fact it may be useful for landscape modeling, city modeling and visualization applications, or for flood or drainage modeling, land-use studies, geological applications etc... In the former part of this first chapter the most common sources for DEM generations are described, while the latter part is more focused on the DEM accuracy assessment and on the possible DEM derivative maps.

1.1 Data sources

Digital Elevation Models are generated by means of different technologies; in this section the most common data source are described.
The process of data surveying can be active or passive: the former means that the instrument obtains directly ground point coordinates; in the latter modality the instrument obtains various information (e.g. ground image) from which, after some elaborations, the point coordinates are extracted [Li et al., 2005].
Once a dataset of ground point coordinates is obtained it is necessary to interpolate it to generate a continuous DEM surface; different methods are available to obtain a dataset of points:

- cartography;
- photogrammetry;
- airborne LiDAR;
- SAR interferometry and radargrammetry.

In the following sections the different technologies will be taken in consideration; the last two sections will be focused on the description of the SRTM and ASTER DEM that are worldwide available.

1.1.1 Cartographic data source

Among the different sources to develop digital terrain model one of the most adopted in the past years is the cartographic one. Practically two approaches exist: vector-based line following and raster-based scanning, both can be either manual or automatic.

The former procedure is the most used, the digitization can be manually obtained by a mechanical based system or a solid-state digitizing tablet.
Contour lines are traced thanks to a cursor with cross-hairs, the operator may choose between recording each relevant position pressing a button or following the lines and then recording point coordinates in fixed time or space interval; the former way is more tedious but its advantage is that the operator has the total control on the operation, the latter is quicker and more dynamical but often the results are not compliant to the original data.
Vector digitization is also available in semi-automated mode using special digitizer systems, however manual intervention is still needed to import contour elevation value, to guide the system in packed contours and cliff areas, etc.

Cartographic methods	
Vector line following	Manual: - user chooses which coordinates to save - dynamical mode: coordinates saved at fixed time/distance Semi automated: Specific digitizer + user intervention
Raster scanning	Manual: user follows the lines on the screen Automated: algorithm performs - noise detection - contour detection, binarization and skeletonization - contour vectorization

Table 1.1: Cartographic data source

Raster scanning procedure instead imports original data as raster maps by using a flat-bed or a drum scanner.
Once the map is imported the vectorization phase can be carried on both manually or automatically: in the manual operation the user, working with a dedicated software, simply follows the lines on the screen and saves them in a vector format. The automated procedure is instead executed with algorithms usually following these steps (eg. Aumann et al. 1991, Goncalves et al. 2002, Hind et al. 1999):

- noise removal;
- contour detection, binarization and skeletonization;
- contour vectorization.

In Table 1.1 the different digitizing methods are summarized.

1.1.2 Photogrammetric data source

Photogrammetry allows 3D object reconstruction from stereo pair taken during a survey; photogrammetry can be space, aerial and terrestrial, for DEM generating purpose in the following only the space and aerial methods will be considered. Stereo pair defines a couple of images of the same area taken in two slightly different time so that they have a certain percentage of overlap; in the overlapping area it is possible to reconstruct 3D models: in the aerial case usually the overlap is set to 60% degree in the flight direction and 30% between the flight strips (Figure 1.1).
Each photograph is characterized by six orientation elements (three angular and three translation), once these elements are known it is possible to compute ground point coordinates.

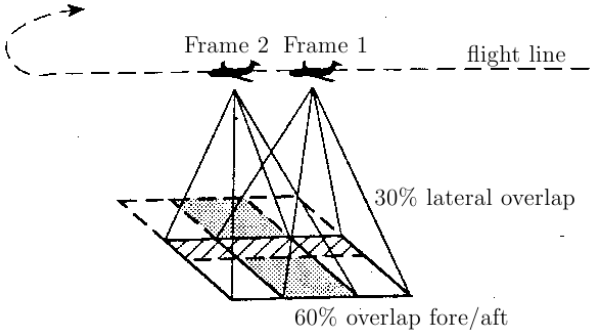

Figure 1.1: Overlap in flight direction and between strips

In analogue photographed the two images constituting the stereo pair are put on two projectors -identical to the camera used in the survey- which position and orientation are restored to the one of the survey, then the light rays projected through the two photographs will intersect and generate a 3 model (stereo model) in the air. Once the model is obtained the user is able to measure 3 points on the stereo model.

In analytical photographed the relation between image point, the corresponding ground point and the projection center is described by the collinearity equation, an analytical condition specifying that the three points belong to a straight line. The collinearity equation contains terms that depend on the six orientation parameters; if they are known and the image coordinates are measured in both the images of the stereo pair (m_1 and m_2 in Figure 1.2) the ground coordinates of the point (M in Figure 1.2) can be computed using the collinearity equation.

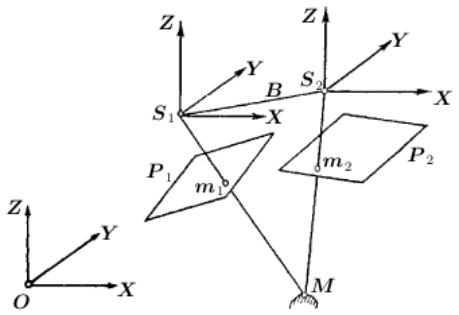

Figure 1.2: Stereo model from two images

In digital photogrammetry images are in digital format, coordinates are determined as row and column of the corresponding pixel. Given a pixel in one image the system automatically finds the related pixel in other images (image matching). The digital photogrammetry can be both aerial and satellite depending on the instruments used: in the former a digital camera is installed into an aircraft while in the latter the instrument is mounted on a satellite; in the next section the satellite photogrammetry will be described.

Satellite photogrammetry In the aerial photogrammetry the survey and so the flight plan is defined ad-hoc with respect to the area characteristics, in the satellite photogrammetry the mission is designed once, so its design is subjected to the final use of the images (photogrammetry, remote sens-

ing, weather forecasting etc...) [Mikhail and Bethel, 2001] . The satellites used for remote sensing or photogrammetry have sun-synchronous orbits, so the satellites always passes over a point at the same local solar time, so for each latitude the position of the Sun is the same in the same season (Figure 1.3); the height with respect to the Earth surface is around 450-850 km.

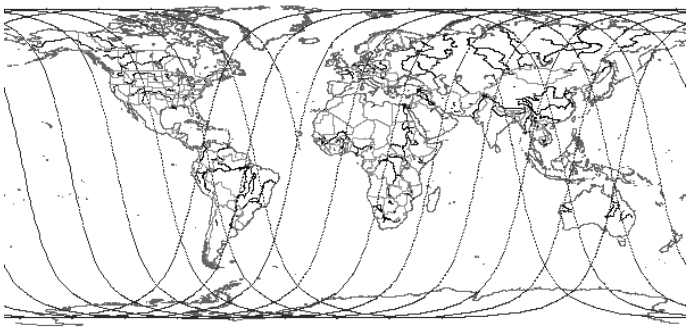

Figure 1.3: Example of sun-synchronous orbit

The sensors used on the satellite are passive and the digital one can be of different types: frame cameras, electro-mechanic (MSS MultiSpectral Scanner on Landsat, Thematic map on Landsat 7) and linear CCD (SPOT). Some satellite are able to steer the sensor in the cross-track and along-track direction; so the area covered is expanded (the time between overflight decreases) and the stereo coverage acquisition is enabled. Some sensors are characterized by very high resolution such as the IKONOS 2, Quickbird, Eros-A. A DEM obtained from the ASTER satellite photogrammetry mission, described in detail at the end of the data source section, is used in this work.

1.1.3 Airborne LiDAR data source

Laser scanning based systems are now widely used thanks to their high resolution and reliability; LiDAR system are both aerial and terrestrial but for DEM generation only the former is used [Ackermann, 1999].
LiDAR system is an integration of three different sensors mounted on an aircraft (Figure 1.4): laser emitter/receiver, GPS and INS/IMU needed to determine position and aircraft attitude (Figure 1.5[1]). LiDAR is an active system, electromagnetic energy is sent off and the energy reflected from the

[1]From C. Brenner presentation "Aerial laser scanning" for International Summer School "Digital Recording and 3D Modeling" Crete, Greece, 24-29 April 2006

terrain is recorded; at the end of the survey a correspondence between GPS coordinates, time of emission and intensity of back scattered energy can be obtained.

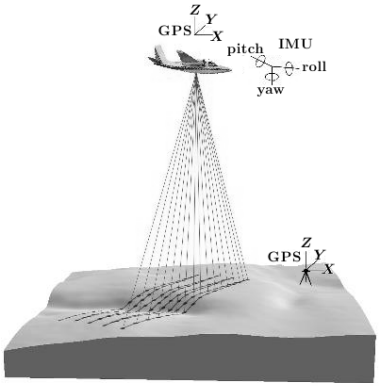

Figure 1.4: LiDAR system

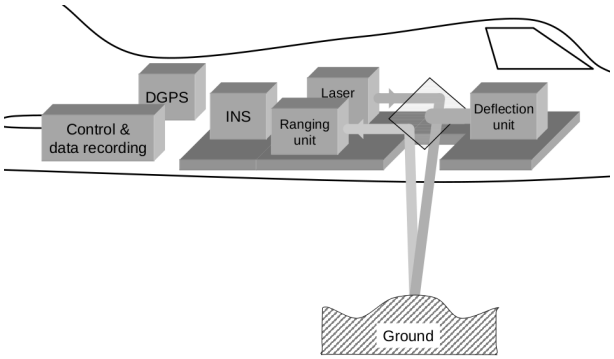

Figure 1.5: Laser unit, GPS and INS/IMU system

Two LiDAR typology exist: pulse and continuous laser emission [Baltsavias, 1999a]; in the former, commonly used, laser pulses are emitted at regular time interval, the latter uses a continuously emitted signal basing the computation on phase difference between emitted and received ray beam.
In pulse laser the direct measure correspond to the time elapsed between laser emission and come back after terrain reflection; the distance R between aircraft and ground is easily obtained considering the speed of the beam c (equal to light speed).

$$R = \frac{t_{travel}}{2} c \tag{1.1}$$

The emission system sends off a laser beam only when all the previously emitted ray have been recorded after ground reflection, from this derives a condition concerning emission frequency (f): the time elapsed from the emission and the reception must be lesser than signal period.

$$\frac{2R}{c} < \frac{1}{f} \Rightarrow R < \frac{c}{2f} \Rightarrow f < \frac{c}{2R} \tag{1.2}$$

For example, if the flying heigh R is 1000 m, the maximum frequency allowed is 150 kHz.
The direct consequence of this condition is the need of a compromise between flying height and point density:

- high flying height $\rightarrow$ low point density: few wide strips;
- low flying height $\rightarrow$ high point density: high number of strips.

In continuous emission the signal may be sinusoidal, so the time of travel depends on phase difference (ϕ) between transmitted and received signal; the distance between aircraft and ground is computed as in the pulse system.

$$t_{travel} = \frac{\phi}{2\pi}\frac{1}{f} \Rightarrow R = \frac{t_{travel}}{2}c = \frac{\phi}{4\pi}\frac{c}{f} \tag{1.3}$$

The non ambiguity condition between signal emitted and received depends only upon the wavelength λ.

$$R < \frac{\lambda}{2} \tag{1.4}$$

Different sensor mechanisms are available [Wehr and Lohr, 1999, Baltsavias, 1999c], they have various differences, in particular they draw different scanning path on the ground (Figure 1.6[2]):

- oscillating mirrors produce a Z-shaped path in bi-directional scansion, in an uni-directional one they draw parallel lines;
- rotating Polygons draw parallel lines on the ground;
- mutating mirror (Palmer scan) creates an elliptical shape so some points are surveyed two times;
- fiber switch scansion produces parallel lines. The mechanism is present only in the TopoSys systems.

[2]From C. Brenner presentation "Aerial laser scanning" for International Summer School "Digital Recording and 3D Modeling" Crete, Greece, 24-29 April 2006

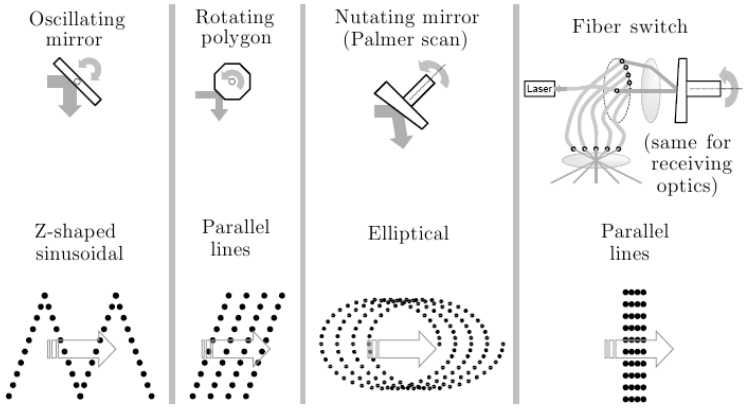

Figure 1.6: LiDAR system

Table 1.2 contains details about different LiDAR system.

System	**Optech ALTM Orion M200**	**Riegl VQ-580**	**TopoSYS Falcon II**
Laser	1064 nm	Near IR	1540 nm
Max Altitude	2500 m	1200 m	1600 m
Measures	Up to 4 pulses	Practically unlimited	First and last
Pulse frequency	Max 200 KHz	Max 380 KHz	83 KHz
Beam Divergence	0.25 mrad	0.2 mrad	0.5 mrad
Scanning Mechanism	Oscillating mirror	Rotating polygon mirror	Fiber switch
Ground path	Z-shaped	Parallel lines	Parallel lines

Table 1.2: LiDAR surveying system

Once acquired, a LiDAR dataset is elaborated to obtain link between point coordinates, intensity of energy reflected and return number. In fact a laser beam is characterized by a certain diameter, so when it reaches the ground it can produce multiple reflection; building roofs and vegetation canopy will reflect firstly the ray while the ground will be the last reflecting surface.
Typically the recording instrument is able to detect at least the first and the last beam reflection, but with technology improvements some systems are able to record also middle reflections (that correspond mostly to vegetated area).

To obtain data suitable to DSM and DTM generation a LiDAR dataset needs to be classified to differentiate between points belonging to terrain and to objects (vegetation, buildings...).
Various filtering algorithms were developed with different characteristics: filters can use different kind of input (raw cloud data or the result of a rasterization procedure) and can perform the analysis in one step or in an iterative way. Another difference between algorithms consist in the number of points classified each time because the classification can be performed in three modality: one point can be a function of another point or a function of many points and many points can be function of a group of neighbouring points. Another characteristic of filter consist in the information used; in fact some filters use only the last pulse of LiDAR data while others use also the first one [Brovelli and Cannata, 2002, Tarsha-Kurdi et al., 2006]. Some filters can use other kind of information like aerial images, existing DEMs [Bretar and Chehata, 2007, Matikainen et al., 2007, Secord and Zakhor, 2007], land use maps, cadastral maps and a wide variety of multispectral data [Steinle and Vogtle, 2001].
Tovari and Pfeifer identified four algorithm typologies [Tovari and Pfeifer, 2005]:

- morphological or slope based algorithms: they use height differences to recognize points belonging to objects. The classification is performed using a threshold that determines the admissible height difference between two neighbour points such that one can be considered as bare earth. This approach can use also a fixed slope or gradient threshold values instead of height differences;

- progressive densification algorithms: these filters at first identifies some points belonging to the ground and then, depending on those, classify as ground more points. Usually the points used as seeds are the ones with lower height. Additional ground points are determined by investigating their neighbour in the reference surface;

- surface based algorithms: these filters use a parametric surface that iteratively approaches to hypothetical bare earth. The surface is modified depending on the influence of the individual input points;

- clustering-Segmentation algorithms: these filters are based on the idea that a cluster of points belongs to an object if it has height values greater than its neighbours. In these cases the classification is performed in two steps: at first a segmentation is carried out and then the segments are divided in different classes depending on the differences in height between segments.

Airborne laser scanner and photogrammetry are often compared to find the better technology for aerial survey; their major differences are summarized in Table 1.3 [Baltsavias, 1999b].

	LiDAR	**Photogrammetry**
System	Active	Passive
Sensor	Point sensors with polar geometry	Frame or linear sensors with perspective geometry
Coordinates acquisition	Direct	Indirect
Images	None or low quality one	High quality with multispectral capabilities
Technology	Developing	Mature
Automation	High	Low
Flight hours	More, it can work theoretically 24h a day	Less, works better when trees have no leaves

Table 1.3: LiDAR vs Photogrammetry

1.1.4 SAR interferometry and radargrammetry data source

Real aperture radar (RAR) and synthetic aperture radar (SAR) are side-looking systems; the microwave pulse beam is radiated at an angle orthogonal to the flight direction.
The length of RAR antenna determines the resolution in the azimuth direction (along-track). Increasing the length also the resolution in that direction will increase. In SAR a combination of received signal is used to synthesize a very long antenna; it was created to remove the spatial resolution dependency of RAR on the antenna length. Synthetic aperture radar is widely used to acquire images very sensitive to terrain variation; this is the base of three techniques:

- radargrammetry acquires DEM through parallax measurement;
- interferometry is based on phase shift between two echoes;
- radarclinometry acquires DEM through shape from shading, it uses a single image obtaining not accurate height measures.

In radargrammetry a 3D stereo model is generated using two SAR images collected with the unique side looking geometry keeping the SAR intensity

information only.
Different studies found that DTM generation from radargrammetry is affected by the following factors [Toutin, 1999, 2002b]:

- terrain features (e.g topographic slope);
- geographical conditions;
- geometric distortions in relation to radar looking angles;
- intersection angles.

SAR was developed to improve the resolution of traditional radar based on Doppler frequency shift caused by the relative movement between the antenna and the target [Toutin and Gray, 2000]. Like LiDAR SAR is an active sensor, it receives and records echoes reflected by the target mapping echoes intensity in a grey scale image. Unlikely photogrammetry SAR is able to work day and night with every weather condition.

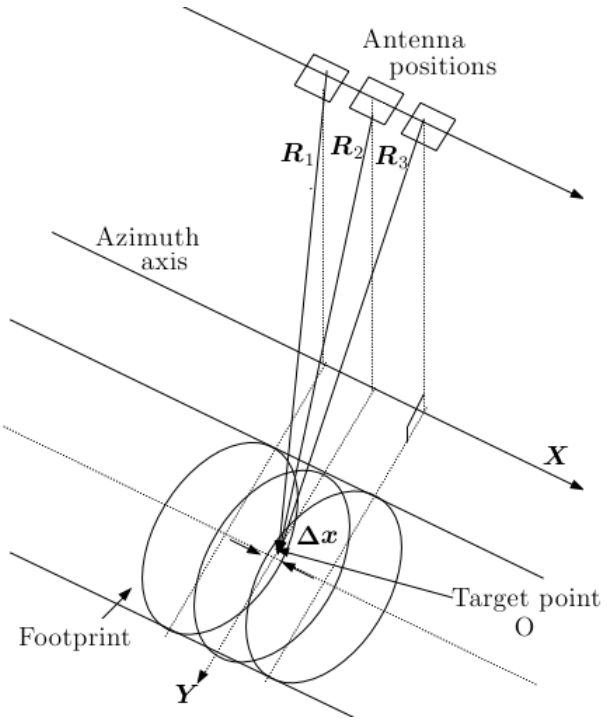

Figure 1.7: SAR imaging geometry

Figure 1.7 displays the imaging geometry for a SAR used to take a side look image of the ground: assuming a real radar with aperture length L moves in

the three positions (1, 2 and 3) to acquire data about target O then the slant range R from O to the antenna varies from R_1 to R_2 and then to R_3. The variation of R causes the frequency shift of the backscattered echo from target O. It's then possible to sharp the azimuth resolution (footprint intersection area Δx in Figure 1.7) by precisely measuring the phase delay of the received echoes; the azimuth resolution of a SAR depends only on the length of the real aperture of an antenna L (and not on the range R or on the wavelength λ).

$$\Delta x = \frac{L}{2} \tag{1.5}$$

In interferometric SAR a pair of images of the same area taken in two slightly different times is used to create an interferogram ($\phi(x, r)$) and the phase difference recorded can be used to derive a topographic map. Figure 1.8 shows the geometry of SAR images to evaluate the height of the target point O.

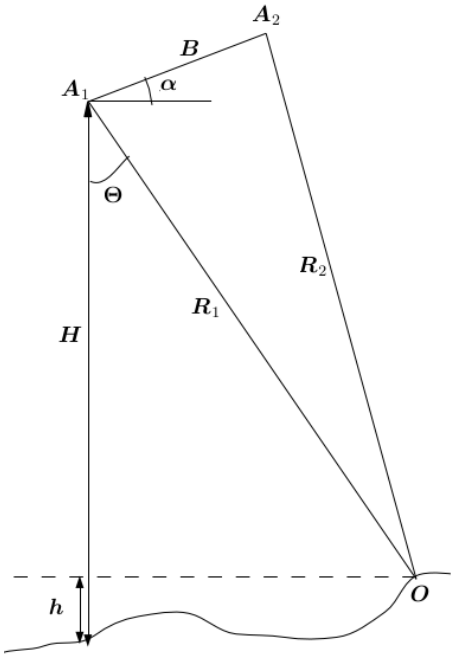

Figure 1.8: SAR geometry for heighting

Defining $\widehat{S}_1(x, r)$ as the image taken at point A_1 with its phase component $\Phi_1(x, r)$ and $\widehat{S}_2(x, r)$ as the one taken at position A_2 with phase component $\Phi_2(x, r)$ it is possible to obtain an interferogram $\phi(x, r)$ subtracting the two phase components. In fact, knowing that the phase delay is directly

proportional to the slant range from the antenna to the target point:

$$\Phi = \frac{2\pi R}{\lambda} \tag{1.6}$$

$$\phi = \Delta\Phi = \Phi_2 - \Phi_1 = \frac{2\pi Q \delta R}{\lambda}. \tag{1.7}$$

The parameter Q is equal to one if the two antenna are mounted on the same flying platform, otherwise, if the two images are acquired at two different places by the same radar Q it is equal to two. From $\phi(x, r)$ it's possible to calculate the slant range difference δR between R_1 and R_2:

$$\delta R = R_1 - R_2 = \frac{\lambda}{2\pi Q}\phi \tag{1.8}$$

When $B \ll R_1$ the difference can be approximated by the baseline component in the slant direction (Θ is the side looking angle and α the one of the baseline with respect to the horizontal line).

$$\delta R \approx B_{\parallel} = B sin(\Theta - \alpha) \tag{1.9}$$

$$sin(\Theta - \alpha) = \frac{R_1^2 + B^2 - R_2^2}{2BR_1} = \frac{R_1^2 + B^2 - (R_1 + \delta R)^2}{2BR_1} \tag{1.10}$$

At the end the height of point O is determined by:

$$\Theta = sin^{-1}\left(\frac{\lambda\phi}{4\pi B}\right) + \alpha \tag{1.11}$$

$$h = H - R_1 cos\Theta \tag{1.12}$$

In InSAR the key points are:

- the precise computation of phase difference;
- the precise estimation of the baseline B.

For DEM generation (Figure 1.9[3]) two images are used, one referred to as the master image and the other as the slave one; these have different orientations since the antenna might have different attitudes at different times. Because of that, they need to be converted in the same coordinate system and resampled to have pixel of equal size (co-registration process).

[3]From http://www.geocomputation.org/1999/084/gc_084.htm

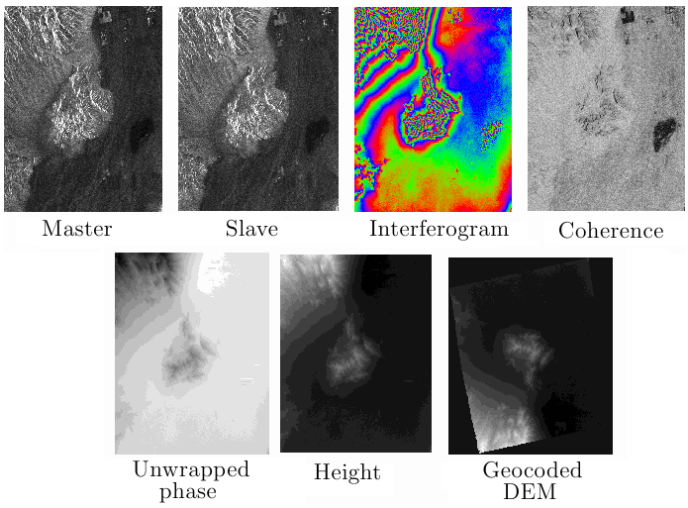

Figure 1.9: Example of DEM generation with SAR

The next step is the interferogram production, the value for each pixel is computed multiplying the two conjugate complex number ($\widehat{S}_1(i)$ and $\widehat{S}_2^*(i)$):

$$G = \sum_{i=i}^{N} \widehat{S}_1(i)\widehat{S}_2^*(i) \tag{1.13}$$

$$\phi_0 = tan^{-1}[G] \in [-\pi, \pi] \tag{1.14}$$

where N is the total number of pixels in the moving window (for phase noise reduction).
Practically the difference δR corresponds to a number of whole waves (ϕ_u) plus a residual (ϕ_0):

$$\phi = \phi_u + \phi_0 = \phi_0 + 2\pi k \tag{1.15}$$

In the equation k correspond to the number of microwave cycles, however this value cannot be determined; this cycle ambiguity problem is solved thanks to the phase unwrapping process (some example in Fornaro et al. 1996, Davidson and Bamler 1999), which makes use of phase difference information in neighbouring pixels.

1.1.5 SRTM DEM

The Shuttle Radar Topography Mission (SRTM) was a joint project of the National Aeronautics and Space Administration (NASA), the German

Aerospace Center (DLR) and the Italian Space Agency (ASI). The mission's objective was the acquisition of a digital elevation model of all land between 60 ° North latitude and 56 ° South latitude (about 80% of Earth's land surface). The cartographic products derived are a global high-quality DEM at resolution levels of 1 (approximately 30 m by 30 m) and 3 arcseconds (approximately 90 m by 90 m) obtained averaging nine values at 1 × 1 arcsecond; at the present the 1 arcsecond data are available only for the USA, while the 3 arcseconds ones are available in every area with the following accuracies (at 90% confidence level):

- linear vertical absolute height error: less than 16 m;
- linear vertical relative height error: less than 10 m;
- circular absolute geo-location error: less than 20 m;
- circular relative geo-location error: less than 15 m.

The relative accuracy describes the error in a local 200-km scale while the absolute value stands for the error budget throughout the entire mission.
The dataset was acquired with the same sensor in a single mission and was produced with a single technique: synthetic aperture radar (SAR) interferometry [Rabus et al., 2003].
The mission took place between 2000 February 11 and 22[4], all the data were acquired in eleven days since the radar scanning system worked independently of darkness or cloud cover. Two antenna pairs operating in C- (5.6 cm; C-RADAR) and X-bands (3.1 cm; X-RADAR) were simultaneously illuminating and recording radar signals. The operational goal of C-RADAR was to generate contiguous mapping coverages, X-RADAR generated data along discrete swaths 50 km wide; X-RADAR was included as an experimental demonstration since the X-band radar had a slightly higher resolution and a better signal to noise ratio than the C-band system.

Instrumentation: the SRTM instrumentation reuses hardware components from the two 1994 Shuttle Radar Laboratory Missions. Two single-pass interferometers were built and operated in parallel, the US C-band system and a German/Italian X-band system X-SAR (details in Table 1.4). The secondary (receive-only) antennas were mounted at the tip of a 60 m long lightweight mast (Figure 1.10[5]).

[4]http://www2.jpl.nasa.gov/srtm/mission.htm
[5]From http://spaceplace.nasa.gov/topomap-earth/

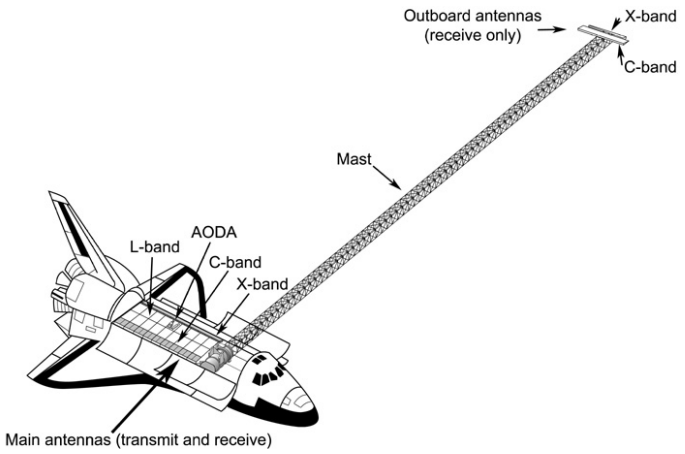

Figure 1.10: SRTM space segment

Wavelength (cm)	3.1
Range pixel spacing (m)	13.3
Azimuth pixel spacing (m)	4.33
Range bandwidth (MHz)	11.25
Effective baseline length (m)	59.9
Baseline angle (°)	54.5
Orbit height (km)	233

Table 1.4: SRTM X-SAR characteristics

The C-band interferometer employed active antennas with electronic steering. To meet the goal of global gap-less mapping, the design goal was a swath width of 225 km; four sub-swaths are imaged quasi-simultaneously by periodically steering the beams from small to large look angles and back. At the same time two swaths (1 and 3 vs 2 and 4 in Figure 1.11[6]) are imaged at different polarization (HH and VV). The X-SAR swath width is in the order of 45 km, the quality of X-band interferograms and DEMs is expected to be better than of those from C-band.
The radar instruments were complemented by the instruments of Attitude and Orbit Determination Avionics (AODA) to measure the geometric baseline. The absolute position of the baseline in space was measured by the GPS receivers with an accuracy of about 1 m.

[6]From http://events.eoportal.org/presentations/129/8271.html

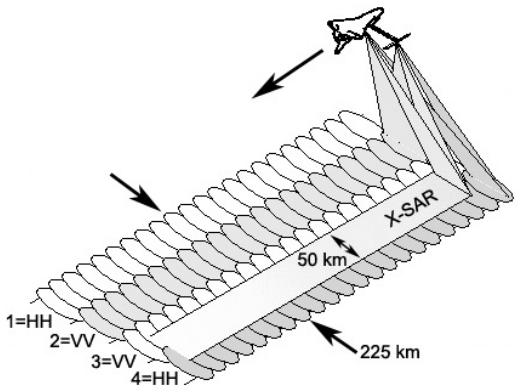

Figure 1.11: SRTM beam geometry

Data production: the C-RADAR data were processed at JPL over a period of nine months; since NASA and NGA (National Geospatial-Intelligence Agency) had different requirements for final data products, two sets of SRTM data were produced [Farr et al., 2007, Vrscaj et al., 2007]. The NGA data comprehends:

- terrain height data: furnished at 1 × 1 arcsecond spacing;
- terrain height error data (THED): estimate of the random error;
- ascending and descending orthorectified image mosaics (OIM);
- seam/hole composite maps: location of all data-take boundaries and voids in the various data takes used in the mosaic.

NGA also produced a version with further improvements: spikes and wells in the data were detected and voided out if they exceeded 100 m compared to surrounding elevations; small voids were filled by interpolation, large voids were left in the data. Water bodies were depicted: the ocean elevation was set to 0 m, lakes of 600 m or more in length were flattened and set to a constant height.
The NASA version 1 data products includes:

- DEM at 1 × 1 arcsecond (SRTM-1);
- DEM at 3 × 3 arcseconds (SRTM-3): produced by averaging nine pixels;
- DEM at lower resolution 30 × 30 arcseconds (SRTM30): produced from USGS GTOPO30 by averaging 30 × 30 pixels and replacing GTOPO30 data with SRTM where possible.

The version 2 data products incorporates the NGA finished data.
The processing of X-RADAR data originates an interferometric DEM with ellipsoidal heights and an additional height error map (HEM).

1.1.6 ASTER DEM

The Advanced Spaceborne Thermal Emission and Reflecting Radiometry (ASTER) is a high-resolution, multispectral imaging system built in Japan for the Ministry of Economy Trade and Industry (METI). A Joint U.S./Japan Science Team was responsible for instrument design, calibration, and validation. It was launched December 19th, 1999 on the Terra platform as part of the National Aeronautics and Space Administration's (NASA) Earth Observing System (EOS) and it collected data between 82 ° N/S latitude [Toutin, 2008]. In Table 1.5 are listed the main differences between ASTER and SRTM at 3 arcseconds.

	ASTER	**SRTM 3 arcseconds**
Data Source	ASTER	Space shuttle radar
Generation and distribution	METI/NASA	NASA/USGS
Release year	2009	2003
Data acquisition period	2000 - ongoing	11 days (in 2000)
Posting interval	30 m	90 m
DEM accuracy (stdev)	7-14 m	10 m
DEM coverage	83 ° north - 83 ° south	60 ° north - 56 ° south
Area of missing data	Area with no ASTER data due to constant cloud cover	Topographic steep area (due to radar characteristics)

Table 1.5: ASTER vs SRTM

Instrumentation: ASTER consists of three subsystems [Toutin, 2002a]: the visible and near infrared (VNIR), the shortwave infrared (SWIR), and the thermal infrared (TIR) (details in Table 1.6); the VNIR subsystem is the only one to provide stereo capability.

Characteristics	VNIR	SWIR	TIR
Spectral range (μm)	Band 1 0.52-0.60 Nadir looking	Band 4 1.60-1.70	Band 10 8.125-8.475
	Band 2 0.63-0.69 Nadir looking	Band 5 2.145-2.185	Band 11 8.475-8.825
	Band 3N 0.76-0.86 Nadir looking	Band 6 2.185-2.225	Band 12 8.925-9.275
	Band 3B 0.76-0.86 Nadir looking	Band 7 2.235-2.285	Band 13 10.25-10.95
	–	Band 8 2.295-2.365	Band 14 10.95-11.65
	–	Band 8 2.360-2.430	–
Ground resolution (m)	15	30	90
Data rate (Mbits/s)	62	23	4.2
Cross-track pointing (deg)	±24	±8.55	±8.55
Cross-track pointing (km)	±318	±116	±116
Swath width (km)	60	60	60
Quantization (bits)	8	8	12

Table 1.6: ASTER system characteristics

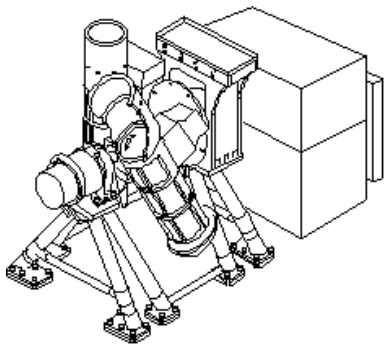

Figure 1.12: VNIR subsystem

The VNIR subsystem (Figure 1.12) operates in three spectral bands at visible

and near-IR wavelengths, with a resolution of 15 m. It consists of two independent telescopes: one nadir-looking with a three-spectral-band detector, and the other backward-looking with a single-band detector. The VNIR subsystem produces by far the highest data rate of the three ASTER imaging subsystems. With all four bands operating the data rate including image data, supplemental information and subsystem engineering data is 62 Mbps.

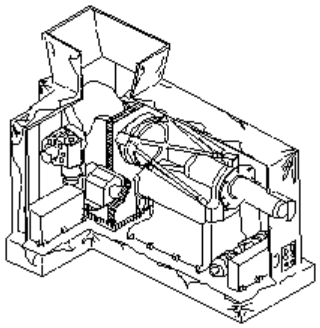

Figure 1.13: SWIR subsystem

The SWIR subsystem (Figure 1.13) operates in six spectral bands in the near-IR through a single, nadir-pointing telescope that provides 30 m resolution; cross-track pointing is accomplished by a pointing mirror.

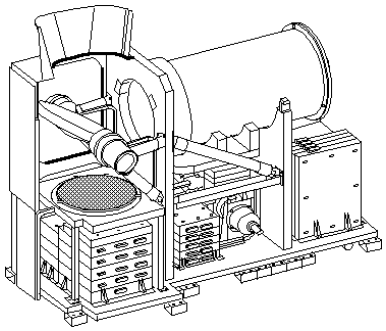

Figure 1.14: TIR subsystem

The TIR subsystem (Figure 1.14) operates in five bands in the thermal infrared region using a single, fixed-position, nadir-looking telescope with a resolution of 90 m. Unlike the other instrument subsystems, it has a “whiskbroom”

scanning mirror which functions both for scanning and cross-track pointing (to 8.55 degrees). In the scanning mode, the mirror oscillates at about 7 Hz and, during oscillation, data are collected in one direction only. Because of the instrument's high data rate, restrictions have been imposed so that the average data rate is manageable by the spacecraft data management system.

Data production: ASTER provides Standard Data Products throughout the life of the mission [Welch et al., 1998]; algorithms to compute these products were created by the ASTER Science Team, and are implemented at the Land Processes DAAC (Distributed Active Archive Center). Table 1.7 shows the different data products available[7]. The ASTER GDEM is in GeoTIFF format with geographic lat/long coordinates and a 1 arcsecond (30 m) grid of elevation and it is referenced to the WGS84/EGM96 geoid. Pre-production estimated accuracies for this global product were 20 meters at 95% confidence for vertical data and 30 meters at 95% confidence for horizontal data.
Studies conducted to validate the ASTER GDEM [METI/ERSDAC et al., 2009] calculated an overall vertical RMSE of 10.87 m (considering 934 GDEM tiles) as compared to NED data; when compared with more than 13000 GCPs from CONUS (Contiguous United States), the RMSE dropped to 9.35 meters. Similar studies conducted by Japanese investigators confirmed these results, however it is necessary to point out that various factors effect local ASTER GDEM accuracy, so the errors can vary in dependence of the area considered.

[7] http://asterweb.jpl.nasa.gov/data_products.asp

Level	Product	Description
1A	Radiance at sensor	Image data plus radiometric and geometric coefficients Data are separated by telescope
1B	Registered radiance at sensor	1A data with radiometric and geometric coefficients applied
1AE	Radiance at sensor	Image data plus radiometric and geometric coefficients Data are separated by telescope
1BE	Registered radiance at sensor	1AE data with radiometric and geometric coefficients applied
2	AST09 Surface radiance-VNIR,SWIR	Radiance corrected for atmospheric effects
	AST09T Surface radiance-TIR	Radiance corrected for atmospheric effects
	AST09XT Surface radiance-VNIR,SWIR Crosstalk Corrected	Radiance corrected for atmospheric effects VNIR and Crosstalk Corrected SWIR
	AST07 Surface reflectance-VNIR,SWIR	Derived from surface radiance with topographic corrections
	AST07XT Surface reflectance-VNIR,SWIR Crosstalk Corrected	Derived from surface radiance with topographic corrections VNIR and Crosstalk Corrected SWIR
	AST08 Surface kinetic temperature	Temperature-emissivity separation algorithm applied to atmospherically corrected surface radiance data
	AST05 Surface emissivity kinetic temperature	Temperature-emissivity separation algorithm applied to atmospherically corrected surface radiance data
3	ASTER GDEM	Global DEM (GDEM) 1×1 degree tiles, 30 m postings, GeoTIFF format
	AST14 DEM	DEM produced by stereo correlation of nadir and aft Band 3 data
	AST14OTH Orthorectified	15 orthorectified L1B radiance images GeoTiff format
	AST14DMO Orthorectified + DEM	15 orthorectified L1B images + DEM

Table 1.7: ASTER products

1.2 DEM quality assessment

Digital elevation models are digital representations of surfaces; they can be derived from different sources and they are used in different fields related to geographical analyses.
During the DEMs generation process different kinds of elevation sampling errors may occur, moreover the surface is complex and irregular, so, even if no error are present, the limited elevation sampling points bring the model to a rough approximation of the true surface [Guo-an et al., 2001].
To evaluate the quality of a DEM it is possible to distinguish between the interior quality (precision) and the exterior one (accuracy); the former defines how well the model fits the data used to generate it, while the latter defines the concordance level with external data [Karel et al., 2006].
The accuracy of a DEM can be defined as the degree of closeness of measurements of the attribute value to its actual value. The precision can be defined as the degree to which repeated measurements under unchanged conditions show the same results.
To determine model precision a very simple approach is the evaluation of the residuals, so the height differences between the original data and the interpolate surface; another method is to leave out some input data and to compare them to the output surface (cross-validation). Among the different statistic that can be computed on the residuals the median is a robust indicator for systematic errors in height.
The accuracy of DEM is affected by different factors such as the quality of the source data, the sampling method, DEM resolution, surface complexity, etc. and it can be evaluated using external data that were not used in the DEM production step. The exterior quality is useful to describes both the model and the process to generate it; the external data should be more accurate than the model under test. Another way to estimate the accuracy of particular digital elevation model is to use empirical formulas fitted for specific DEM generation method; for example in case of Airborne Laser Scanning derived DEMs one of the proposed empirical formulas is the following (where n correspond to the points density and $tan\,(\alpha)$ to the terrain slope) [Karel et al., 2006, Karel and Kraus, 2007].

$$\sigma_z[cm] = \pm\left(\frac{6}{\sqrt{n}} + 30tan\,(\alpha)\right) \tag{1.16}$$

In the next section the ISO requirements for digital elevation models are listed; this to point out the fact that a validation procedure for assessing the quality of a DEM in terms of accuracy is needed.

1.2.1 ISO requirements

As geographical products DEMs need to respect the requirements of the standard for special data; in particular the International Organization for Standardization produced two documents related to geographic data: ISO 19113:2002 and ISO 19114:2003.

- ISO 19113:2002[8] establishes the principles for describing the quality of geographic data and specifies components for reporting quality information and it is applicable to digital data such as digital elevation models.
- ISO 19114:2003[9] provides a framework of procedures for determining and evaluating quality that is applicable to digital geographic datasets, consistent with the data quality principles defined in ISO 19113.

The ISO 19113:2002 defines a set of characteristics that should be used to define the quality of a digital product [ISO/TC211, 2008]:

- completeness: presence and absence of features, their attributes and relationships
  - commission: excess data present in a dataset
  - omission: data absent from a dataset
- logical consistency: degree of adherence to logical rules of data structure, attribution and relationships
  - domain consistency: adherence of values to the value domains
  - format consistency: degree to which data is stored in accordance with the physical structure of the dataset
  - conceptual consistency: adherence to rules of the conceptual schema
  - topological consistency: correctness of the explicitly encoded topological characteristics of a dataset
- positional accuracy: accuracy of the position of features
  - relative or internal accuracy: closeness of the relative positions of features in a dataset to their respective relative positions accepted as or being true

[8] http://www.iso.org/iso/catalogue_detail.htm?csnumber=26018
[9] http://www.iso.org/iso/catalogue_detail.htm?csnumber=26019

    - absolute or external accuracy: closeness of reported coordinate values to values accepted as or being true
    - gridded data position accuracy: closeness of gridded data position values to values accepted as or being true
- temporal accuracy: accuracy of the temporal attributes and temporal relationships of features
    - accuracy of a time measurement: correctness of the temporal references of an item
    - temporal consistency: correctness of ordered events or sequences, if reported
    - temporal validity: validity of data with respect to time
- thematic accuracy: accuracy of quantitative attributes and the correctness of non- quantitative attributes and of the classifications of features and their relationships.
    - classification correctness: comparison of the classes assigned to features or their attributes with respect to ground truth
    - non-quantitative attribute correctness: correctness of non-quantitative attributes
    - quantitative attribute accuracy: accuracy of quantitative attributes

In a digital elevation model the quality is mainly function of the positional accuracy.

1.3 DEM derivatives

DEM derivatives are data products derived from DEM data. Often their computation involves operation on neighbours cells in the original digital elevation model [El-Sheimy et al., 2005, Bajata et al., 1999]. The operation is based on the height difference between one cell in the DEM and its surrounding.

1.3.1 First order derivatives: slope and aspect

Slope is defined as the rate of change in elevation Δz over a change in spacial position; it is usually measured as degrees or percent.
The rate of change in elevation both in x and y direction is useful to identify

the direction and magnitude of the steepest gradient. The magnitude (slope) can be obtained by combining the two component partial derivatives:

$$Slope = \frac{\delta Z}{\delta XY} = \sqrt{\left(\frac{\delta Z}{\delta X}\right)^2 + \left(\frac{\delta Z}{\delta Y}\right)^2} \tag{1.17}$$

Elevation may change in both x and y direction, so the slope resulting from a change in position is the vector sum of the slope in the x direction and of the slope in y direction (see Figure 1.15).

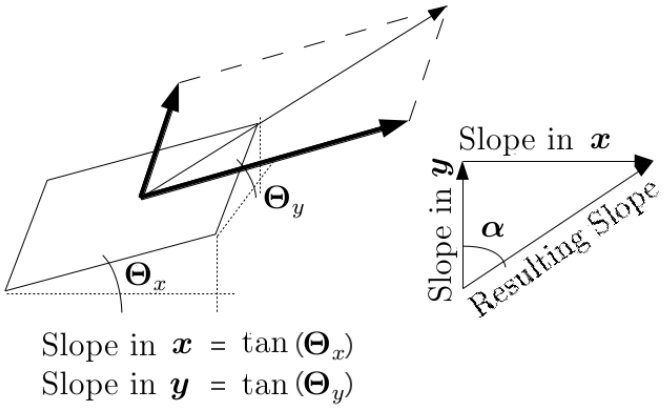

Figure 1.15: Slope definition

The aspect value assigned to each cell defines the direction (north, south, etc..) to which that cell is oriented. Taking in consideration Figure 1.15 the aspect can be defined as:

$$Aspect = tan\,(\alpha) = \frac{\frac{\delta Z}{\delta X}}{\frac{\delta Z}{\delta Y}} \tag{1.18}$$

The aspect is usually measured in degrees from 0 to 360, in case of flat surfaces (e.g. lakes etc..) it is not possible to assign an aspect value, so some software may assign or the value “0” or “-1”.

1.3.2 Second order derivative: curvature

The second order derivative of a digital elevation model describes the terrain slope change rate. It also describes the curvature of the terrain in term of

how convex, concave or straight each grid cell is configured.
Curvature maps are very useful in different practical analysis as in land curvature studies, aging of terrain studies or flow acceleration. Curvature is computed as:

$$Curvature = \sqrt{\left(\frac{\delta^2 Z}{\delta X^2}\right)^2 + \left(\frac{\delta^2 Z}{\delta Y^2}\right)^2} \tag{1.19}$$

In curvature maps negative values point out that the terrain is upwardly concave at the cell (e.g. valley type formation). Zero values derives from flat cells and positive values indicates that the terrain is upwardly convex at the cell (e.g. mountainous area).

Chapter 2

LiDAR data filtering

One of the possible sources for DEMs creation is the Airborne LiDAR; since a LiDAR dataset was available for the area under analysis it was used to generate a DSM and a DTM. In this chapter the LiDAR filtering method used is described and its results are compared to the one obtained with a commercial software. In the latter part of the chapter the DEM interpolation steps are described.

2.1 Filtering algorithms

In the previous chapter the airborne laser scanning was listed among the possible DEMs sources (see Section 1.1.3). Since in the area taken in consideration for DEMs comparison and validation a LiDAR dataset was available it was used to obtain a digital surface and a digital terrain model. A LiDAR datased needs to be classified in order to extract the points belonging to the ground; the classification is also useful to determine points belonging to building or to vegetated area.
Among the different algorithms available to filter the data available two particular methods were taken in consideration: the former algorithm was developed within GRASS GIS by the Laboratory of Geomatics at the Politecnico di Milano and the latter, implemented in TerraScan, makes use of the Axellson classification procedure.
The classification using GRASS was carried out after a parameter calibration procedure by means of UCODE_2005; the classification with TerraScan was provided by OGS both in automatic and semi-automatic procedure.
In the following section the algorithms, the calibration phase and the execution modality will be described.

2.1.1 GRASS GIS filtering algorithms

GRASS (Geographic Resources Analysis Support System) is a GIS software used for geospatial data management and analysis, image processing, graphics and maps production, spatial modeling, and visualization [Mitasova and Neteler, 2004]. It is a Open Source and Free Software GIS with GNU GPL licence and this means users can run the program for any purpose and can redistribute copies but also, and more important, user can study how the program works and can improve the program and release the improvements. The cascade commands, developed for this software, are three (v.lidar.edgedetection, v.lidar.growing, v.lidar.correction) and are present in the last release of GRASS [Brovelli et al., 2004, Brovelli and Cannata, 2002].
These algorithms can be classified as morphological or slope based and for each of them many execution parameters, ensuring algorithms flexibility, have to be set.

v.lidar.edgedetection allows the detection of the edges of the surface objects; where an edge can be thought as a significant change in the height value corresponding to a small shift of the horizontal position.
The algorithm performs at first an approximation of the DSM by means of bilinear and bicubic spline functions with Tikhonov regularisation in a least squares approach. The two surfaces are regularised minimising the gradient (G_m) and the curvature.

$$G_m = \sqrt{G_x^2 + G_y^2} = \sqrt{\left(\frac{dz}{dx}\right)^2 + \left(\frac{dz}{dy}\right)^2} \tag{2.1}$$

In the former case a low regularisation parameter (λ_g) brings the interpolating functions as close as possible to the observations, whereas in the latter one the choice of a high value for λ_r gives a rough and loose-fitting surface.
The imposition of a unique threshold to the gradient magnitude is not suitable because if a low value was chosen it would be impossible to discriminate between an actual edge and possible measurement noise and if a high value was chosen only very sharp height changes would be detected. The basic hypothesis is that noise corresponds mostly to an isolated observation or, at least, adjacent noises are generally not organised in a regular shape. In contrast, an edge shows a regular, chain-like behaviour.
For these reasons two thresholds for the magnitude gradient, the high (T_g) and low (t_g) thresholds, are set.
Every point P where the magnitude gradient exceeds T_g is classified as a possible edge point. For every point where the magnitude gradient is lower

than T_g but exceeds t_g we find, along the direction of the maximum direction of gradient rise (θ_P perpendicular to the direction of the edge vector), the two neighbouring and opposite points P_1 and P_2.

$$\theta_P = tan^{-1}\left(\frac{G_y}{G_x}\right) + \frac{\pi}{2} \tag{2.2}$$

If these points have the same edge direction of P and if the magnitude gradient for the eight nearest neighbouring points exceeds T_g in at least two instances, the point will be classified as a possible edge point. In other cases it is classified as non-edge point.
The output contains the classification of the nature of the measurement points (edge, non edge).
The parameters to be set are the interpolation step in east and north direction (S_{ee}, S_{en}), the Tikhonov regularising parameter with bilinear splines (λ_g), the two thresholds t_g and T_g for the gradient magnitude, the threshold θ_g for the edge direction, the Tikhonov regularising parameter with bicubic splines (λ_r).

v.lidar.growing fills-in the edge previously obtained using the idea that the inner part of an object has generally a greater height than its edges.
Using the mean height value of the points within each cell the data are rasterized with a resolution t_d equal to the minimum data raw density. For each cell the presence of points with double reflection is evaluated (difference between first and last reflection greater than t_j). Starting from the cells classified as 'edge' and with only one reflection, all the linked cells are found and a convex hull algorithm is applied on them computing at the same time the mean of the corresponding heights (mean edge height). The points inside the convex hull are classified as objects in case their height is greater or equal to the previously mean computed edge height.
The output contains the classification in four classes (terrain, terrain with double reflection, object with double reflection, object).
The parameters to be set are a rasterizing grid resolution to be used in the region growing algorithm (t_d) and the minimum difference to assume a double reflection for each cell (t_j).

v.lidar.correction corrects imprecision that the v.lidar.growing procedure can generate.
A bilinear interpolation with Tikhonov regularising parameter (λ_c) only on the ground points is performed.
The analysis of the residuals (Δ) between the observations and the interpolated values compared with two thresholds t_c, T_c consents the reclassification of

some points to obtain the four output classes (terrain, terrain with double reflection, object with double reflection, object).

- if the point is classified as terrain and $\Delta > T_c$, it will be reclassified as object
- if the point is classified as 'terrain with double reflection' and $\Delta > T_c$, it will be reclassified as 'object with double reflection'
- if the point is classified as object and $|\Delta| < t_c$, it will be reclassified as terrain
- if the point is classified as 'object with double reflection' and $|\Delta| < t_c$, it will be reclassified as 'terrain with double reflection'

The parameters to be set in the last command are the spline steps in east and north direction (S_{ce}, S_{cn}), the Tikhonov regularising parameter with bilinear splines (λ_c) , the two thresholds t_c and T_c for residuals analysis.

All the parameters were once calibrated in an empirical way for LiDAR dataset with low spatial resolution (0.9 point/m^2), so there was the necessity to create a structured calibration procedure to obtain calibrated parameter values for different spatial resolution dataset.

2.1.2 UCODE_2005

UCODE_2005 is a software developed by United States Geological Survey (USGS) that performs model calibration with non-linear regression methods and sensitivity analysis in an iterative way.
It can be applied with any application model or set of models; the only requirement is that they have numerical (ASCII or text only) input and output files and that numbers in these files have sufficient significant digits [Poeter et al., 2008].
UCODE_2005 is built using the JUPITER API capabilities and conventions, which facilitates inter program communications.
The estimated parameters can be defined with user-specified functions: for example prior, or direct, information on estimated parameters also can be included in the regression.
UCODE_2005 needs different files to work, and the most important one is the configuration file (.in). The .in file [Poeter and Hills, 1998] specifies the command to run the model, the parameters to be evaluated and their information (starting value, lower reasonable value, largest reasonable value, scale parameter values, adjustability, fractional amount of perturbation for

sensitivity, applied log-transformation, maximum fractional change between iterations, etc..), and the other files needed for the calibration procedure: the model input file (.if), the model input file template (.tpl), the model output file (.est), the model output file structure (.ins).
The program to run requires the definition of the parameters to be estimated and the definition of the observations that it use to verify every iteration results.
In the present work all the parameters had been defined in the configuration file while for the observations an ad hoc file (.flo) was created; it contains all the observation used by the software to verify the accuracy of the simulated equivalent values.
Observations to be matched in the regression can be any quantity for which a simulated equivalent value can be produced, thus simulated equivalent values are calculated using values that appear in the application model output files and can be manipulated with additive and multiplicative functions, if necessary. The file .if (model input file) and .tpl (input file template) are used by UCODE_2005 to update the parameter values every iteration. In the configuration file the last pair of files to be defined are the model output file (.est) and the model instruction file (.ins). The former is the file in which the results of the model at every iteration are saved, the latter specifies the format of the output file.

2.1.3 GRASS-UCODE_2005 integration

In order to perform the calibration procedure on the algorithm parameters it was necessary to integrate the two software packages (UCODE_2005 and GRASS GIS). The integration is due to the need of commands to work within GRASS environment. A schema of the file structure [Lucca, 2008] behind the calibration procedure is shown in Figure 2.1.
The UCODE_2005 files can be presented in the configuration file divided in different section (command line, parameters, observations, model input file and model output file). The integration between the two software is performed thanks to an intermediate script that read the current value of the parameters and pass it to the "GRASS script" in order to perform the filtering step.
At every iteration UCODE_2005 executes the intermediate script that reads the actual parameter values in the UCODE_2005 model input file and executes the "GRASS script" which in turn executes some commands and creates the numerical output file. UCODE_2005 finally reads the output file accordingly to the Model output file component and compares the observation simulated

equivalent with the observations value.

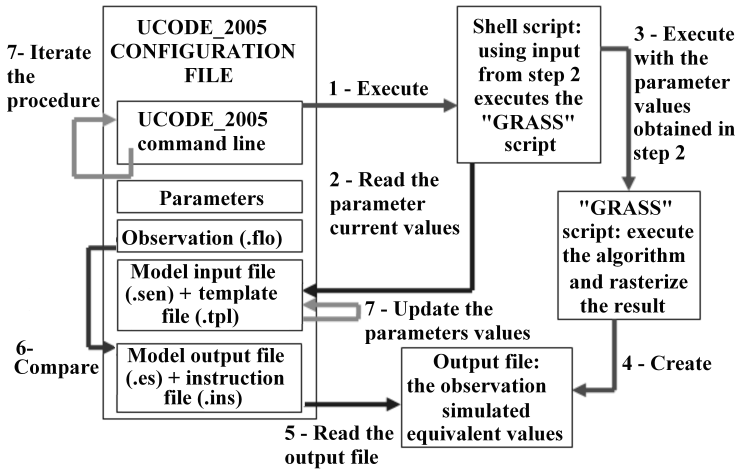

Figure 2.1: UCODE_2005 - GRASS integration scheme

As calibration area a small region with some buildings is usually chose; the calibration procedure is carried on independently for each LiDAR module [Brovelli and Lucca, 2009]; at first the v.lidar.edgedetection parameters are calibrated, then the edge detection is performed with the resulting parameters value and on the following algorithm the calibration is performed; the algorithm results are rasterized and each cell has a simulated equivalent value.
The observations to be compared with the output are created rasterizing the result of a building map of the area (digitized with the support of an ortophoto or directly provided in a vector format).
After the calibration procedure a validation in an independent zone is performed to evaluate the accuracy of the results; in this second area the algorithms with the calibrated parameter values are executed and the result, after rasterization, is compared with the raster building map.

2.1.4 TerraScan Axelsson algorithm

Axelsson developed in 1999 a filtering algorithm based on TIN densification that is now used in the commercial software TerraScan.
The algorithm derives a TIN network from the neighbouring minima as a first approximation of the bare earth. In iterative steps the TIN is modified by adding other laser points that meet certain distance and orientation criteria

in relation to the triangles that contains them [Sithole, 2005].
The vegetation and the buildings are classified using a cost function based on the second derivatives on the elevation differences [Axelsson, 1999]. The model assumes that the buildings consist of connected planar surfaces, so along a scan line the points belonging to a change of direction of the roof will cause a non-zero value of the second derivatives and will be defined as breakpoints, in the opposite case (zero value of the second derivatives) points will be classified as belonging to a straight line segment; vegetation instead is modelled as points with randomly distributed second derivatives.
The TerraScan classification procedure based on Axelsson algorithm is usually carried on in three different steps; at first a division between ground and over-ground points is carried on, then, on the over-ground points is performed the building classification and as last step the vegetation is extracted. Additional steps to extract linear object (power lines etc..) or to increase the classification detail (division between high and low vegetation) may be performed.

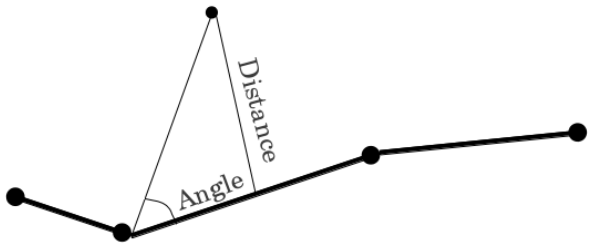

Figure 2.2: TerraScan iteration angle and distance

TerraScan provides different routine to perform the classification, for example to classify ground points a routine is available; it classifies ground points by iteratively building a triangulated surface model starting from the selection of some local low points that are confident hits on the ground; after the first step the program iteratively adds laser point to the ground model, the iteration parameters determine how close a point must be to a triangle plane for being accepted as ground point and added to the model; the parameters [TerraSolid, 2011] to be set for the whole procedure are:

- maximum building size: edge length of the largest building, it specifies an area in which at least one it belongs to the ground

- iteration angle: maximum angle between a point, its projection on triangle plane and the closest triangle vertex (see Figure 2.2)

- iteration distance: maximum distance from point to triangle plane (usually between 0.5 and 1.5 meters)

- terrain angle: steepest allowed slope in ground terrain (usually between 4.0 and 10.0 degrees respectively for flat and rough terrain)

In case of semi-automatic classification, after each step a manual check and reclassification of uncertain points is done by the user; this operation allow to increase the classification accuracy but it is time consuming: the average manual editing efficiency, depending both on the morphological complexity of the area and on the final accuracy in classification, is about 4-5 km^2 in 8 hours.

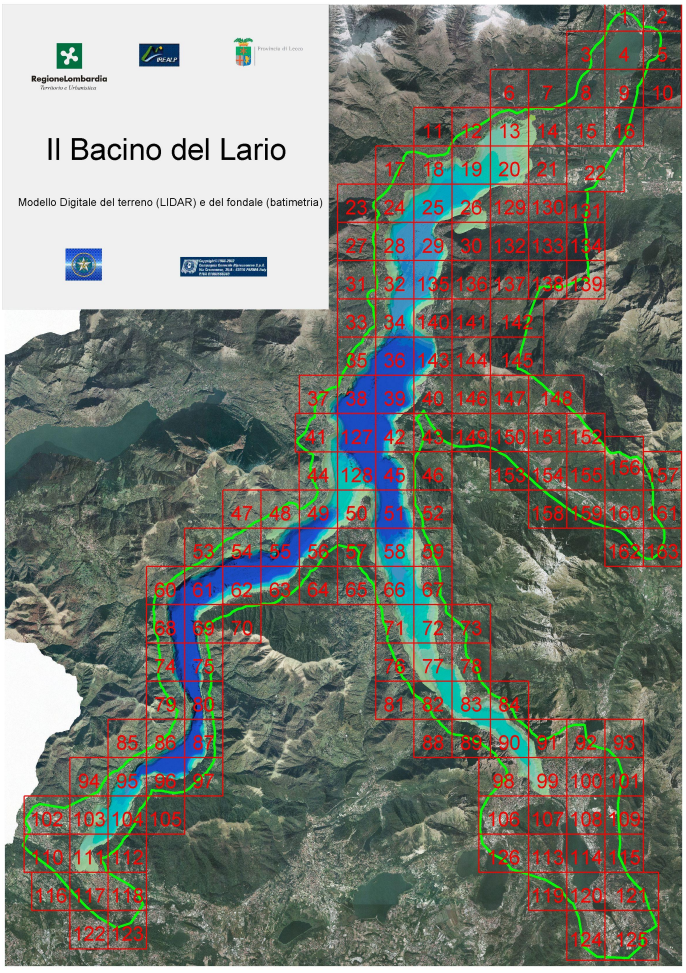

Figure 2.3: Dataset extension

2.2 LiDAR dataset

The LiDAR data delivered by the Lombardia Region (Italy) consist in raw data corresponding to first and last reflections all over the Como area; the whole dataset contains 125 areas (Figure 2.3), in this work only the data near the city of Como were considered: in particular the areas 110, 116, 117, 118, 122 and 123; the projection and coordinates system of the dataset used is UTM32-ETRF89 with ellipsoidal heights; this LiDAR dataset has already been validated using GPS observations.

After removing strip border line observations (according to the flight plan), the calibration of the data filtering parameters was performed in a small region of the dataset (Figure 2.4).

Figure 2.4: Calibration area

As stated in the previous section each command was calibrated independently; once the calibrated parameters value of the first step (v.lidar.edgedetection) were available, the calibration procedure was set up for the second step (v.lidar.growing) and so on. The obtained calibrated value were then approximated to be used for filtering the whole dataset.

Table 2.1 contains the results obtained for the first filtering step, while Table 2.2 and Table 2.3 contain the results respectively for the growing and the correction procedure.

Parameter		Default value	Calibrated value - after 5 iterations	Approximated value
S_{ee}	Spline interpolation step (East)	4	1.00	1
S_{en}	Spline interpolation step (North)	4	1.00	1
T_g	High threshold (gradient)	6	1.5	1.5
t_g	Low threshold (gradient)	3	1.00	1
λ_g	Regularization parameter (bilinear spline)	0.01	0.001	0.001
θ_g	Edge detection threshold	0.26	0.18	0.18
λ_r	Regularization parameter (bicubic spline)	1	1	1

Table 2.1: v.lidar.edgedetection parameters

Parameter		Default value	Calibrated value - after 5 iterations	Approximated value
t_j	Rasterization resolution	0.2	0.2244	0.22
t_d	Threshold for the height reflection difference	0.6	0.1421	0.14

Table 2.2: v.lidar.growing parameters

Parameter		Default value	Calibrated value - after 9 iterations	Approximated value
S_{ce}	Spline interpolation step (East)	25	19.05	19
S_{cn}	Spline interpolation step (North)	25	17.37	17
T_g	High threshold (residual analysis)	2	2.856	2.9
t_g	Low threshold (residual analysis)	1	2.430	2.4
λ_c	Regularization parameter (bilinear spline)	1	0.6532	0.65

Table 2.3: v.lidar.correction parameters

The automatic classification with TerraScan included different classes: ground, low vegetation (from 0.5 m to 2 m), high vegetation (from 2 m to 50 m), buildings, bridges and water bodies. The ground class was extracted using two approaches in case of mountainous or flat area: in the former case the default class extracted was the ground one using the parameters listed in Table 2.4, in the latter case the points were assigned by default to the low vegetation class (parameters in Table 2.5) and then among those points the ground points were extracted using the parameters in Table 2.6.
The automatic and the semi-automatic classifications using TerraScan were provided by the OGS.

Parameter	Value
Maximum building size	10
Terrain angle	45
Iteration angle	20
Iteration distance	1.4

Table 2.4: Ground routine parameters - mountainous area

Parameter	Value
Maximum building size	120
Terrain angle	80
Iteration angle	10
Iteration distance	1.4

Table 2.5: Ground routine parameters - flat area - low vegetation points extraction

Parameter	Value
Maximum building size	5
Terrain angle	80
Iteration angle	10
Iteration distance	1.4

Table 2.6: Ground routine parameters - flat area - low vegetation points extraction

2.3 Automatic classification comparison

In general the comparison between GRASS and TerraScan classification is quite difficult, because the two software do not produce the same class division: with GRASS the classes obtained are terrain (cat 1), terrain with double reflection (cat 2), object with double reflection (cat 3) and object while using TerraScan ground, low vegetation, high vegetation and buildings points are extracted. The GRASS terrain correspond to TerraScan ground but for the other classes it is not possible to determine an univocal link, the main issue is that the GRASS filtering algorithms until now are not able to precisely extract points belonging to vegetation: these points are spread among the terrain with double reflection class (medium - low vegetation), object with double pulse class (high vegetation) and object class (area with continuous vegetation), as consequence it is not possible to state that the object class contains only buildings and man-made features [Brovelli and Lucca, 2011, 2012].
In this particular work the classifications have other discrepancies: the one produced with GRASS used the points obtained after strip overlap removal while in TerraScan all the dataset was taken in consideration; in Table 2.7 the total amount of last reflection points available, the amount of points removed

due to the strip overlap issue and the amount of points classified with GRASS is reported for each survey area.

Survey area	**Last reflection points (total)**	**Points removed (total)**	**Points removed (percentage)**	**Last reflection points classified**
Area 110	4468553	2652606	59.36%	1815947
Area 116	1803715	603727	33.47%	1199988
Area 117	4345695	2781882	64.01%	1563813
Area 118	3134658	1730976	55.22%	1403682
Area 122	699399	66112	9.45%	633287
Area 123	2049155	695245	33.93%	1353910
Whole region	16501175	8530548	51.70%	7970627

Table 2.7: Last reflection points: total, removed due to strip overlap and used for filtering

2.3.1 GRASS data filtering

The filtering procedure with GRASS was carried out by using the approximated parameters value indicated in Table 2.1, Table 2.2 and Table 2.3 respectively for the edge-detection, the growing and the correction algorithms; in Table 2.8 the classification results for each area are presented while Table 2.9 presents the summary for the whole region.
The results reported in Table 2.8 indicate that the filtering procedure within GRASS was not able to identify accurately the lower and the medium vegetation, in fact the amount of points belonging to category two and three is much lower than the one of category one and four; this problem is evident also in Table 2.9, in fact only the 6.92% of points belong to category 2 and 7.53% to category 3.

Class	Area 110	Area 116	Area 117	Area 118	Area 122	Area 123
Category 1: terrain	958653 52.79%	803323 66.94%	821039 52.50%	787048 56.07%	367025 57.96%	68978 50.95%
Category 2: terrain with double reflection	116583 6.42%	136719 11.39%	101571 6.50%	74726 5.32%	38632 6.10%	83708 6.18%
Category 3: object with double reflection	146043 8.04%	67733 5.65%	108608 6.95%	102203 7.28%	42962 6.78%	132346 9.77%
Category 4: object	594668 32.75%	192213 16.02%	532595 34.05%	439705 31.33%	184668 29.16%	448078 33.10%

Table 2.8: GRASS filtering results for each area

Class	Total	Percentage
Cat 1: terrain	4426866	55.54%
Cat 2: terrain with double reflection	551939	6.92%
Cat 3: object with double reflection	599895	7.53%
Cat 4: object	2391927	30.01%

Table 2.9: GRASS filtering results for the whole region

In the Figure 2.5 and Figure 2.6 two examples of the classification results with GRASS are shown; Figure 2.5 shows that in the area almost no points were classified as high vegetation (object with double reflection), this fact indicates the possibility that some points belonging to vegetation were classified instead as object. The same problem is more evident in Figure 2.6 in which some continuous forestry areas (lower left or upper right in the image) are not classified as vegetation (object with double pulse or terrain with double pulse) but as object; this is a shortcoming of the filter, the direct consequence is that the object class does not contain only man-made features such as buildings.

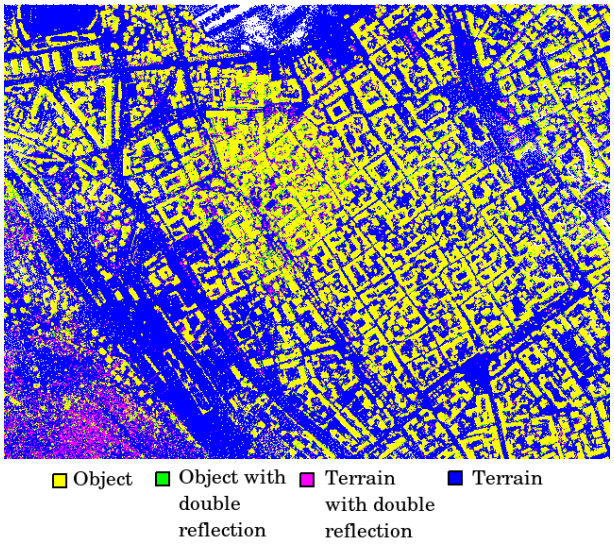

Figure 2.5: Example of the GRASS classification

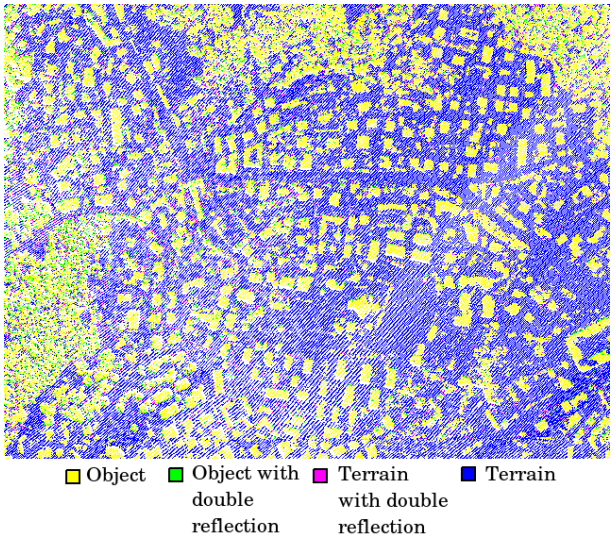

Figure 2.6: Example of the GRASS classification

2.3.2 TerraScan automatic data filtering

The filtering procedure with TerraScan was executed on the whole dataset available, no overlap between strips was removed. To compare GRASS and TerraScan results it was decided to reduce the TerraScan classification results

on the GRASS one using the v.select command within GRASS; Table 2.10 show that the total amount of points filtered by TerraScan include both the last and the first reflection, in fact the total amount of TerraScan classified points (19076729 points) is greater than the total amount of last points (16501175 points), in the same Table the total amount of points used for the comparison, after dataset reduction, is shown; the points counts is slightly different from the GRASS dataset (7970627 points) due to map border managing problems in the v.select command.

Survey area	**Complete dataset**	**Reduced dataset**	**GRASS dataset**
Area 110	5204327	1815994	1815947
Area 116	2148165	1200007	1199988
Area 117	4955526	1563845	1563813
Area 118	3539514	1403705	1403682
Area 122	806685	633289	633287
Area 123	2422512	1353925	1353910
Whole region	19076729	7970765	7970627

Table 2.10: Points filtered with TerraScan: complete and reduced dataset and GRASS dataset

Similarly to the previous section in Table 2.11 the filtering results for each area is presented, while in Table 2.12 the summary for the whole region is reported.
The results in Table 2.11 indicate that TerraScan was able to detect both the low and the high vegetation points other than the ones belonging to buildings and ground. Figure 2.7 and Figure 2.8 shows the TerraScan automatic classification for the same example areas used in the GRASS section. In Figure 2.7 most of the buildings are classified correcly, except in the upper right part of the image in which some of them are classified as high vegetation. In Figure 2.8 the results is better than the one obtained with GRASS (Figure 2.6), since the vegetated areas are filtered more correctly. These two examples indicate that the automatic classification is not completely accurate but it is quite reliable, while the one obtained with GRASS is subjected to problems in detecting the vegetated areas.

Class	Area 110	Area 116	Area 117	Area 118	Area 122	Area 123
Ground	530916 29.23%	700275 58.36%	452484 28.94%	445355 31.73%	260363 41.11%	479506 35.42%
Building:	134856 7.43%	74671 6.22%	240130 15.35%	183215 13.05%	75481 11.92%	90737 6.70%
Low vegetation	126520 6.96%	83173 6.93%	104845 6.70%	126347 9.00%	36320 5.74%	83618 6.18%
High vegetation	960585 52.90%	292243 24.35%	668571 42.75%	572698 40.80%	251094 39.65%	664270 49.06%
Unclassified points	63117 3.48%	49645 4.14%	97842 6.26%	76090 5.42%	10031 1.58%	35794 2.64%

Table 2.11: TerraScan filtering results for each area

Category	Total	Percentage
Ground	2868899	35.99%
Building	799063	10.03%
Low vegetation	560823	7.04%
High vegetation	3409461	42.77%
Unclassified	332519	4.17%

Table 2.12: TerraScan filtering results for the whole region

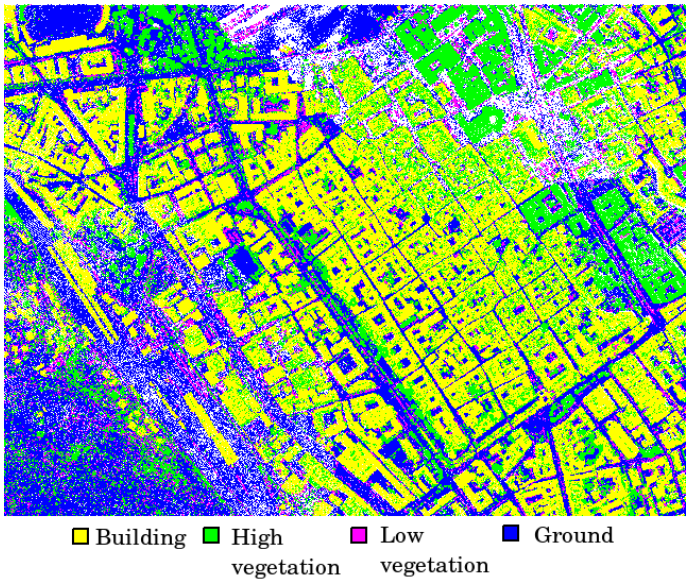

Figure 2.7: Example of the automatic TerraScan classification

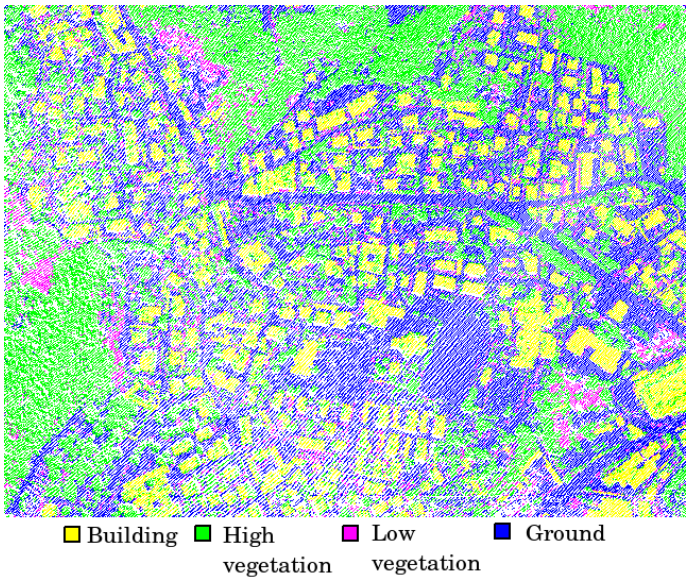

Figure 2.8: Example of the automatic TerraScan classification

2.3.3 GRASS - automatic TerraScan automatic comparison

The comparison between GRASS and TerraScan was performed extracting the overlapping points between different classes, in such way it is possible, for example, to extract the amount of points classified as terrain by GRASS and as ground by TerraScan; the results obtained are contained in Table 2.13. The table confirms that points classified as object for GRASS in reality could be spread among different classes, in fact the same points in the TerraScan result belong to high vegetation (2016932 points) but also to low vegetation (27073 points) and ground (65322 points).
To point out better the discrepancies between the two filtering results the percentages of the points with respect to the total amount of points for each classes were computed; practically two tables are available, the former (Table 2.14) was computed with respect to the GRASS classification, so the percentage of the first line are computed with respect to the relative total and so on, the latter (Table 2.15) was computed with respect to the TerraScan classification.

		TerraScan				
		Ground	Buildings	High vegetation	Low vegetation	Unclassified points
GRASS	Category 1: terrain	2509537	298967	890117	447418	280827
	Category 2: terrain with double reflection	247443	10966	199080	73693	20757
	Category 3: object with double reflection	68758	29066	472610	169631	12530
	Category 4: object	43161	460064	1847654	22781	18267

Table 2.13: Overlap between GRASS and TerraScan classes in terms of points number

		TerraScan			
		Ground	Buildings	High vegetation	Low vegetation
GRASS	Category 1: terrain	56.69%	6.75%	20.11%	10.11%
	Category 2: terrain with double reflection	44.83%	1.99%	36.07%	13.35%
	Category 3: object with double reflection	11.46%	4.85%	78.78%	2.82%
	Category 4: object	1.80%	19.23%	77.25%	0.95%

Table 2.14: Overlap: percentages with respect to the GRASS classification

		TerraScan			
		Ground	Buildings	High vegetation	Low vegetation
GRASS	Category 1: terrain	87.47%	37.41%	26.11%	79.78%
	Category 2: terrain with double reflection	8.63%	1.37%	5.84%	13.14%
	Category 3: object with double reflection	2.40%	3.64%	13.86%	3.02%
	Category 4: object	1.50%	57.58%	54.19%	4.06%

Table 2.15: Overlap: percentages with respect to the automatic TerraScan classification

Table 2.14 indicates that on this dataset the GRASS filtering does not produce a well defined result; taking in consideration the category one only the 56.69%

of points falls into the TerraScan ground class, the remaining points fall mainly into the TerraScan low vegetation (10.11%) and into the TerraScan high vegetation (20.11%). The same consideration goes for the category four, for which the correspondence to the similar class in TerraScan (the building one) is only of 19.23% points; this is probably due to the fact that forestry areas were in some cases classified as object and not as object with double pulse (the overlap with the high vegetation class is 77.25%).
Table 2.15 shows that the result obtained with TerraScan is more coherent, the ground points that corresponds to the GRASS category one are 87.47%; if the building class is taken in consideration the table shows that the points that for TerraScan belong to this class for GRASS instead are divided among the terrain (category 1) and the object (category 4) classes, this fact suggest that the algorithms in GRASS had some problems with the dataset since the characteristics of these two classes are quite different. The columns that refer to low and high vegetation point out that within GRASS there is almost the total absence of an intermediate classification (category two and three) since almost the 80% of points for each TerraScan vegetation class belongs to terrain or object for GRASS.

2.4 Semi-automatic TerraScan classification

The TerraScan automatic classification, provided by OGS, was manually modified to upgrade the accuracy of the filtering result; this operation practically consists in changing the class assigned to the points; it is useful to recall that the manual editing efficiency is around 4-5 km^2 in 8 hours. Table 2.16 presents the result after the manual reclassification for the different classes, as for the automatic TerraScan procedure the number of points was reduced to the GRASS classified ones (see Table 2.10); the difference between the semi-automatic classification and the automatic one is presented, in terms of points amount, in Table 2.17, while in Figure 2.9 and in Figure 2.10 the image of the classification for the two example areas are shown. Figure 2.9 show that, despite the manual upgrade, some errors are still present in the result (buildings in the upper-right part of the image).
As Table 2.16 and Table 2.17 show in various area the classification was changed, in particular in Area 118, another difference in Area 117 consist in the introduction of the water class for the points falling into the lake (see Figure 2.9), it is also noticeable that for each area there is an increment of the unclassified points number.
The cross-comparison with the GRASS results is similar to the one obtained

for the automatic TerraScan (see Table 2.13) so it is not inserted. The TerraScan semi-automatic classification, however not so much different from the automatic one, is better than the one obtained with GRASS, so it will be used in the next step of the work, in some step as ground truth.

Class	**Area 110**	**Area 116**	**Area 117**	**Area 118**	**Area 122**	**Area 123**
Ground	529588 29.16%	699865 58.32%	447299 28.60%	456202 32.50%	260355 41.11%	479416 35.41%
Building:	125303 6.90%	74008 6.17%	239522 15.32%	182642 13.01%	73884 11.67%	90156 6.66%
Low vegetation	126413 6.96%	83143 6.93%	104845 6.70%	123770 8.82%	36300 5.73%	83605 6.18%
High vegetation	968649 53.34%	292210 24.35%	669152 42.79%	553616 39.44%	251057 39.64%	664500 49.08%
Unclassified points	66041 3.64%	50781 4.23%	97842 6.59%	87475 6.23%	11693 1.85%	36248 2.68%

Table 2.16: Semi-automatic TerraScan filtering results for each area

Class	**Area 110**	**Area 116**	**Area 117**	**Area 118**	**Area 122**	**Area 123**
Ground	-1328	-410	-5185	10847	-8	-90
Building	-9553	-663	-581	-573	-1597	-581
Low vegetation	-107	-30	0	-2577	-20	-13
High vegetation	8064	-33	581	-19082	-3	230
Unclassified points	2924	1136	0	11385	1662	454

Table 2.17: Differences between the semi-automatic and the automatic TerraScan classifications

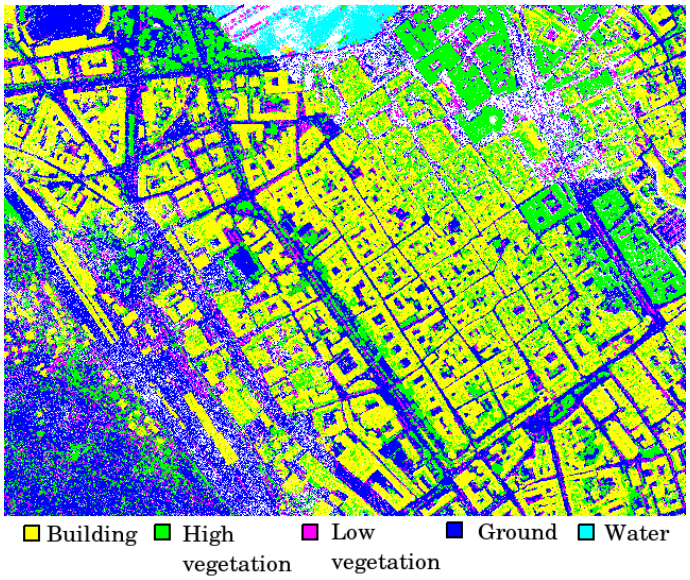

Figure 2.9: Example of the semi-automatic TerraScan classification

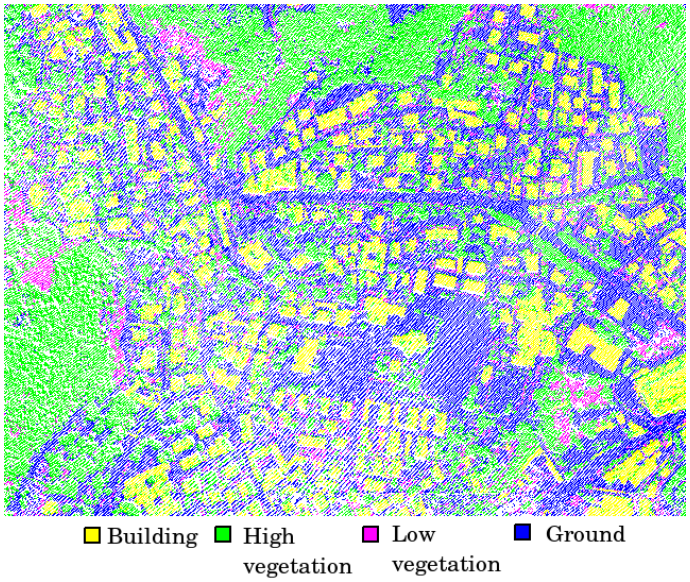

Figure 2.10: Example of the semi-automatic TerraScan classification

2.5 DEM interpolation

The step that follows the LiDAR filtering consists in the DTM and DSM computation. To interpolate the point clouds the command v.surf.bspline within GRASS was used, the algorithm allows the interpolation with bilinear or bicubic splines. The parameters to be set are the spline step in East and North direction (S_{ie}, S_{in}), the method to be used (bilinear or bicubic) and the Tykhonov regularization parameter that affects the smoothness of the result. The command can produce a gridded raster map or a vector point layer, but not simultaneously.
To produce the DTM of the area (cell 2 m $\times$ 2 m) the semi-automatic TerraScan ground points were used with spline step of 4m both in East and North direction and the default Tykhonov regularization parameter, the method use was the bilinear one.
For the DSM (cell 2 m $\times$ 2 m) the same parameters as for the DTM production were used, except for the method: in this case the bicubic one was chosen in order to better follow the shapes of man made features and vegetation, the interpolation was done on the whole set of last points available. The DTMs obtained in the two example areas are shown in Figure 2.11 and in Figure 2.12, the resulting DSMs are displayed in Figure 2.13 and Figure 2.14.

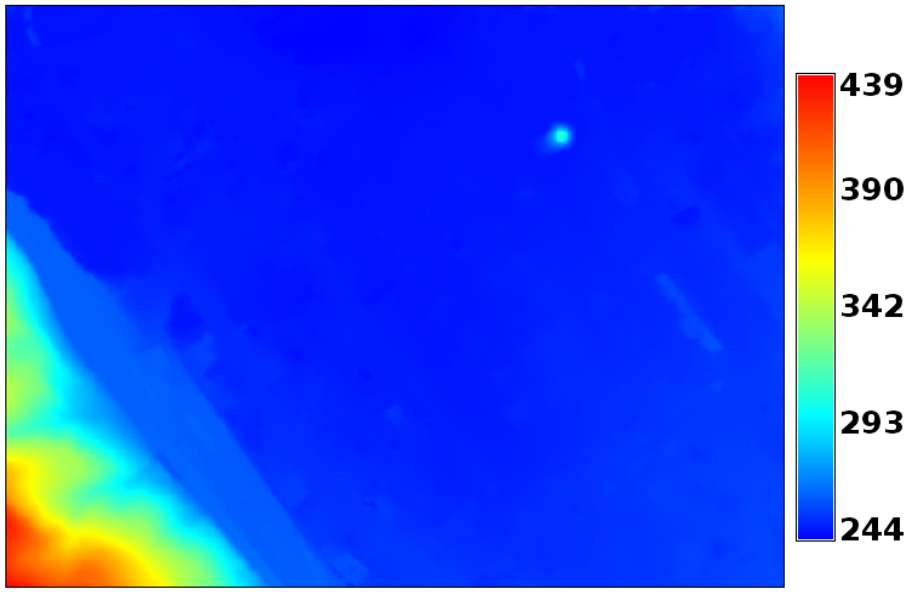

Figure 2.11: Example the intepolated DTM

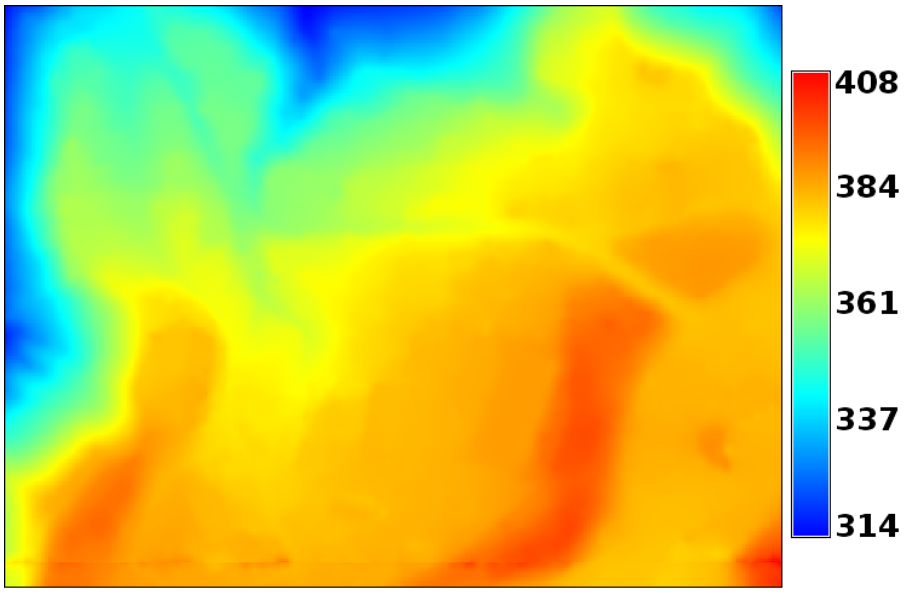

Figure 2.12: Example the intepolated DTM

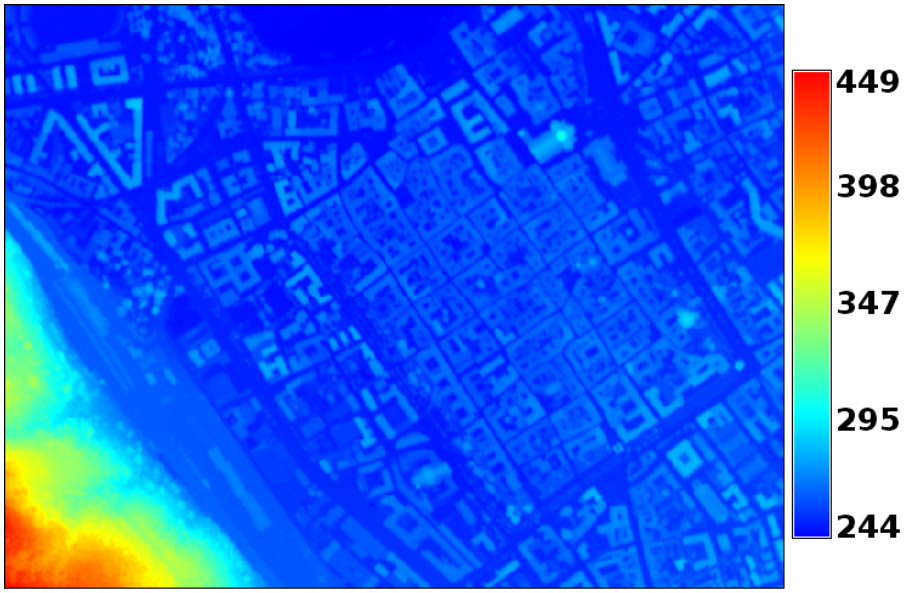

Figure 2.13: Example the intepolated DSM

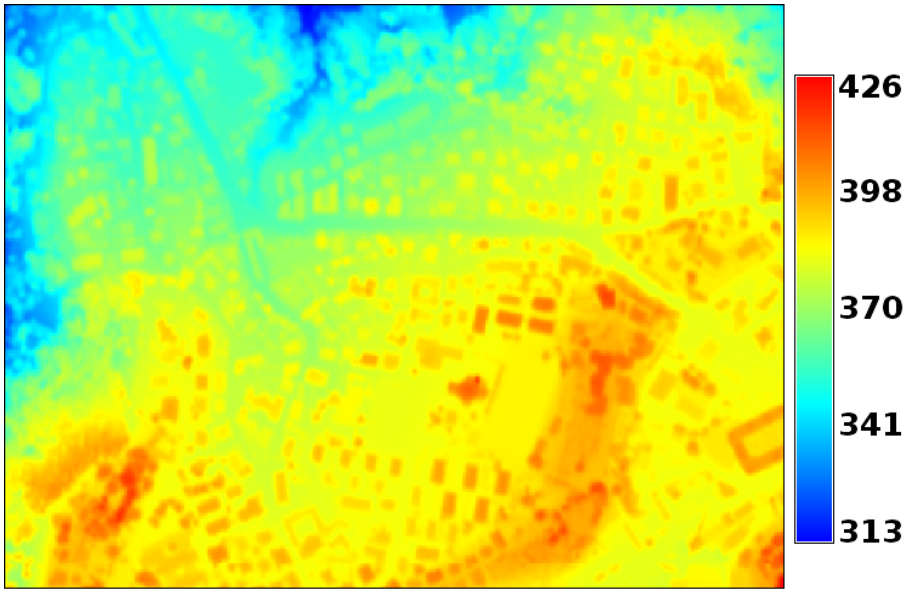

Figure 2.14: Example the intepolated DSM

Chapter 3

DEM validation

The final purpose of this work is the set up of a procedure to merge different digital elevation model; it is however necessary to assess the quality of the models available before attempting the model merging.
In this chapter the internal validation procedure used is described; in the first section the digital models available are listed and briefly described, the following sections are instead focused on the internal validation procedure used: its description and its application on the available DEMs.
The latter part of the chapter describes the external validation step that follows the internal one.

3.1 Digital model used

For the whole work it was decided to use various datasets covering the area near the walled city of Como; different models were available in the selected region. The main purpose of the work consists in the set up of a procedure to merge different digital elevation models; however before attempting to mosaic different models a validation procedure is needed in order to assess the accuracy of the data available and to reject possible outliers.
The models available were generated by different techniques:

- SRTM DSM (for further details see Section 1.1.5);
- ASTER DSM (for further details see Section 1.1.6)
- LiDAR DSM: a DSM from the LiDAR dataset available in WGS84-UTM32N projection (for further details see Section 2.5);

- LiDAR DTM: a DTM from the LiDAR dataset available in WGS84-UTM32N projection (for further details see Section 2.5);

- Photogrammetric DSM: this dataset was provided by the Lombardia Region (projection WGS84- UTM32N) and it is characterized by a 2 m cell step and a vertical nominal accuracy of 2 m.

The first step consisted then in the internal validation of each model; after that an external validation based on the LiDAR DSM was performed.

3.2 Internal validation

The first step to assess the quality of the DEMs used in this work consists in an internal validation procedure, that is the possible outlier detection using only information provided by the DEM itself, while an external validation procedure takes into consideration other informative data.
The internal validation step is performed with a package developed within the GRASS GIS software at the Laboratory of Geomatica in the Politecnico di Milano. In this section the package and the validation technique are briefly described, followed by the results obtained on the available datasets.

3.2.1 GRASS GIS internal validation: r.outldetect

The GRASS algorithm developed to perform an inner DEM validation is r.outldetect (not yet available in the official releases of the software). The main idea is to examine the entire dataset by considering sequentially only a small subset at a time; for each step the data belonging to a moving square window are taken into account while the data contained in the central pixel are handled separately; the basic hypothesis is that the values in the moving windows are observations affected by white noise.
After the choice of an interpolation method, among the available ones, and of the moving windows dimension the algorithms estimates the value of the central pixel with the selected method and computes the difference between the actual and the interpolated value. The residuals analysis, once provided a significance level, consists in statistical tests to evaluate the presence of possible outliers [Triglione, 1999].
The r.outldetect command requires different parameters to be set, apart from the input DEM:

- Output: raster output files in which the cell corresponding to outlier are substituted with the moving windows interpolated value.

- Method: type of validation: average, linear, bilinear, quadratic, bi-quadratic, bicubic, median, collocation
- Neighbourhood size: 1, 3, 5, 7, 9, 11, 13, 15, 17, 19, 21, 23, 25
- Significance value alpha: value between zero and one.
- Sites file: additional output file which contains the down-weighted sites, so points suspected to be outliers.
- Residuals: additional output file which contains the residual value between the original data and the interpolated ones.
- Binary file: additional output file in which the outlier points have value 1 while the correct points have value 0.

The key point in the validation step is the choice of method, neighbour size and the alpha value: to choose the best method for each model the program r.outldetopt was used. The choice of the alpha value is also to be done for each model, since it is used in a test for outlier identification; if the alpha value is more strict there is the possibility to identify as outlier both outlier and correct data, on the opposite situation the outlier removed are less than their total amount. For these reasons, before attempting to validate a model with this algorithm, it is better to perform an adaptive procedure to estimate the correct value of alpha to be used after the method choice.

3.2.2 Method choice: r.outldetopt

The r.outldetopt helps in the choice of the interpolation method to apply in the r.outldetect execution [Triglione, 1999]. The program, once given a digital model as input, compares different interpolation methods and provides the better one in the output; the parameters to be set are:

- Method: type of enquiry: polynomial or collocation
- Significance value alpha: only for polynomial, four choices are possible (5%, 1%, 0.1%, 0.01%).
- Wedsratio: percentage ratio for down-sampling along the W-E axis
- Nsdsratio: percentage ratio for down-sampling along the N-S axis

In this algorithm the significance level α determines the threshold for the choice between two polynomial surface with the same windows dimension.

3.2.3 Adaptive procedure with r.outldetect

As said in a previous section, the adaptive procedure is useful to determine the value of alpha to be used for model validation. The main idea is to compare the theoretical curve used in the outlier rejection test with an empirical one obtained from the model to be validated [Brovelli et al., 1999]; the curve to be generated depends on the choice of validation method and neighbourhood size: in the following the equation of the polynomial functions available in r.outdetect and their Student's t-distribution for the validation test are listed (N_k is the number of observations considered).

1. The linear surface:

$$h_{linear}(z, y) = a_0 + a_1 x + a_2 y \tag{3.1}$$

where a_0, a_1, a_2 are the three parameter to be estimated.

$$S = \sqrt{\frac{N_k}{N_k + 1}} \frac{\Delta h}{\widehat{\sigma_0}} = \sqrt{\frac{N_k}{N_k + 1}} \frac{\Delta h}{\sigma_0} \frac{\sigma_0}{\widehat{\sigma_0}} \sim \frac{Z}{\sqrt{\frac{\chi^2_{N_k-3}}{N_k - 3}}} = t_{(N_k-3)} \tag{3.2}$$

2. The bilinear surface:

$$h_{bilinear}(z, y) = a_0 + a_1 x + a_2 y + a_3 xy \tag{3.3}$$

where a_0, a_1, a_2, a_3 are the four parameter to be estimated.

$$S = \sqrt{\frac{N_k}{N_k + 1}} \frac{\Delta h}{\widehat{\sigma_0}} = \sqrt{\frac{N_k}{N_k + 1}} \frac{\Delta h}{\sigma_0} \frac{\sigma_0}{\widehat{\sigma_0}} \sim \frac{Z}{\sqrt{\frac{\chi^2_{N_k-4}}{N_k - 4}}} = t_{(N_k-4)} \tag{3.4}$$

3. The quadratic surface:

$$h_{quadratic}(z, y) = a_0 + a_1 x + a_2 y + a_3 xy + a_4 x^2 + a_5 y^2 \tag{3.5}$$

where a_0, a_1, a_2, a_3, a_4 and a_5 are the six parameter to be estimated.

$$S = \sqrt{\frac{N_k}{N_k + 1}} \frac{\Delta h}{\widehat{\sigma_0}} = \sqrt{\frac{N_k}{N_k + 1}} \frac{\Delta h}{\sigma_0} \frac{\sigma_0}{\widehat{\sigma_0}} \sim \frac{Z}{\sqrt{\frac{\chi^2_{N_k-6}}{N_k - 6}}} = t_{(N_k-6)} \tag{3.6}$$

4. The biquadratic surface:

$$h_{biquadratic}(z,y) = \begin{array}{c} a_0 + a_1x + a_2y + a_3xy + a_4x^2 + \\ +a_5y^2 + a_6x^2y + a_7xy^2 + a_8x^2y^2 \end{array} \tag{3.7}$$

where $a_0 \dots a_8$ are the nine parameter to be estimated.

$$S = \sqrt{\frac{N_k}{N_k+1}}\frac{\Delta h}{\widehat{\sigma_0}} = \sqrt{\frac{N_k}{N_k+1}}\frac{\Delta h}{\sigma_0}\frac{\sigma_0}{\widehat{\sigma_0}} \sim \frac{Z}{\sqrt{\frac{\chi^2_{N_k-9}}{N_k-9}}} = t_{(N_k-9)} \tag{3.8}$$

5. The bicubic surface:

$$h_{bicubic}(z,y) = \begin{array}{c} a_0 + a_1x + a_2y + a_3xy + a_4x^2 + a_5y^2 + a_6x^2y + \\ +a_7xy^2 + a_8x^2y^2 + a_9x^3 + a_{10}y^3 + a_{11}xy^3 + \\ +a_{12}x^3y + a_{13}x^2y^3 + a_{14}x^3y^2 + a_{15}x^3y^3 \end{array} \tag{3.9}$$

where $a_0 \dots a_{16}$ are the sixteen parameter to be estimated.

$$S = \sqrt{\frac{N_k}{N_k+1}}\frac{\Delta h}{\widehat{\sigma_0}} = \sqrt{\frac{N_k}{N_k+1}}\frac{\Delta h}{\sigma_0}\frac{\sigma_0}{\widehat{\sigma_0}} \sim \frac{Z}{\sqrt{\frac{\chi^2_{N_k-16}}{N_k-16}}} = t_{(N_k-16)} \tag{3.10}$$

Once the moving window size the number of observations N_k can be easily derived as the number of cells contained in the window a part from the central pixel; having N_k it's possible to compute de degrees of freedom needed to build the Student's t theoretical curve once an interpolation method is chosen. The empirical curve needs to be built from the actual data to be validated; to do so an algorithm similar to r.outldetect is used: the parameters to be specified are the same but, instead of the residual output map, a map containing the module of the empirical Student's t-distribution values is provided.
It is then possible to compute the cumulative distribution of the two distribution and to compare them: in Figure 3.1 one of the possible trend of the two cumulative distribution is shown, the theoretical curves is at the beginning under the empirical one until a certain probability level is reached, then the theoretical one is upon the empirical one, which implies that in the former situation the empirical curves finds more outlier than the theoretical one, so also correct data are mistaken as outliers, in the latter case the empirical distribution finds less outliers than the theoretical one, so some outlier are left in the dataset.

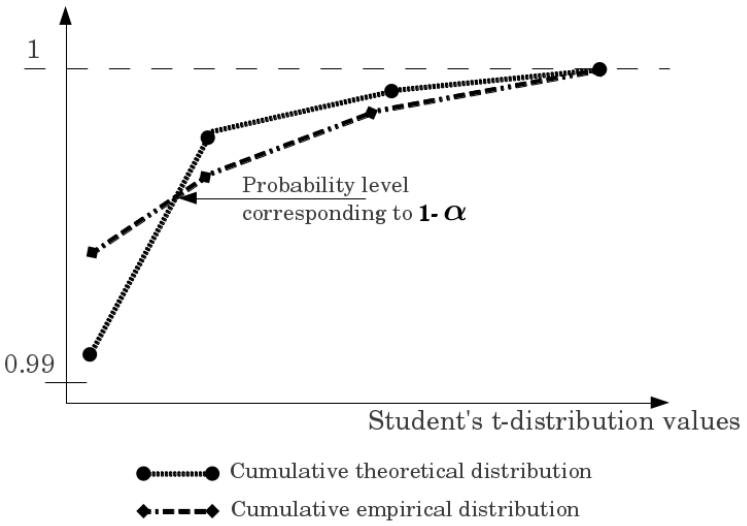

Figure 3.1: Empirical and theoretical cumulative distribution comparison

The most suitable alpha value is then found taking in consideration the probability level at which the two cumulative curves exchange their relative position, that corresponds to 1-α.

3.2.4 Digital model internal validation

In this section the results of the internal validation (carried on using r.outldetect) of the different digital models available are described. The model available in the area are the SRTM DSM, the ASTER DSM, the digital surface and terrain model obtained after the LiDAR filtering step (see Chapter 2) and a photogrammetric DSM provided by the Lombardia Region.
For each model the validation procedure is the same: at first r.outdetopt is used to find the most suitable method and the adaptive procedure to determine the value of the alpha parameter is executed, then the value obtained is used in the validation procedure to detect possible outliers.

3.2.4.1 SRTM validation

The algorithm r.outdetopt suggested the use of the bilinear surface with a moving window of size 5, so these values were used in the adaptive validation step; the results, in terms of Student's t-distribution are reported in Table 3.1 for the empirical distribution and in Table 3.2 for the theoretical one (20 degrees of freedom).

Interval	Number of points	Relative frequencies	Cumulative distribution
[0;1.5)	4921	0.75406067	0.75406067
[1.5;3)	1586	0.24302789	0.99708856
[3;4)	17	0.00260495	0.99969351
[4;∞)	2	0.00030647	1

Table 3.1: SRTM DSM: $|t_{emp}|$ frequencies and cumulative distribution

Interval	Probability	Number of points	Cumulative Distribution
[0;1.5)	0.85076423	5551	0.85076423
[1.5;3)	0.14215986	928	0.99292409
[3;4)	0.00637236	42	0.99929645
[4;∞)	0.00070351	5	1

Table 3.2: SRTM DSM: $|t_{teo}|$ frequencies and cumulative distribution

In Figure 3.2 the comparison between the two cumulative distribution is shown, the graphic show a behaviour opposite to the one represented in Figure 3.1: at first the theoretical cumulative distribution is over the empirical one and then their relative position is switched, the alpha value is however found considering the intersection point at which corresponds a probability of 0.988, so a value of α around 0.01.

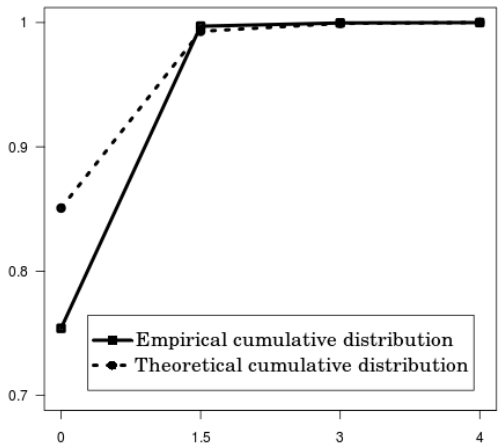

Figure 3.2: SRTM DSM: comparison between the two distributions

The validation was then carried on using r.outldetect with the value of alpha obtained in the previous step, 59 outlier were found upon 7676 cells; in Figure 3.3 the residuals between the bilinear interpolation computed for each cell and the original data are plotted, while Figure 3.4 show the validated SRTM model.

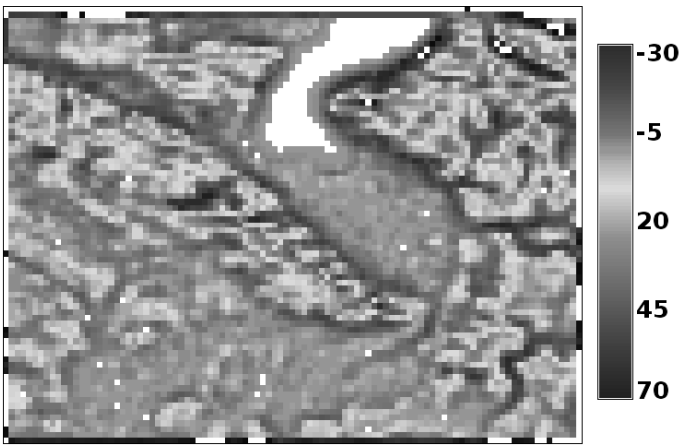

Figure 3.3: Residuals between SRTM and the bilinear interpolation

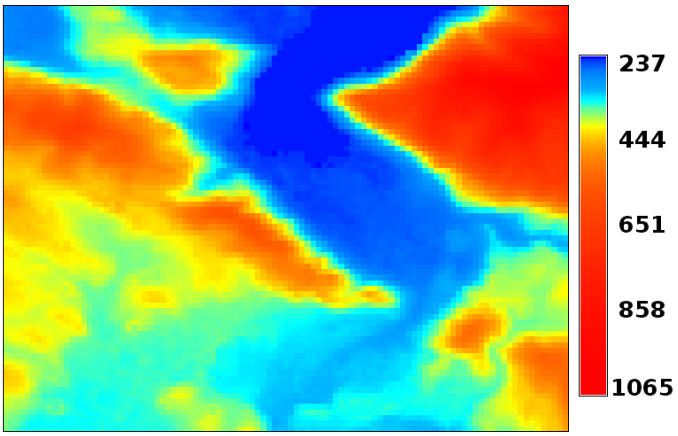

Figure 3.4: Validated SRTM model

3.2.4.2 ASTER validation

As for the previous digital model considered, the program to find the optimum method suggested the use of a bilinear surface with a window of 5 × 5 cells. Concerning the alpha value estimation, the Student's t-distribution are

reported in Table 3.3 for the empirical distribution and in Table 3.4 for the theoretical one (20 degrees of freedom).

Interval	Number of points	Relative frequencies	Cumulative distribution
[0;1.5)	19810	0.60306250	0.60306250
[1.5;3)	13025	0.39651131	0.99957381
[3;4)	12	0.00036531	0.99993912
[4;∞)	2	0.00006088	1

Table 3.3: ASTER DSM: $|t_{emp}|$ frequencies and cumulative distribution

Interval	Probability	Number of points	Cumulative Distribution
[0;1.5)	0.85076423	27947	0.85076423
[1.5;3)	0.14215986	4670	0.99292409
[3;4)	0.00637237	209	0.99929646
[4;∞)	0.00070351	23	1

Table 3.4: ASTER DSM: $|t_{teo}|$ frequencies and cumulative distribution

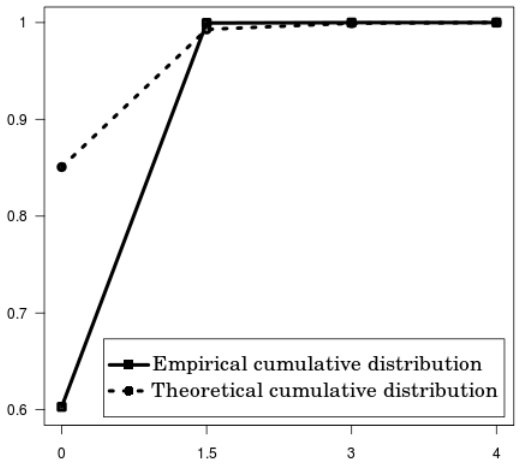

Figure 3.5: ASTER DSM: comparison between the two distributions

The graphic displaying the two cumulative curves is similar to the one obtained with the SRTM DSM in terms of relative position between the two lines

(Figure 3.5); the value of α is then around 0.01 since the probability level corresponding to the intersection point is 0.989.
In the validation step 136 outlier over 70380 cells were found, it may be useful to recall that value of the cells marked as outliers are substituted with the interpolation computed with the method selected in r.outldetect (in the specific case the bilinear model); Figure 3.6 shows the residuals between the original data and the bilinear interpolation, while Figure 3.7 shows the validated ASTER DSM model.

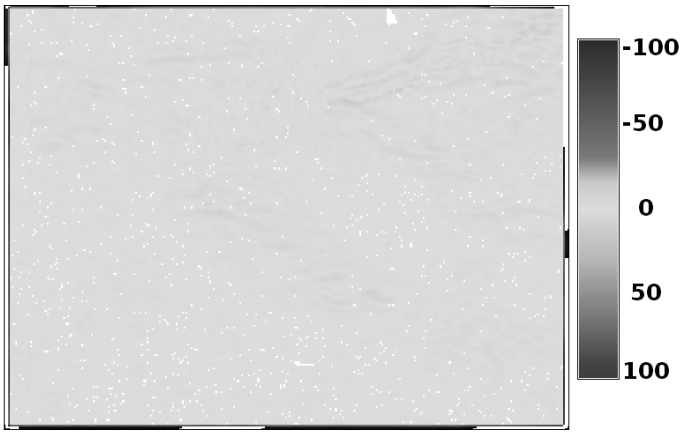

Figure 3.6: Residuals between ASTER and the bilinear interpolation

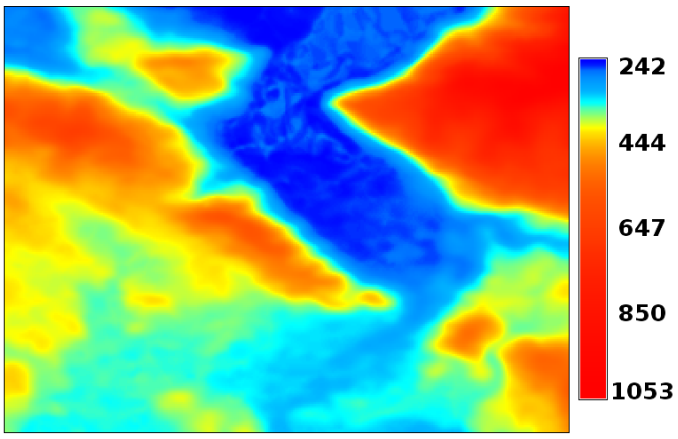

Figure 3.7: Validated ASTER DSM model

3.2.4.3 Photogrammetric DSM validation

Also in this case the method selected by r.outdetopt is the bilinear one with a window of 5 × 5 cells size. The procedure to validate internally this model is the same used for the ASTER and the SRTM DSM; the Student's t-distribution are reported in Table 3.5 for the empirical data and in Table 3.6 for the theoretical curve (20 degrees of freedom).

Interval	**Number of points**	**Relative frequencies**	**Cumulative distribution**
[0;3)	2481143	0.99636013	0.99636013
[3;5)	8502	0.00341416	0.99977429
[5;7)	399	0.00016023	0.99993452
[7;10)	62	0.00002490	0.99995942
[10;50)	96	0.00003854	0.99999796
[50;∞)	5	0.00000201	1

Table 3.5: Photogrammetric DSM: $|t_{emp}|$ frequencies and cumulative distribution

Interval	**Probability**	**Number of points**	**Cumulative Distribution**
[0;3)	0.9929241012	2472587	0.9929241012
[3;5)	0.0070071685	17449	0.99993127
[5;7)	0.0000678704	169	0.99999914
[7;10)	0.0000008561	2	0.999999996
[10;50)	0.0000000032	0	0.999999999
[50;∞)	0	0	1

Table 3.6: Photogrammetric DSM: $|t_{teo}|$ frequencies and cumulative distribution

The two cumulative curves (Figure 3.8) show a pattern similar to the one indicated in Figure 3.1; the value of alpha is determined by considering the point of intersection between the two curves, since the probability level of the intersection is 0.999772118 the value of the parameter α is around $2 \cdot 10^{-4}$.

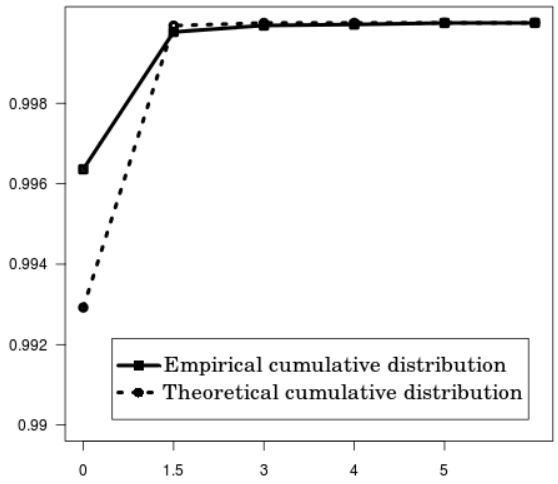

Figure 3.8: Photogrammetric DSM: comparison between the two distributions

After the validation step 900 cells were identified as outliers over 12264435 cells and their value was substituted with the one derived from the bilinear interpolation of the twenty-four neighbour data; the image of the residual between the original DSM and the bilinear interpolation values is presented in Figure 3.9, while the validated photogrammetric DSM is shown in Figure 3.10.

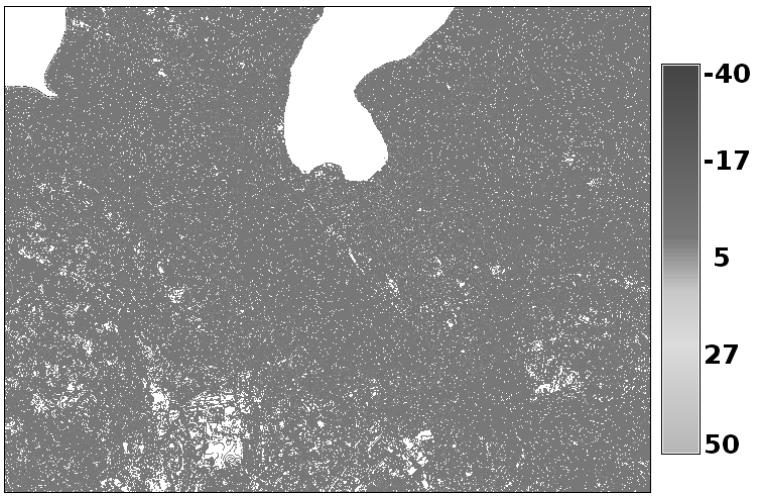

Figure 3.9: Residuals between the photogrammetric DSM and the bilinear interpolation

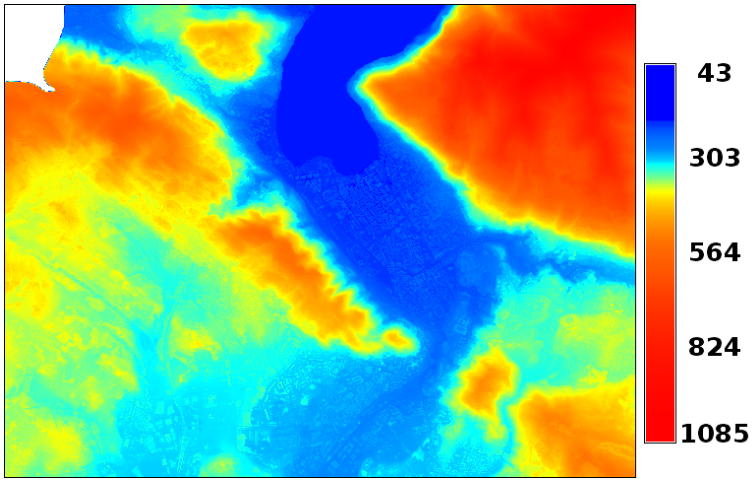

Figure 3.10: Validated photogrammetric DSM model

3.2.4.4 LiDAR DSM validation

The execution of r.outdetopt for the LiDAR DSM gave as optimum interpolation model to choose the biquadratic one with a 7×7 cells windows. The adaptive analysis of the DSM LiDAR produced the Student's t-distribution value available in Table 3.7, the theoretical distribution values (39 degrees of freedom) are instead available in Table 3.8; Figure 3.11 show the graphic displaying the trend of the two cumlative distribution. From the intersection between the two lines (probability equal to 0.993515) the value of α equal to 0.006 was obtained.

Interval	Number of points	Relative frequencies	Cumulative distribution
[0;1.5)	356997	0.74348817	0.74348817
[1.5;3)	121650	0.25335041	0.99683858
[3;4)	1447	0.00301354	0.99985212
[4;5)	55	0.00011454	0.99996666
[5;∞)	10	0.00003332	1

Table 3.7: DSM from LiDAR: $|t_{emp}|$ frequencies and cumulative distribution

Interval	Probability	Number of points	Cumulative Distribution
[0;1.5)	0.85833296	412141	0.85833296
[1.5;3)	0.13698047	65773	0.99531343
[3;4)	0.00441271	2119	0.99972614
[4;5)	0.00026133	125	0.99998747
[5;∞)	0.00001252	6	1

Table 3.8: DSM from LiDAR: $|t_{teo}|$ frequencies and cumulative distribution

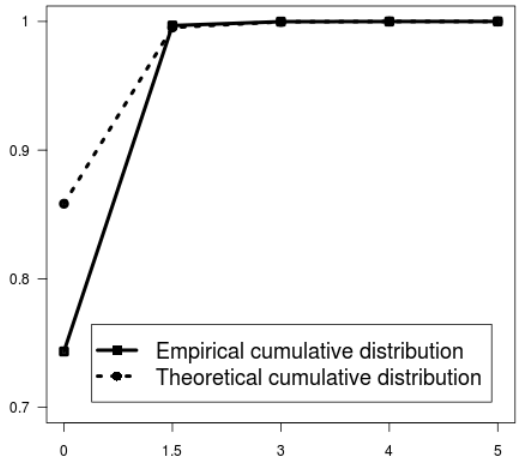

Figure 3.11: DSM from LiDAR: comparison between the two distributions

The validation phase was carried on with the value of α from the previous step; 3148 cells were identified as outliers over the total amount of 5949414 non null cells, Figure 3.12 contains the residual map and Figure 3.13 the validated DSM from LiDAR data.

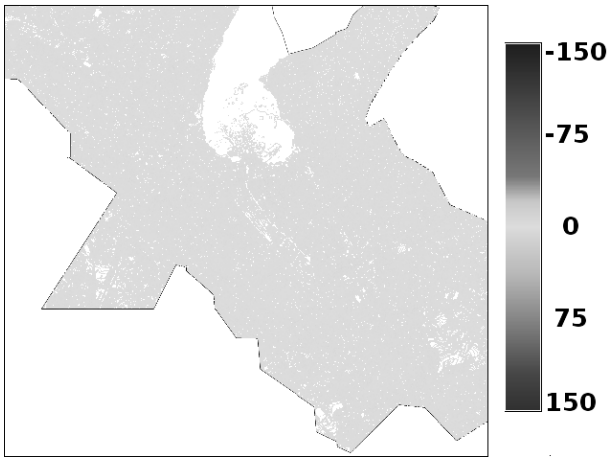

Figure 3.12: Residuals between the DSM from LiDAR and the bilinear interpolation

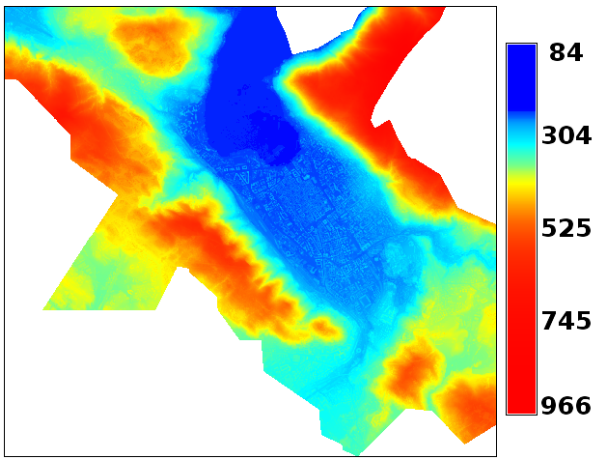

Figure 3.13: Validated LiDAR DSM model

3.2.4.5 LiDAR DTM validation

The algorithm r.outdetopt suggested the use of a biquadratic interpolating surface with a 5×5 dimension moving windows; these values were used for the adaptive analysis of the DTM LiDAR which gave the results presented in Table 3.9 that contains the empirical distribution values and in Table 3.10 that contains the theoretical ones (15 degrees of freedom); in Figure 3.14 the trend of the two cumulative curves is shown. From the intersection between the two

lines (probability equal to 0.998953) the value of α equal to 0.001 was obtained.

Interval	Number of points	Relative frequencies	Cumulative distribution
[0;1.5)	78721	0.88749717	0.88749717
[1.5;3)	9847	0.11101466	0.99851183
[3;4)	37	0.00041714	0.99892897
[4;5)	19	0.00021421	0.99914318
[5;∞)	76	0.00085681	1

Table 3.9: DTM from LiDAR: $|t_{emp}|$ frequencies and cumulative distribution

Interval	Probability	Number of points	Cumulative Distribution
[0;1.5)	0.84563334	75008	0.84563334
[1.5;3)	0.14539392	12896	0.99102726
[3;4)	0.00781341	693	0.99884067
[4;5)	0.00100095	89	0.99984162
[5;∞)	0.00015837	14	1

Table 3.10: DTM from LiDAR: $|t_{teo}|$ frequencies and cumulative distribution

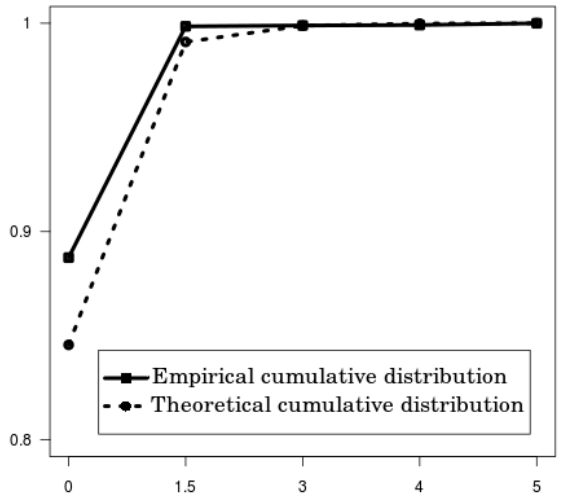

Figure 3.14: DTM from LiDAR: comparison between the two distributions

After the validation step 95 cells were identified as outliers over the total amount of 5949414 non null cells, Figure 3.15 contains the residual map and Figure 3.16 the validated digital terrain model.

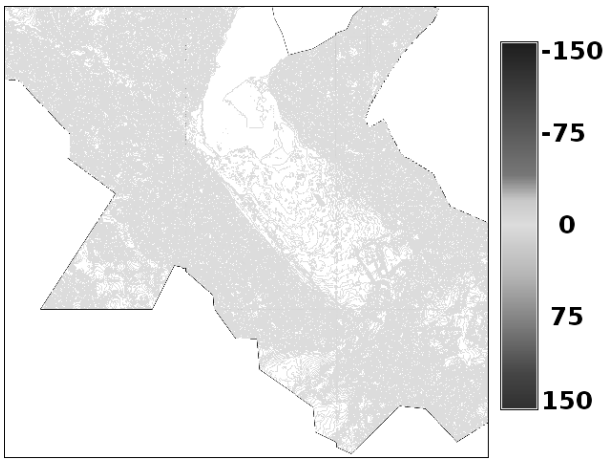

Figure 3.15: Residuals between the DTM from LiDAR and the bilinear interpolation

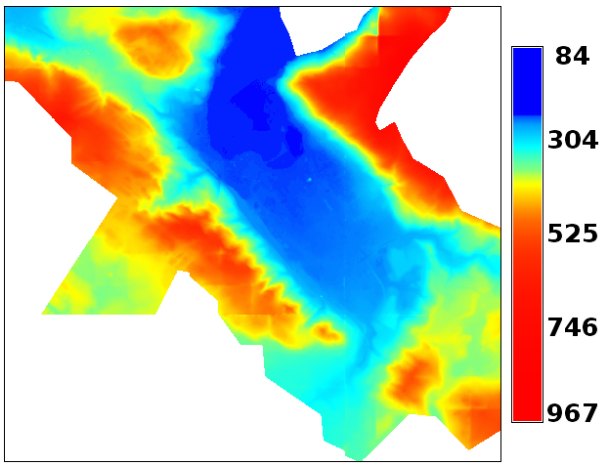

Figure 3.16: Validated LiDAR DTM model

3.2.4.6 Results summary

All the available DEMs were validated using the tools r.outdetopt and r.outldetect; for all the DEMs the outlier are spread in the area, so it is

not possible to associate them to the presence of hills or steep slopes.

Model	Interpolation method	Window size	Degrees of freedom	α value
SRTM DSM	bilinear	5×5	20	0.01
ASTER DSM	bilinear	5×5	20	0.01
Photogrammetric DSM	bilinear	5×5	20	$2 \cdot 10^{-4}$
LiDAR DSM	biquadratic	7×7	39	0.006
LiDAR DTM	biquadratic	5×5	15	0.001

Table 3.11: Model interpolation method - summary

In Table 3.11 the methods chosen for the different digital model are sum up, while Table 3.12 contains the final results concerning outlier detection.

Model	Outlier number	Total cell number	Percentage of outlier
SRTM DSM	59	7676	0.77%
ASTER DSM	136	70380	0.19%
Photogrammetric DSM	900	12264635	0.007%
LiDAR DSM	3148	5949414	0.053%
LiDAR DTM	95	5949514	0.0016%

Table 3.12: Model interpolation method - summary

3.3 External validation

After performing the internal validation an external validation phase was executed on the SRTM and ASTER DSMs; the external validation is useful to assess the actual accuracy of the DSM in the analysed area with respect to the nominal accuracy provided.
For this validation step it is necessary to compare the DSMs with a more accurate one corresponding to the terrain truth: in this work the LiDAR validated DSM was used.
Before performing the external validation the SRTM and ASTER models

were converted into the WGS84-UTM32N reference system to be compared with the LiDAR DSM using the conversion software "GK2CNV" developed by the Politecnico di Torino; after the coordinates conversion of the grid nodes the SRTM and ASTER grid were recreated by a bilinear spline interpolation with step respectively of 90 m and 30 m.
The LiDAR DSM was resampled to have the spatial grid resolution equal to the one of the DSM under validation:

- SRTM: the LiDAR DSM value corresponding to a SRTM cell was obtained as the mean value of all the original 2 m $\times$ 2 m cells falling into it; the mean value was used since the SRTM value, obtained from SAR technology, is an average value, too.

- ASTER: the LiDAR DSM value considered in this case is the one belonging to the cell nearest to the center of the ASTER one; for the ASTER the average value was not used since the ASTER, derived from satellite photogrammetry, consists of point-wise observations.

These models are used also in the morphology analysis and for the merging procedure.
The ASTER and the SRTM were then compared to the LiDAR ones, and the mean of the squared differences was compared to the nominal accuracy value; in Table 3.13 the results are presented: the SRTM DSM is compliant with the nominal accuracy value since the nominal accuracy value is greater than the one obtained from the datasets comparison; the ASTER DSM, instead, has a nominal accuracy value lower than the computed one, so it is less reliable than the SRTM DSM; it is however considered validated since its nominal accuracy can vary until the value of 20 m at 95%.

Model	**Nominal accuracy (m)**	**Accuracy from LiDAR comparison (m)**
SRTM DSM	16	13.20
ASTER DSM	10	12.32

Table 3.13: External validation - results

An advanced external validation phase is described in the next chapter, since the SRTM and ASTER DSMs will be analysed in function of the terrain morphology.

Chapter 4

Analysis of variance

In this chapter the digital model dependences on terrain characteristics are evaluated by means of the two way ANalysis Of VAriance (ANOVA) statistical procedure. The former sections of the chapter pertain to the ANOVA definition and the description of the test used for model comparison, in the latter part the results of the analysis obtained for the SRTM and the ASTER DSMs are described.

4.1 Analysis of variance

After the DEMs validation, and before attempting the DEMs merging, it is useful to assess whether the model depends on the terrain characteristics, in particular on slope gradient and aspect; this is useful also in view of the model merging to assign different weights as a function of the feature which the model depends on.
The main morphological terrain characteristics considered are the slope gradient and aspect (for their definition see Section 1.3) that were computed on the DSM from LiDAR data considered as ground truth. To assess the DSM dependences on these two features a variance analysis procedure (ANOVA) was set up [Sansó, 1993]; this procedure gives the possibility to compare two models in which the former depends on the two characteristics while in the latter only one feature influences its behaviour.
In the simplest ANOVA formulation the two features are classified in various classes for which an observation value is given. If each class contains more than one observation it is possible to built up the analysis of variance using each class mean value as representative observation for the whole class; this, however, is possible only if the classes have the same size. Unfortunately, in this work the classes do not fulfil this requirement, so in the next section the

two way ANOVA is developed considering classes with variable size.

4.2 Two way ANOVA

In the two way ANOVA the observations y_0 are classified accordingly two concomitant factors A, B.

$$\begin{aligned} A &= A_1, A_2, \ldots, A_q \\ B &= B_1, B_2, \ldots, B_p \end{aligned} \tag{4.1}$$

The observations follow the model described in Formula 4.2, while the corresponding variance-covariance matrix can be written in two different ways: if the class size is constant the variance of each class will be constant and equal to σ_0^2 (Formula 4.3), otherwise it will also depend on the class size (Formula 4.4).

$$E\{y_{0ij}\} = \alpha_i + \beta_j \qquad (i = 1,\ldots,q),\ (j = 1,\ \ldots,p) \tag{4.2}$$

$$C_{y_0 y_0} = \sigma_0^2 I \tag{4.3}$$

$$C_{y_0 y_0} = \sigma_0^2 Q \tag{4.4}$$

Q is a diagonal matrix containing the inverse of the number of data (N_{ij}) for each class as:

$$N_{1,1} \ldots N_{1,p} \ldots N_{q,p} \tag{4.5}$$

In both cases it is assumed that the observations are independent from each other since their variance-covariance matrices are diagonal (Formula 4.3 and 4.4). To assess model dependencies on the factors A and B, two statistical tests are needed: in the former the hypothesis H_0 under test states that the factor A does not have any influence on the observations (Formula 4.6); the latter will test the same but for the factor B. These hypothesis are tested comparing the full parametrized model with one depending only on one of the two factors.

$$H_0 : \alpha_1 = \alpha_2 = \cdots = \alpha_q \tag{4.6}$$

Before solving the least squares system and setting up the two tests it is necessary to point out that the system itself is over-parametrized; in fact the observations (Formula 4.2) are functions of α_i and β_i but it is not possible to discriminate their contribution apart.
For this reason, the imposition of an arbitrary constraint (Formula 4.7) is necessary to carry out the compensation to obtain a particular $\widehat{\alpha}$, $\widehat{\beta}$ solution.

$$\beta_1 = 0 \tag{4.7}$$

In the next sections the full model and the two reduced ones and their corresponding tests will be described.

4.2.1 Full model

The full data model can be summarized into two tables, the former (4.8) containing the observations (mean values representative for each class) and the latter (4.9) containing the number of data for each class (where S_{RC} is the total number of data).

Observations table:

	β_1	β_2	$\dots$	β_p
α_1	$y_{0,1,1}$	$y_{0,1,2}$	$\dots$	$y_{0,1,p}$
α_2	$y_{0,2,1}$	$y_{0,2,2}$	$\dots$	$y_{0,2,p}$
$\dots$	$\dots$	$\dots$	$\dots$	$\dots$
α_q	$y_{0,q,1}$	$y_{0,q,2}$	$\dots$	$y_{0,q,p}$

(4.8)

Size table:

	β_1	β_2	$\dots$	β_p	$Sum(R_i):$
α_1	$n_{1,1}$	$n_{1,2}$	$\dots$	$n_{1,p}$	R_1
α_2	$n_{2,1}$	$n_{2,2}$	$\dots$	$n_{2,p}$	R_2
$\dots$	$\dots$	$\dots$	$\dots$	$\dots$	$\dots$
α_q	$n_{q,1}$	$n_{q,2}$	$\dots$	$n_{q,p}$	R_q
$Sum(C_j):$	C_1	C_2	$\dots$	C_p	S_{RC}

(4.9)

In the full model both the two characteristics are supposed to influence the observations:

$$y_{0ij} = \alpha_i + \beta_j + \nu_{ij} \tag{4.10}$$

In order to perform the Fisher F test for the model comparisons it is necessary to obtain an estimation of the model variances, this will be done carrying on a least squares adjustment in which the parameters to be determined are the weight of the factors A_i and B_j; since the constraint imposed was $\beta_1 = 0$ the first β value to be estimated is the β_2.

$$\underline{\widehat{x}} = \begin{bmatrix} \alpha_1 \\ \vdots \\ \alpha_i \\ \vdots \\ \alpha_q \\ \beta_2 \\ \vdots \\ \beta_j \\ \vdots \\ \beta_p \end{bmatrix} \tag{4.11}$$

Once defined the design matrix A the least squares solution can be obtained as:

$$\begin{aligned} \underline{\hat{x}} &= N^{-1}\underline{T}_n \\ \underline{\hat{y}} &= A\underline{\hat{x}} \end{aligned} \tag{4.12}$$

where:

$$\begin{aligned} N &= A^T Q^{-1} A \\ \underline{T}_n &= A^T Q^{-1} \underline{y}_0 \end{aligned} \tag{4.13}$$

The residuals vector and the estimated variance are then computed as:

$$\underline{\hat{\nu}} = \underline{y}_0 - \underline{\hat{y}} \tag{4.14}$$

$$\hat{\sigma}_0^2 = \frac{\underline{\hat{\nu}}^T Q^{-1} \underline{\hat{\nu}}}{n-m} \tag{4.15}$$

where n is the number of observations and m the number of parameters to be estimated.
The matrix N, whose dimension depends on p and q values and it is indicated inside the squared brackets, can be written using the notation defined in Formula 4.9:

$$N_{[(q+p-1)\times(q+p-1)]} = \begin{vmatrix} N_{11} & N_{12} \\ N_{21} & N_{22} \end{vmatrix} =$$

$$\begin{vmatrix} R_1 & 0 & \dots & \dots & 0 & n_{12} & \dots & n_{1j} & \dots & n_{1p} \\ 0 & R_2 & \dots & \dots & \vdots & n_{22} & \dots & n_{2j} & \dots & n_{2p} \\ \vdots & \dots & \ddots & \dots & \vdots & \vdots & \dots & \vdots & \dots & \vdots \\ \vdots & \dots & \dots & \ddots & \vdots & \vdots & \dots & \vdots & \dots & \vdots \\ 0 & \dots & \dots & \dots & R_q & n_{q2} & \dots & n_{qj} & \dots & n_{qp} \\ n_{12} & \dots & n_{i2} & \dots & n_{q2} & C_2 & 0 & \dots & \dots & 0 \\ n_{13} & \dots & n_{i3} & \dots & n_{q3} & 0 & C_3 & \dots & \dots & \vdots \\ \vdots & \dots & \vdots & \dots & \vdots & \vdots & \dots & \ddots & \dots & \vdots \\ \vdots & \dots & \vdots & \dots & \vdots & \vdots & \dots & \dots & \ddots & \vdots \\ n_{1p} & \dots & n_{ip} & \dots & n_{qp} & 0 & \dots & \dots & \dots & C_p \end{vmatrix} \tag{4.16}$$

The vector $\underline{T}_n$, using the same notation, can be written as:

$$\underline{T}_{n[(q+p-1)\times 1]} = \left|\begin{matrix}\underline{a}\\ \underline{b}\end{matrix}\right| = \left|\begin{matrix} R_1 a_1 \\ R_2 a_2 \\ \vdots \\ R_q a_q \\ C_2 b_2 \\ C_3 b_3 \\ \vdots \\ C_p b_p \end{matrix}\right| \tag{4.17}$$

where the terms a_i and b_j are:

$$\begin{aligned} a_i &= \frac{\sum_{j=2}^{p} n_{ij} y_{ij}}{R_i} \\ b_j &= \frac{\sum_{i=1}^{q} n_{ij} y_{ij}}{C_j} \end{aligned} \tag{4.18}$$

The analytical solution of the least squares system should be obtained as:

$$\begin{cases} \underline{\alpha} = N_{11}^{-1}\underline{a} - N_{11}^{-1} N_{12}\underline{\beta} \\ \left(N_{22} N_{21} N_{11}^{-1}\right)\underline{\beta} = \underline{b} - N_{21} N_{11}^{-1}\underline{a} \end{cases} \tag{4.19}$$

All the least squares adjustments were solved using the statistical programming language R[1] after the definition of the design matrix A and the observation vector $\underline{y}_0$.

4.2.2 The test for model comparison

The model containing all the parameters should then be compared with the models regulated only by the first or the second classification factor (factor A and B), that is to hypothesize that the factor A (or B) does not influence the model behaviour.
The model taken into consideration for the test are always the full parametrized one (with variance σ_{0f}^2 and m_f parameters) and one with a reduced number of parameters (with variance σ_{0r}^2 and m_r parameters); the models variances are unknown, so the least squares estimated variances are used instead:

$$\frac{\hat{\sigma}_{0f}^2}{\sigma_{0f}^2} \sim \chi_{n-m_f}^2 \tag{4.20}$$

$$\frac{\hat{\sigma}_{0r}^2}{\sigma_{0r}^2} \sim \chi_{n-m_r}^2 \tag{4.21}$$

[1] http://www.r-project.org/

The test verifies the hypothesis that the fitting of the data does not depend on the model left out parameters:

$$H_0 : \sigma_{0f}^2 = \sigma_{0r}^2 = \sigma_0^2 \tag{4.22}$$

The value to be compared with the theoretical one follows a Fisher F with $(m_f - m_r,\, n - m_f)$ degree of freedom, where n corresponds to the number of observations:

$$\frac{\hat{\sigma}_{0r}^2(n - m_r) - \hat{\sigma}_{0f}^2(n - m_f)}{\hat{\sigma}_{0f}^2(n - m_f)} \sim \frac{\dfrac{\chi^2_{m_f - m_r}}{m_f - m_r}}{\dfrac{\chi^2_{n-m_f}}{n - m_f}} = F_{m_f - m_r, n - m_f} \tag{4.23}$$

The theoretical F value (Figure 4.1) corresponds to the abscissa after which the α percentage of distribution is left, where α corresponds to the significance level of the test, and it is read from tables.

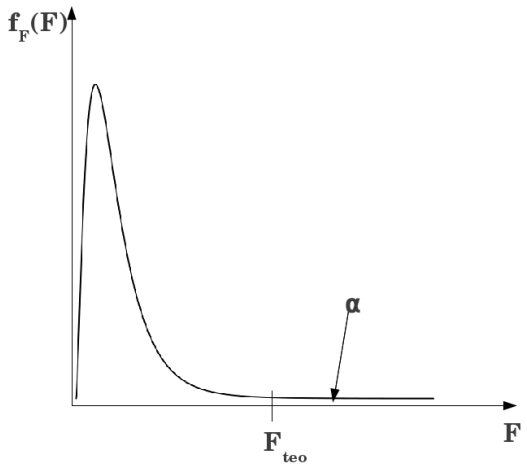

Figure 4.1: Theoretical F value

The empirical F value is instead computed directly from the data by substituting in the left part of Formula 4.23 the actual values. Once decided the significance level α the value of the Fisher F theoretical value (F_{teo}) can be computed and compared to the empirical one (F_{emp}):

- $F_{emp} > F_{teo} \longrightarrow$ The hypothesis that a parameters set does not influence the model is rejected, so the model behaviour depends on both of them.
- $F_{emp} < F_{teo} \longrightarrow$ The hypothesis is verified, so the model can be described using less parameters.

4.2.3 First hypothesis: A does not influence the model

The first model to be compared with the full one is built under the hypothesis that the factor A does not influence the observations, that is to write H_0 as:

$$H_0 : \alpha_1 = \alpha_2 = \cdots = \alpha_q \tag{4.24}$$

under this hypothesis and the constraint on the value β_1 the normal matrix N, following the notation specified in Formula 4.9, can be written as:

$$N_{[p\times p]} = \begin{vmatrix} S_{RC} & C_2 & C_3 & \dots & C_p \\ C_2 & C_2 & 0 & \dots & 0 \\ \vdots & 0 & \ddots & \dots & \vdots \\ \vdots & \vdots & \dots & \ddots & \vdots \\ C_p & 0 & \dots & \dots & C_p \end{vmatrix} \tag{4.25}$$

while the vector T_n will be:

$$\underline{T}_{n[p\times 1]} = \begin{vmatrix} a \\ \underline{b} \end{vmatrix} = \begin{vmatrix} S_{RC} y_{RC} \\ C_2 b_2 \\ C_3 b_3 \\ \vdots \\ C_p b_p \end{vmatrix} \tag{4.26}$$

where

$$y_{RC} = \frac{\sum_{i,j}^{q,p} n_{i,j} y_{i,j}}{\sum_{i,j}^{p,q} n_{i,j}} \tag{4.27}$$

The number of parameters to be estimated is p, since there is only an α value and $(p-1)$ β; the empirical Fisher F value is computed as:

$$\frac{\hat{\sigma}^2_{0r}(n-p) - \hat{\sigma}^2_{0f}(n-(q+p-1))}{\hat{\sigma}^2_{0f}(n-(q+p-1))} \sim F_{(q-1),n-(q+p-1)} \tag{4.28}$$

Once decided the significance level α it is possible to compare the two Fisher F values and verify the hypothesis.

4.2.4 Second hypothesis: B does not influence the model

The other model to be tested is the one in which only the factor A is supposed to influence the model; as before, the hypothesis to be tested is that B does not influence the model behaviour:

$$H_0 : \beta_1 = \beta_2 = \cdots = \beta_p \tag{4.29}$$

under this hypothesis the normal matrix N can be written as:

$$N_{[q\times q]} = \begin{vmatrix} R_1 & 0 & \dots & 0 \\ 0 & \ddots & \dots & \vdots \\ \vdots & \dots & \ddots & \vdots \\ 0 & \dots & \dots & R_q \end{vmatrix} \tag{4.30}$$

while the vector $\underline{T}_n$ is:

$$\underline{T}_{n[q\times 1]} = \left|\underline{a}\right| = \begin{vmatrix} R_1 a_1 \\ R_2 a_2 \\ \vdots \\ R_q a_q \end{vmatrix} \tag{4.31}$$

The parameters to be estimated under the hypothesis H_0 are the whole set of α values, so q values; in this situation the theoretical Fisher F value is similar to:

$$\frac{\hat{\sigma}^2_{0r}(n-q) - \hat{\sigma}^2_{0f}(n-(q+p-1))}{\hat{\sigma}^2_{0f}(n-(q+p-1))} \sim F_{(p-1),n-(q+p-1)} \tag{4.32}$$

Again the hypothesis should be verified after the choice of a significance level α.

4.3 Data analysis

As written in the introduction of this chapter, the ANOVA analysis is used to verify possible DEM's dependences on the terrain morphology (slope gradient and aspect).
In the following the factor A and B, used to describe the ANOVA procedure, correspond to the slope gradient and aspect of the area.
The slope gradient and aspect classes were defined upon the DSM from LiDAR data while the models tested were the SRTM and the ASTER ones obtained after the external validation step (see Section 3.3). The resampled LiDAR DSM were used then to compute the gradient and aspect maps using a tool available in GRASS GIS: r.slope.aspect; at first the two morphological maps (gradient and aspect) were classified, i.e. subdivided into different classes, then classes corresponding to all the possible combinations of the two classifications were created; for each class the difference between LiDAR DSM and the model under test was computed and the mean value of the squared difference was taken into account as class observation.

4.3.1 SRTM analysis

The ANOVA analysis on the SRTM was performed considering sixteen classes:

- the slope gradient was divided into four classes (Figure 4.2); the 25%, 50% and 75% gradient map percentiles were chosen as interval extremes:
  - 0 - 3°
  - 3° - 10°
  - 10° - 20°
  - greater than 20°
- the slope aspect was divided into four classes of 90 degrees each (Figure 4.3):
  - 0 - 90° (NE)
  - 90° - 180° (NW)
  - 180° - 270° (SW)
  - 270° - 360° (SE)

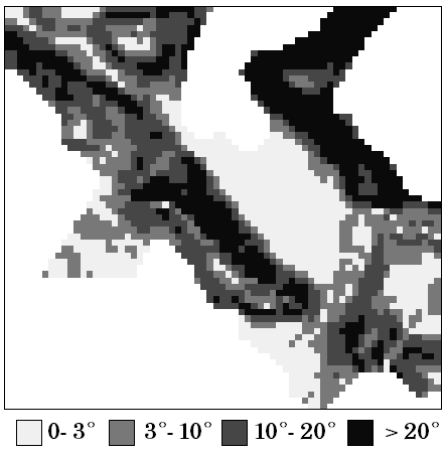

Figure 4.2: SRTM: slope gradient classification

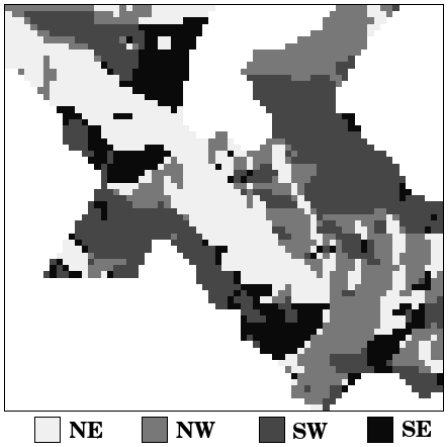

Figure 4.3: SRTM: slope aspect classification

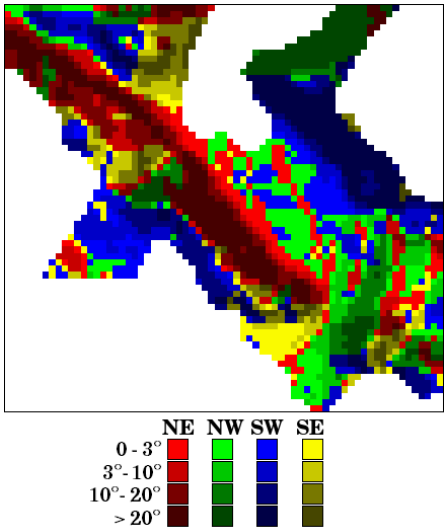

Figure 4.4: SRTM: classification combination map

As written before a final map was created from the combination of the two single classifications in correspondence of the LiDAR data (see Figure 4.4) since the observation values will refer to the differences between the LiDAR and the SRTM DSMs.
In Table 4.1 the absolute frequency of the sixteen classes is shown; these value are used to populate the Q matrix.

		Aspect			
		NW	SW	SE	NE
Gradient	0 - 3°	224	176	99	174
	3° - 10°	120	216	99	137
	10° - 20°	121	183	109	199
	> 20°	171	218	53	225

Table 4.1: SRTM: absolute frequencies

The squared mean value obtained from the difference between SRTM and LiDAR DSM is shown in Table 4.2; these values are used in the two way ANOVA analysis to define the observation vector ($\underline{y}_0$).

		Aspect			
		NW	SW	SE	NE
Gradient	0 - 3°	9.36	13.91	18.32	9.00
	3° - 10°	48.02	91.97	41.99	56.55
	10° - 20°	94.48	245.86	79.74	132.48
	> 20°	206.78	819.68	146.41	362.52

Table 4.2: SRTM: mean squared difference values [m^2]

Once written the least squares system the full model was compared with the reduced ones to test the hypothesis that either the gradient or the aspect does not influence the model behaviour.
The results of the model comparison test are presented in Table 4.3, the hypothesis that the slope gradient has no influence on the SRTM is rejected for both the considered value of α since the empirical Fisher F value is greater than the empirical ones; the second hypothesis, about the slope aspect not influencing the model, instead, is rejected for α equal to 5% and accepted for α equal to 1%, so one can deduce that the slope gradient affects more the SRTM DSM than the slope aspect.

	First hypothesis: slope gradient has no influence	**Second hypothesis: slope aspect has no influence**
F_{emp}	23.01	6.42
Degrees of freedom	v_1=3,v_2=9	v_1=3,v_2=9
F_{teo} with $\alpha = 0.01$	6.99	6.99
F_{teo} with $\alpha = 0.05$	3.86	3.86

Table 4.3: SRTM: ANOVA test comparison results

Table 4.2 provide another information, in fact the mean squared difference value corresponds to the variance of the class considered. Assuming differences with zero mean; it is possible then to compute the standard deviation (Table 4.4) as an index of the class variability.

		Aspect			
		NW	SW	SE	NE
Gradient	0 - 3°	3.06	3.73	4.28	3.00
	3° - 10°	6.93	9.59	6.48	7.52
	10° - 20°	9.72	15.68	8.93	11.51
	> 20°	14.38	28.63	12.10	19.04

Table 4.4: SRTM: class standard deviation values [m]

The standard deviation increases as a function of the slope gradient while it does not vary considerably as a function of the aspect; this means that the SRTM follows better the LiDAR DSM behaviour at lower gradient and its height error increase when increasing the slope inclination; analogous results were obtained by [Miliaresis, 2008, Ludwig and Schneider, 2006, Miliaresis and Charalampos, 2005].
The detailed analysis on the SRTM shows that it is anyway more accurate with respect to the nominal accuracy value provided (16 m), in fact the error of the different slope gradient and aspect classes is always under the nominal value apart from the case of gradient greater than 20°.

4.3.2 ASTER analysis

For the ASTER analysis the total amount of classes is 32, in fact:

- the slope gradient was divided in four classes (Figure 4.5) using, as in the previous analysis, the 25%, 50% and 75% gradient map percentiles:
  - 0 - 5°
  - 5° - 12°
  - 12° - 21°
  - greater than 21°
- the slope aspect was divided in eight classes of 45 degrees each (Figure 4.6), for the SRTM DSM this was not done to avoid classes with low absolute frequency:
  - 0 - 45° (E)
  - 45° - 90° (NE)
  - 90° - 135° (N)
  - 135° - 180° (NW)
  - 180° - 225° (W)
  - 225° - 270° (SW)
  - 270° - 315° (S)
  - 315° - 360° (SE)

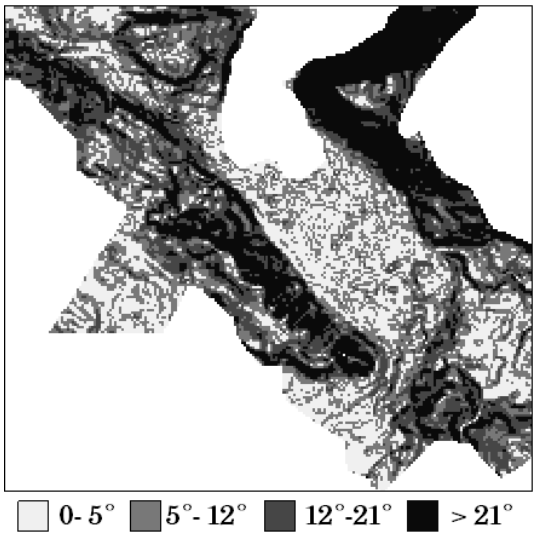

Figure 4.5: ASTER: slope gradient classification

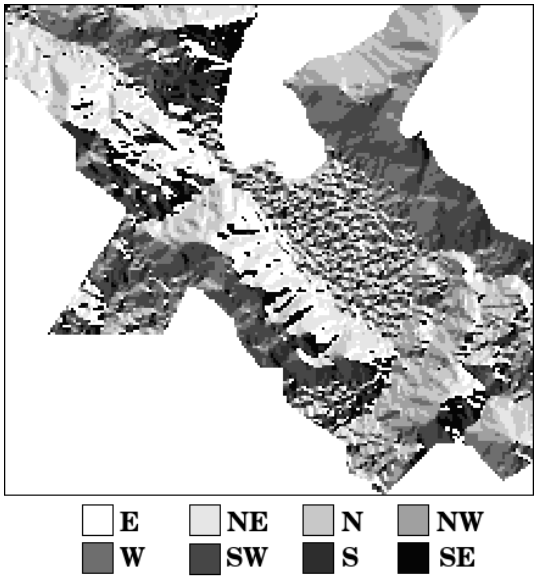

Figure 4.6: ASTER: slope aspect classification

Again a map combining the two classifications was created in the area covered by the LiDAR DSM (Figure 4.7)

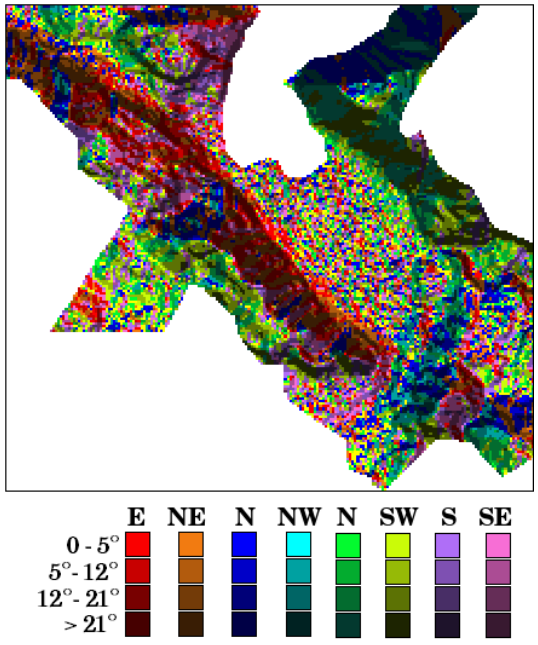

Figure 4.7: ASTER: classification combination map

Table 4.5 contains the absolute frequency of the thirty-two classes; as before these values are used to populate the Q matrix.

		Aspect							
		N	NW	W	SW	S	SE	E	NE
Gradient	0 - 5°	754	732	641	561	657	681	698	674
	5° - 12°	1019	1050	756	659	789	711	705	802
	12° - 21°	833	898	562	597	843	772	634	612
	> 21°	796	1022	246	355	722	1033	1018	591

Table 4.5: ASTER: class size

The observation vector ($\underline{y}_0$) contains the squared mean differences values from the comparison between the LiDAR DSM and the ASTER one (Table 4.6)

		Aspect							
		N	NW	W	SW	S	SE	E	NE
Gradient	0 - 5°	44.22	51.70	51.55	59.14	59.14	63.20	60.06	51.70
	5° - 12°	76.39	82.81	85.75	105.06	111.30	104.45	105.06	89.49
	12° - 21°	129.73	141.85	151.54	176.36	162.82	129.96	153.76	146.89
	> 21°	380.64	402.80	309.76	331.97	257.60	138.30	218.74	288.66

Table 4.6: ASTER: mean squared difference values [m^2]

The model comparison results are presented in Table 4.7.

	First hypothesis: slope gradient has no influence	**Second hypothesis: slope aspect has no influence**
F_{emp}	172.18	4.03
Degrees of freedom	v_1=3,v_2=21	v_1=7,v_2=21
F_{teo} with $\alpha = 0.01$	4.87	3.64
F_{teo} with $\alpha = 0.05$	3.06	2.48

Table 4.7: ASTER: ANOVA test comparison results

From the Fisher F tests it is possible to conclude that the ASTER DSM depends on both the two features, since for both the hypotheses the empirical value is greater than the theoretical one with α equal to 0.01 or 0.05.
We can state that, since the empirical value under the first hypothesis is greater than the other one, the ASTER has a stronger dependence on the gradient than on the aspect.
Concerning the standard deviation (Table 4.8) it is possible to see that the error for the ASTER does increase with the steepness of the slope as for the SRTM.
Comparing the accuracies of Table 4.4 and Table 4.8 it is possible to conclude that the SRTM DSM in the Como area is more accurate than the ASTER one despite the nominal accuracies provided for the two DEMs (16 m for SRTM and 10 m for the ASTER). The ASTER DEM satisfies its nominal error for the first and second slope gradient classes, in all the other cases its error is greater than the nominal one.

		Aspect							
		N	NW	W	SW	S	SE	E	NE
Gradient	0 - 5°	6.65	7.19	7.18	7.69	7.69	7.95	7.75	7.19
	5° - 12°	8.74	9.10	9.26	10.25	10.55	10.22	10.25	9.46
	12° - 21°	11.39	11.91	12.31	13.28	12.76	11.40	12.40	12.12
	> 21°	19.51	20.07	17.60	18.22	16.05	11.76	14.79	16.99

Table 4.8: ASTER: class standard deviation values [m]

Chapter 5

DEM fusion

This chapter describes the final results obtained with this work, which final purpose is the DEM fusion.
Two main kinds of fusion methods are describes, the former based on the concept of weighted average and the latter on the collocation prediction; for each method implementation details and results are proposed.

5.1 Introduction to DEM fusion

The fusion of different data, defined as "a formal framework in which are expressed means and tools for the alliance of data originating from different sources" has the aim to obtain information of greater quality [Wald, 1999].
The merging of different DEMs involves the problem of multi-sourcing information, since the digital elevation models can be obtained by different sources and may have different resolutions and accuracies.
The DEMs fusion strategies are mainly two [Audenino et al., 2001]: the top down fusion and the bottom up one; the former consists in the refinement of an existing reliable DEM using additional multi-source information, in the latter the original data quality is lower, so the data are used to create a brand-new DEM.
At the present there is no established fusion procedure for digital elevation models, however in technical literature some papers focus on this subject: some approaches use the wavelet decomposition to produce a new model [Hahn and Samadzadegan, 1999] or merge various DEMs using different concepts of weight error maps [Roth et al., 2002, Papasaika et al., 2009, Knopfle et al., 1998], other methods are somehow more specific dealing with specific technologies, for example the merging of InSAR DEMs with LiDAR data [Gamba et al., 2003, James, 2003].

The purpose of this work is the testing of different fusion strategies applicable to DEMs obtained from various data sources. In the following two fusion strategies to merge DEMs in the Como area will be proposed.

5.2 Fusion methods

The final purpose of this work consists in the DEMs merging; however it is not easy to define the best fusion approach, so different trial were done.
After each trial the product of the DEM merging was compared to the LiDAR DSM to assess its accuracy in order to evaluate improvements with respect to the original DEMs. Two main merging strategies were taken into account:

- fusion by weighted average;
- fusion by collocation prediction.

The first method is the simplest one, in fact it only needs a set of DSMs weights to be provided, then for each cell the average value is computed. The collocation is more difficult to implement since lots of parameters need to be set. The two DSMs taken in consideration for the merging were the ASTER and the SRTM; their characteristics imposed some limitation to the merged results:

- SRTM at 3 arcseconds is created averaging the values of the SRTM at 1 arcseconds, so its values are a mean value over an area of dimension around 90 m $\times$ 90 m;
- ASTER is from satellite photogrammetry, so its values correspond to point-wise observations (step 30 m).

The consequence is that the merging by weighted average has to produce a DSM covering the SRTM grid (the lower spatial resolution one) since it is not possible to reconstruct point observations from average ones.
The collocation, instead, being a stochastic prediction method, allows the prediction from an average value to a single point observation; consequently the weighted average merged products will be available on the SRTM grid, while the collocation ones will be available on both the two grids.

5.3 Weighted average fusion on the SRTM grid

As said before, the weighted average method requires only the definition of a weight map for each model to be merged. The weight map is defined also as

an error map, since it has to provide information about the DEM accuracy. The error map can be generated in different ways. In this work three different error maps were taken for the ASTER and the SRTM DSMs, they corresponds to the following hypothesis:

1. constant nominal vertical accuracy;
2. constant vertical accuracy from LiDAR DSM comparison (external validation step);
3. variable vertical accuracy from slope gradient and aspect classification.

These three weighted average methods produce DSMs covering the SRTM grid, so their accuracy will be compared to the SRTM one. In the following these three merging attempts and their results are described.

5.3.1 SRTM and ASTER accuracies

The merged maps obtained from the fusion procedure need to be validated in order to verify their improvements with respect to the original data; the validation will be performed comparing them to the LiDAR DSM used to externally validate the SRTM DSM.
The merged map accuracy values have to be compared with the ones of the original DSMs in order to verify potential improvements; concerning the SRTM its accuracy was computed in the external validation step obtaining a standard deviation σ of 13.20 m (see Section 3.3).
As for the assessment of the ASTER accuracy, the ASTER DSM was averaged on the SRTM grid and compared with the LiDAR DSM obtaining a σ of 10.16 m.

5.3.2 Constant nominal vertical accuracy

In this first attempt the error map was created using the nominal vertical accuracy values provided for the two DSMs (16 m for the SRTM and 10 m for the ASTER DSM), so a unique accuracy value was used to weight each digital model.
The height values, as explained before, are merged on the SRTM grid; this means that for each SRTM value about nine ASTER values are available for the fusion, due to the different DSMs spatial resolution.
For this reason two steps were performed to compute the merged value:

1. the ASTER values useful to compute the output value, so the ones that fell into the SRTM cell, were averaged to have a unique value;

2. the SRTM and the ASTER values (indicated in the following as $u(Q_S)$ and $u(Q_A)$) were averaged using the weight map defined.

Each merged value ($u(P)$) was obtained as:

$$u(P) = \frac{\frac{\overline{u}(Q_A)}{\sigma^2_{\overline{A}}} + \frac{u(Q_S)}{\sigma^2_S}}{\frac{1}{\sigma^2_{\overline{A}}} + \frac{1}{\sigma^2_S}} \tag{5.1}$$

in which the $\sigma^2_{\overline{A}}$ and the $\overline{u}(Q_A)$ values are referred to the averaged ones; in particular the $\sigma^2_{\overline{A}}$ is computed from the nominal variances of the N values falling into the SRTM cell as:

$$\sigma^2_{\overline{A}} = \frac{\sigma^2_{nom}}{N}. \tag{5.2}$$

So for the SRTM DSM the weight was equal to the nominal accuracy value (16 m), while for the ASTER it was computed for each output grid node depending on the number of ASTER values falling into the cell. The mosaicked map was then compared with the LiDAR DSM with cell size of 90 m and the mean of the squared difference values was computed; as done in Section 3.3 this value is an index of the accuracy of the resulting map with respect to the one taken as ground truth.
The σ of this first result is equal to 11.52 m, so it is comparable with the ASTER (σ=10.16 m) and more accurate than the SRTM (σ=13.20 m).

5.3.3 Constant vertical accuracy from external validation

This time the error map was created using the accuracies obtained from the external validation step; the procedure to fuse the two DSMs is the same as in the attempt described in the previous section (see Formula 5.1). A σ value of 13.20 m was considered for the SRTM where the value of 12.32 m for the ASTER DSM; the accuracy of the merged map is equal to 11.48 m, that is an improvement with respect to the original data and to the fusion using the nominal accuracies. Naturally, in this way the weighting procedure is not completely independent from the data set there used for the accuracy assessment.

5.3.4 Variable vertical accuracy

The last weighted average merging attempt was performed using error maps in which the accuracy was a function of the terrain morphology.
In order to classify the terrain the slope gradient and aspect maps used in the ANOVA analysis were taken into account (see Section 4.3) and for each class an accuracy value was assigned; in this way the weight is more reliable since the local behaviour of the model is considered.
The computation of the ASTER averaged value is slightly different from the one used in the previous merging procedure since the variance varies cell by cell; the ASTER value is obtained as a weighted average of the N ones falling into the SRTM cell:

$$\overline{u}\left(Q_A\right) = \frac{\sum_{i=1}^{N} \frac{1}{\sigma_i^2} u\left(Q_{A_i}\right)}{\sum_{i=1}^{N} \frac{1}{\sigma_i^2}} \tag{5.3}$$

The variance value corresponding to the $\overline{u}\left(Q_A\right)$ one is obtained as propagation from the N ASTER variances.

$$\sigma_{\overline{A}}^2 = \frac{1}{\sum_{i=1}^{N} \frac{1}{\sigma_i^2}} \tag{5.4}$$

Once obtained the averaged ASTER value and its variance, the merged value is computed as in the previous cases (see Formula 5.1). The comparison of the mosaicked product with respect to the LiDAR DSM gave a final accuracy of 10.75 m, so also in this attempt there is a quality increase with respect to the original SRTM and ASTER DSMs.

5.3.5 Weighted average fusion: summary

The three weighted average merging trials prove the increasing of accuracy of the fusion results; Table 5.1 contains a summary of the elaboration results with respect to the original models on the SRTM grid.
As Table 5.1 shows, the accuracy increases as the merging method increases the amount of information used: the simpler method uses general information provided with the data, while in the latter method terrain morphology details are introduced.

Model (on the SRTM grid)	Accuracy (m)
SRTM	13.20
ASTER	10.16
Fusion with constant nominal vertical accuracy	11.52
Fusion with constant vertical accuracy from external validation	11.48
Fusion with variable vertical accuracy from gradient and aspect classes	10.75

Table 5.1: Weighted average merging: summary

The method that provides the best results is the one with variable vertical accuracies as a function of the terrain morphology; this result was expected since the two digital surface models proved to be dependent on the terrain slope gradient and aspect (for details see Section 4.3).

5.4 Fusion on the ASTER grid using collocation

As said in Section 5.2, the second fusion strategy involves the stochastic prediction method of collocation. The stochastic approach is used since it allows the prediction of a point value from an average one, so the merged outputs can be DSMs corresponding to the ASTER grid and not the SRTM one.
This method however is more complex than the one based on the weighted average values, so in the following some notion about the collocation method will be provided in addition to the implementation description.

5.4.1 Collocation method outline

Collocation is a stochastic method to model and predict a signal using its stochastic properties (e.g covariance function ...); it assumes that the signal has a zero mean, otherwise the use of the kriging prediction method is more suitable [Sansó, 1986, Koch, 1997].
Let us consider the 1D case for the sake of simplicity; the generalization to the 2D case for the DTM analysis is quite straightforward; the assumption

is that the observations (y_0) are sampled from a random process plus noise (Formula 5.5) and have certain stochastic features (signal and noise mean values, signal and noise covariance functions and correlation, as in Formula 5.6).

$$y_0(t_i) = s(t_i) + \nu(t_i) \tag{5.5}$$

$$\begin{cases} E[s(t_i)] = E[\nu(t_i)] = 0 & \forall t_i \\ E[s(t_i)\, s(t_j)] = C_s(t_i, t_j) & \forall t_i, t_j \\ E[\nu(t_i)\, \nu(t_j)] = C_\nu(t_i, t_j) = \sigma_v^2 \delta_{ij} & \text{with:} \delta_{ij} = \begin{cases} 1 & i = j \\ 0 & i \neq j \end{cases} \forall t_i, t_j \\ E[s(t_i)\, \nu(t_j)] = 0 & \forall t_i, t_j \end{cases} \tag{5.6}$$

The signal value in $t_\emptyset$ is estimated using a linear combination of the available observations (Formula 5.7) and the combination weights $\underline{\lambda}$ are determined thanks to the Wiener-Kolmogorov principle (Formula 5.8) that is to minimize the square estimation error.

$$\widehat{s}(t_\emptyset) = \sum_i \lambda_i y_{0i} = \underline{\lambda}^T \underline{y}_0 \tag{5.7}$$

$$E\left\{[s(t_\emptyset) - \widehat{s}(t_\emptyset)]^2\right\} = \min_{\underline{\lambda}} \tag{5.8}$$

The result of the minimization is:

$$\widehat{s}(t_\emptyset) = \underline{C}_{ss_\emptyset}^T \left(C_{ss} + C_{\nu\nu}\right)^{-1} \underline{y}_0 \tag{5.9}$$

where:

$$\underline{C}_{ss_\emptyset} = \begin{bmatrix} C_s(t_1, t_\emptyset) \\ C_s(t_2, t_\emptyset) \\ \vdots \\ C_s(t_N, t_\emptyset) \end{bmatrix} \tag{5.10}$$

$$\underline{C}_{ss} = \begin{vmatrix} C_s(t_1, t_1) & C_s(t_1, t_2) & \dots & C_s(t_1, t_N) \\ C_s(t_2, t_1) & C_s(t_2, t_2) & \dots & C_s(t_2, t_N) \\ \vdots & \vdots & \ddots & \vdots \\ C_s(t_N, t_1) & C_s(t_N, t_2) & \dots & C_s(t_N, t_N) \end{vmatrix} \tag{5.11}$$

$$\underline{C}_{\nu\nu} = \begin{vmatrix} \sigma_\nu^2 & 0 & \dots & 0 \\ 0 & \sigma_\nu^2 & \ddots & \vdots \\ \vdots & \ddots & \ddots & 0 \\ 0 & \dots & \dots & \sigma_\nu^2 \end{vmatrix} = \sigma_\nu^2 I \tag{5.12}$$

with N the number of available observations. Of course, it is not possible to compute the estimation error (Formula 5.13), i.e. the difference between

the true and the estimated signal, since the true signal is unknown; the only information computable about the error is the error variance (Formula 5.14).

$$e\left(t_{\emptyset}\right) = s\left(t_{\emptyset}\right) - \widehat{s}\left(t_{\emptyset}\right) \tag{5.13}$$

$$E^2\left(t_{\emptyset}\right) = \sigma^2\left\{e\left(t_{\emptyset}\right)\right\} = C_s\left(t_{\emptyset}, t_{\emptyset}\right) - \underline{C}^T_{ss_{\emptyset}}\left(C_{ss} + C_{\nu\nu}\right)^{-1}\underline{C}_{ss_{\emptyset}} \tag{5.14}$$

In order to apply the collocation estimation process it is necessary to have the covariance matrices values (Formulae 5.10, 5.11, 5.12); to populate these matrices the covariance function of the process need to be estimated.
The procedure to estimate this function from the empirical covariance values consists of three steps:

- empirical covariance function estimation from the data, assuming the nD random field homogeneous and isotropic (Figure 5.1)

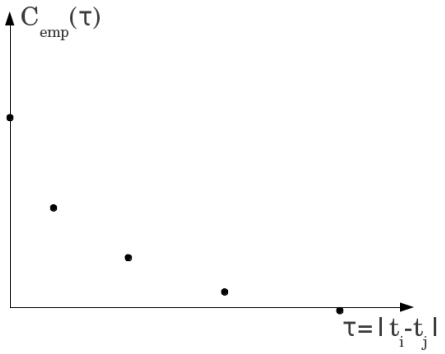

Figure 5.1: Empirical covariance function estimation

- covariance function interpolation using a positive definite model (Figure 5.2);

$$C_s\left(\tau\right) = C_s\left(\left|t - t'\right|\right) \quad \forall t, t' \tag{5.15}$$

- noise variance estimation from the empirical covariance value and the interpolated one at τ=0 (Formula 5.16). If $\widehat{C}_s\left(0\right) > C_{emp}\left(0\right)$ for numerical reason, the variance of the noise have to be forced equal to zero or set up to an a-priori value.

$$\widehat{\sigma}^2_{\nu} = C_{emp}\left(0\right) - \widehat{C}_s\left(0\right) \tag{5.16}$$

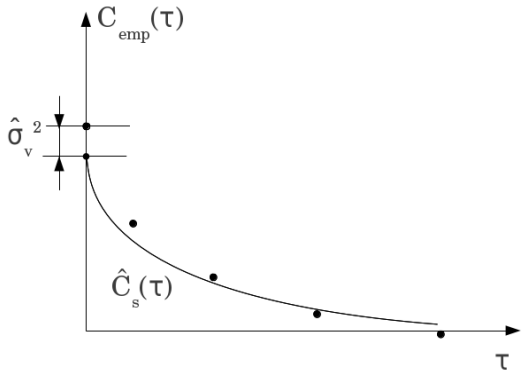

Figure 5.2: Covariance function interpolation

Another way to obtain the covariance function, that is the one applied in this work, is based on the empirical variogram estimation [Wackernagel, 1998]. The variogram is a function (Formula 5.17 where $s(t_i, t_j) = \mu + u(t_i, t_j)$) defined in such a way that it does not depend on the mean value (μ).

$$\begin{aligned} \gamma_s(t_i, t_j) &= \frac{1}{2} E\left[(s(t_i) - s(t_j))^2\right] \\ &= \frac{1}{2} E\left[(u(t_i) - u(t_j))^2\right] = \gamma_u(t_i, t_j) \end{aligned} \tag{5.17}$$

Once computed the empirical variogram and estimated the variogram function (Figure 5.3), the covariance function can be extracted thanks to a relation between covariance and variogram (Formula 5.18).

$$\gamma_s(\tau) = C_s(0) - C_s(\tau) \tag{5.18}$$

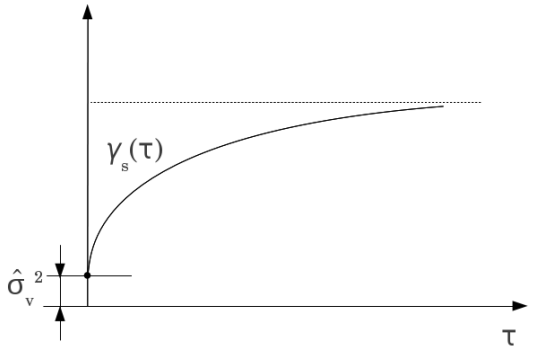

Figure 5.3: Variogram function estimation

Finally it is necessary to point out that there exist variogram models which do not have a corresponding covariance models.

5.4.2 Collocation method implementation

The fusions obtained with the collocation method were done in different sub areas and not for the whole ASTER grid. This was necessary since this merging method is very time consuming; the testing areas were chosen as representative of different morphologies such as flat terrain, hills and mountainous areas to assess the fusion method performances; Figure 5.4 shows the position of the chosen regions with respect to the ASTER DSM.

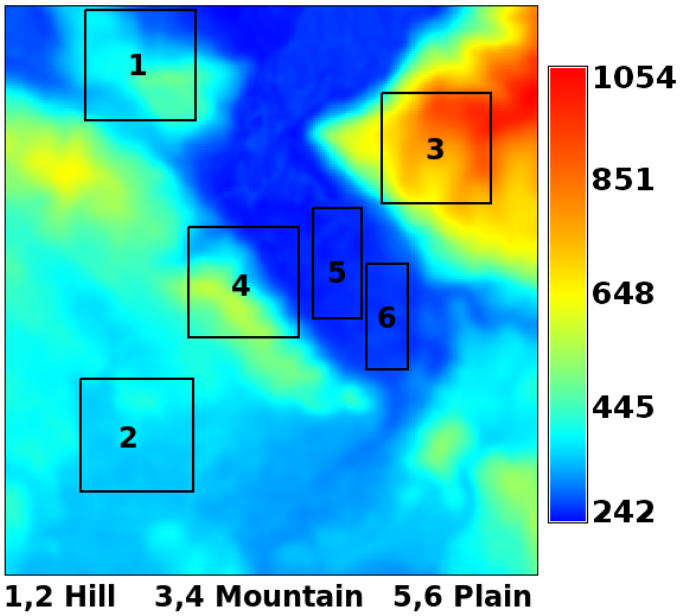

Figure 5.4: Fusion with collocation: testing area

The method implementation is the same for each area, so for each testing region only the specific results are reported.
The prediction on the ASTER grid is done, after removing the mean height value from the observations, using the collocation method; its implementation, however, is different from the general one described in Section 5.4.1 because the observations belong to two different data sets: the ASTER sparse point observations and the SRTM ones. In addition, the two observation sets represents different entities, as mentioned in Section 5.2. In fact the ASTER

data correspond to point features, while the SRTM ones are average values of the height field over the cell areas.
For these reasons, in the following, the collocation is outlined referring to the specific prediction problem considered.
The main purpose is the height prediction ($\widehat{u}$) in a generic point P using the ASTER ($\underline{y}_{0A}$) and SRTM ($\underline{y}_{0S}$) observations; the observations are combined using two sets of weights λ and μ (Formula 5.19):

$$\widehat{u}(P) = \begin{bmatrix} \underline{\lambda}^T & \underline{\mu}^T \end{bmatrix} \begin{bmatrix} \underline{y}_{0A} \\ \underline{y}_{0S} \end{bmatrix}. \tag{5.19}$$

The ASTER and the SRTM observations depend on both the signal and the noise (Formula 5.20); in the SRTM case, however, this relation must be expressed as an average value defined by a double integral over an area (R) around the observation point Q_S (see Figure 5.5 for clarification on the symbols used).

$$\begin{aligned} \underline{y}_{0A} &= \underline{u}(Q_A) + \underline{\nu}_A(Q_A) \\ \underline{y}_{0S} &= \frac{1}{R} \int\int_R u(Q)\, dR + \underline{\nu}_S(Q_S) \end{aligned} \tag{5.20}$$

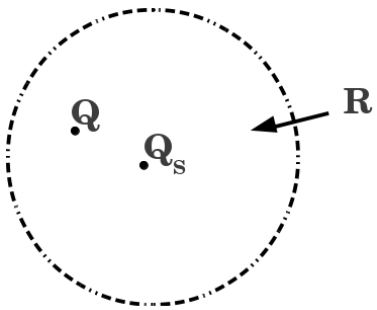

Figure 5.5: SRTM: how to define the signal in Q_S

The prediction is possible once found the $\underline{\lambda}$ and $\underline{\mu}$ weight values; among the possible solutions it is chosen the one that minimizes the average square difference between the signal and its prediction (Formula 5.21).

$$E\left\{[u(P) - \widehat{u}(P)]^2\right\} = \min_{\underline{\lambda},\underline{\mu}} \tag{5.21}$$

Defining as Φ the function to be minimized, it can be expressed as described as follows:

$$\Phi = E\left\{[u(P) - \widehat{u}(P)]^2\right\} = E\left\{\left[u(P) - \underline{\lambda}^T \underline{y}_{0A} - \underline{\mu}^T \underline{y}_{0S}\right]^2\right\} \tag{5.22}$$

it is possible then to substitute the terms $\underline{y}_{0A}$ and $\underline{y}_{0S}$ with their definitions (see Formula 5.20).

$$\begin{aligned}\Phi =& E\left\{\left[u\left(P\right)-\lambda^{T}\left(\underline{u}\left(Q_{A}\right)+\underline{\nu}_{A}\left(Q_{A}\right)\right)+\right.\right. \\ &\left.\left.-\underline{\mu}^{T}\left(\frac{1}{A}\int\int u\left(Q_{i}\right)dA_{i}+\underline{\nu}_{S}\left(Q_{S}\right)\right)\right]^{2}\right\}\end{aligned} \tag{5.23}$$

To simplify the solution the term $\frac{1}{R}\int\int_{R}u\left(Q\right)dR$ will be indicated hereafter as $\overline{u}\left(Q_{S}\right)$.

$$\begin{aligned}\Phi &= E\left\{\left[u\left(P\right)-\lambda^{T}\underline{u}\left(Q_{A}\right)-\underline{\lambda}^{T}\underline{\nu}_{A}\left(Q_{A}\right)-\underline{\mu}^{T}\overline{u}\left(Q_{S}\right)-\underline{\mu}^{T}\underline{\nu}_{S}\left(Q_{S}\right)\right]^{2}\right\}= \\ &= E\left\{u^{2}\left(P\right)+\underline{\lambda}^{T}\underline{u}\left(Q_{A}\right)\underline{u}^{T}\left(Q_{A}\right)\underline{\lambda}+\underline{\lambda}^{T}\underline{\nu}_{A}\left(Q_{A}\right)\underline{\nu}_{A}^{T}\left(Q_{A}\right)\underline{\lambda}+\right. \\ &+\underline{\mu}^{T}\overline{u}\left(Q_{S}\right)\overline{u}^{T}\left(Q_{S}\right)\underline{\mu}+\underline{\mu}^{T}\underline{\nu}_{S}\left(Q_{S}\right)\underline{\nu}^{T}\left(Q_{S}\right)\underline{\mu}+ \\ &-2u\left(P\right)\underline{\lambda}^{T}\underline{u}\left(Q_{A}\right)-2u\left(P\right)\underline{\lambda}^{T}\underline{\nu}_{A}-2u\left(P\right)\underline{\mu}^{T}\overline{u}\left(Q_{S}\right)+ \\ &-2u\left(P\right)\underline{\mu}^{T}\underline{\nu}_{S}\left(Q_{S}\right)+2\underline{\lambda}^{T}\underline{u}\left(Q_{A}\right)\underline{\nu}_{A}^{T}\left(Q_{A}\right)\underline{\lambda}+ \\ &+2\underline{\lambda}^{T}\underline{u}\left(Q_{A}\right)\overline{u}^{T}\left(Q_{S}\right)\underline{\mu}+2\underline{\lambda}^{T}\underline{u}\left(Q_{A}\right)\underline{\nu}_{S}^{T}\left(Q_{S}\right)\underline{\mu}+ \\ &\left.+2\underline{\lambda}^{T}\underline{\nu}_{A}\overline{u}\left(Q_{S}\right)\underline{\mu}+2\underline{\lambda}^{T}\underline{\nu}_{A}\underline{\nu}_{S}^{T}\left(Q_{S}\right)\underline{\mu}+2\underline{\mu}^{T}\overline{u}\left(Q_{S}\right)\underline{\nu}_{S}^{T}\left(Q_{S}\right)\underline{\mu}\right\}\end{aligned} \tag{5.24}$$

Then the expectation is:

$$\begin{aligned}\Phi &= C_{u}\left(0\right)+\underline{\lambda}^{T}C_{AA}\underline{\lambda}+\underline{\lambda}^{T}C_{\nu_{A}\nu_{A}}\underline{\lambda}+\underline{\mu}^{T}C_{SS}\underline{\mu}+\underline{\mu}^{T}C_{\nu_{S}\nu_{S}}\underline{\mu}+ \\ &-2\underline{\lambda}^{T}C_{A}\left(P\right)-2\underline{\mu}^{T}C_{S}\left(P\right)+2\underline{\lambda}^{T}C_{AS}\underline{\mu}=\min_{\underline{\lambda},\underline{\mu}}\end{aligned} \tag{5.25}$$

note that, when computing the expectation expression, the terms in which the signal is multiplied with the noise give zero as expected value, this happens because signal and noise are supposed to be uncorrelated, the same for the multiplication of two noises.
The minimization of the function Φ is then done imposing its differential over $\underline{\lambda}$ and over $\underline{\mu}$ equal to zero (Formula 5.26).

$$\begin{cases}\dfrac{d\Phi}{d\lambda}=\delta\underline{\lambda}^{T}C_{AA}\underline{\lambda}+\delta\underline{\lambda}^{T}C_{\nu_{A}\nu_{A}}\delta\underline{\lambda}-\delta\underline{\lambda}^{T}C_{AS}\underline{\mu}-\delta\underline{\lambda}^{T}C_{A}\left(P\right)=0 \\ \dfrac{d\Phi}{d\mu}=\delta\underline{\mu}^{T}C_{SS}\underline{\mu}+\delta\underline{\mu}^{T}C_{\nu_{S}\nu_{S}}\underline{\mu}-\delta\underline{\mu}C_{S}\left(P\right)+\underline{\lambda}^{T}C_{AS}\delta\underline{\mu}=0\end{cases} \tag{5.26}$$

The equations in Formula 5.26 can be rearranged in matrices; then the solution, i.e. the $\underline{\lambda}$ and $\underline{\mu}$ values, can be computed (Formula 5.27) as:

$$\begin{bmatrix}C_{AA}+C_{\nu_{A}\nu_{A}} & C_{AS} \\ C_{AS}^{T} & C_{SS}+C_{\nu_{S}\nu_{S}}\end{bmatrix}\begin{bmatrix}\underline{\lambda} \\ \underline{\mu}\end{bmatrix}=\begin{bmatrix}\underline{C}_{A}\left(P\right) \\ \underline{C}_{S}\left(P\right)\end{bmatrix} \tag{5.27}$$

Once estimated the $\underline{\lambda}$ and $\underline{\mu}$ values, it is possible to predict the signal in the point of prediction using the relation in Formula 5.19. So far concerning the theoretical aspects of the problem; on the other hand, from the practical point of view, other information are needed to populate the matrices defined above, like, for example, the empirical covariance model function.
For each test area a model covariance function is obtained from a variogram function fitted on the ASTER sparse points falling in the area by the VESPER[1] software (Variogram Estimation and Spatial Prediction plus ERror) [Whelan et al., 2002]. This shareware software was chosen because it is able to manage large datasets and, because of its user-friendly interface, it is easy to use.
The software, once given a dataset of points, computes the empirical variogram function and fits it with one suitable model available; it provides also the coefficients needed to define the analytical model.
Using the relation defined in Formula 5.18 it is possible to get the corresponding covariance model from the variogram one.
In the following sections the way each matrix was constructed is described.

Observation vector y_0: the observation vector y_0 is constructed using the ASTER ($\underline{y}_{0A}$) and SRTM ($\underline{y}_{0S}$) sparse points, obtained after the coordinate conversion step, that falls into the testing region under analysis.

$$y_0 = \begin{bmatrix} \underline{y}_{0A} \\ \underline{y}_{0S} \end{bmatrix} = \begin{bmatrix} y_{0A_1} \\ y_{0A_2} \\ \vdots \\ y_{0A_n} \\ y_{0S_1} \\ y_{0S_2} \\ \vdots \\ y_{0S_m} \end{bmatrix} \tag{5.28}$$

Signal covariance matrix C_{ss}: the full signal covariance matrix is composed by the covariance matrix between the signal with itself (C_{AA} and C_{SS}) and between the two signals available (C_{AS} between the ASTER and SRTM points):

$$C_{ss} = \begin{bmatrix} C_{AA} & C_{AS} \\ C_{AS}^T & C_{SS} \end{bmatrix}. \tag{5.29}$$

The covariance matrix between the ASTER data with themselves is created computing at first all the distances between the dataset points and then the

[1] http://www.usyd.edu.au/agriculture/acpa/software/vesper.shtml

covariance value corresponding to each distance using the empirical covariance model defined for the region.
The field is assumed to be homogeneous and isotropic, so the signal covariance is just a function of the distance but not of the direction.
The set up of the covariance matrix between SRTM and ASTER and the one between the SRTM with itself is more difficult due to the fact that the SRTM signal is defined as an integral over a surface (Formula 5.20).
The analytical solution of the double integral is generally unknown, so the computation of the C_{SS} and the C_{AS} values is done by numerical approximations. Concerning the covariances between the ASTER and the SRTM points, each SRTM value is represented as function of the twenty-four values representative of the twenty-four circular sectors around (Figure 5.6). Unfortunately at the present no influence evaluation of the numbers of sectors chosen was done, future works may include this analysis and the tests with different sector divisions.

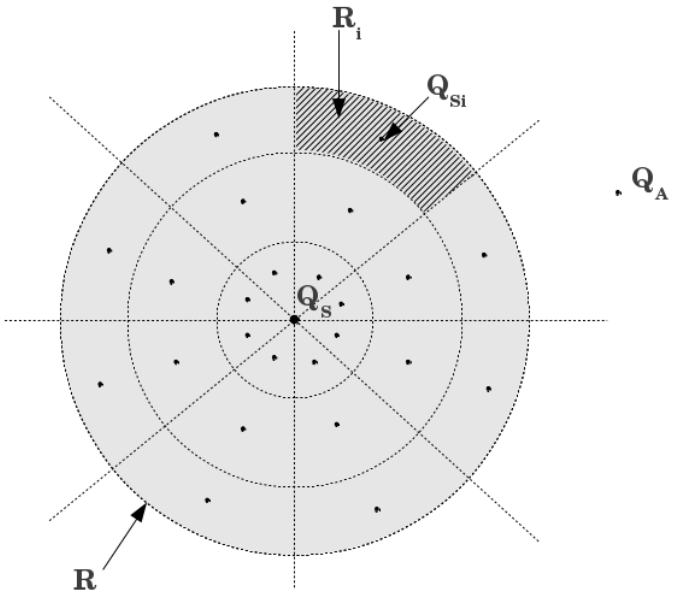

Figure 5.6: Position of the twenty four circular sectors around the SRTM point Q_S

For each ASTER point (Q_A) the distances with respect to the twenty-four central point (Q_{S_i}) of the sectors around the SRTM point (Q_S) are computed and the corresponding covariance value (σ_{AS_i}), computed based on an empiri-

cal covariance model, are consequently obtained.
Each covariance value has a weight that depends on the area of the sector (R_i in Figure 5.6) over the total area around the SRTM point (the whole gray area R in Figure 5.6); the result of the weighted sum of the twenty-four covariance values is then associated to the couple of SRTM and ASTER points taken into account (see Formula 5.30).

$$\sigma_{AS} = \frac{1}{R} \sum_{i=1}^{24} \sigma_{AS_i} R_i \tag{5.30}$$

The covariance values of the SRTM points with themselves are the results of the following integral where Q_{S_i} and Q_{S_k} are the points near to the two SRTM values for which the covariance value has to be computed:

$$\begin{aligned}
&E\left\{\frac{1}{R}\int\int_{Q_{S_i}} u\left(Q_i\right) dR_i \cdot \frac{1}{R}\int\int_{Q_{S_k}} u\left(Q_{S_k}\right) dR_k\right\} = \\
&E\left\{\frac{1}{R^2}\int\int_{Q_{S_i}}\int\int_{Q_{S_k}} u\left(Q_{S_i}\right) dR_i u\left(Q_{S_k}\right) dR_k\right\} = \\
&\frac{1}{R^2}\int\int_{Q_{S_i}}\int\int_{Q_{S_k}} E\left\{u\left(Q_{S_i}\right) u\left(Q_{S_k}\right)\right\} dR_i dR_k = \\
&\frac{1}{R^2}\int\int_{Q_{S_i}}\int\int_{Q_{S_k}} C\left(Q_{S_i}, Q_{S_k}\right) dR_i dR_k
\end{aligned} \tag{5.31}$$

The analytical solution of this integral is unknown, so a numerical approximation is needed. Considering two SRTM points (Q_{S_1} and Q_{S_2}) (Figure 5.7), between whom the covariance value has to be computed, we have two numerical approximations done using twenty-four sectors for each SRTM point. For each Q_{S_i} point around Q_{S_1} the distances and the covariance function values to the points around Q_{S_2} are computed; then these values are summed using weights depending on the ratio between the sector area R_k and the total area R_2 around Q_{S_2}, the result is the covariance value between Q_{S_2} and the Q_{S_i} point around Q_{S_1}:

$$\sigma_{S_i S_2} = \frac{1}{R_2} \sum_{k=1}^{24} \sigma_{S_i S_k} R_k \tag{5.32}$$

The covariance value between Q_{S_1} and Q_{S_2} is obtained by performing a weighted sum of the twenty-four covariance values obtained between Q_{S_2} and the twenty-four Q_{S_i} points; the weights are, as before, the ratios between the sector area R_i and the total area R_1 around the SRTM point Q_{S_1} (Formula 5.33).

$$\sigma_{S_1 S_2} = \frac{1}{R_1} \sum_{i=1}^{24} \sigma_{S_i S_2} R_i \tag{5.33}$$

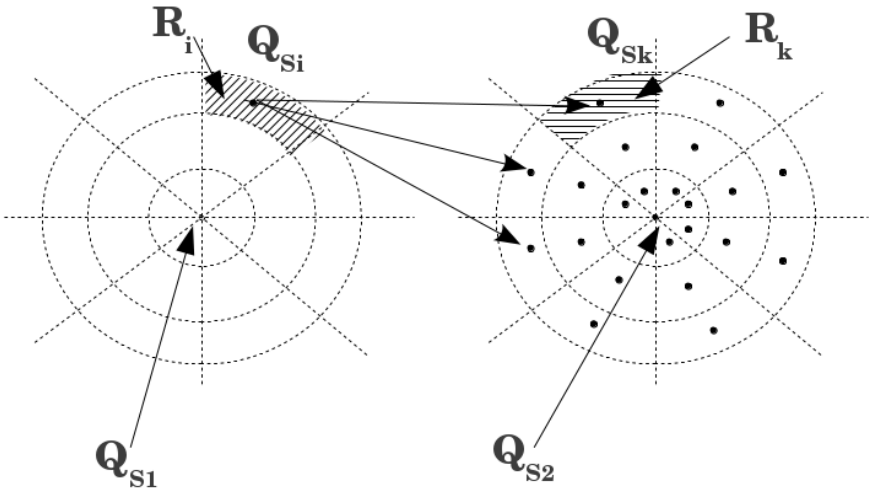

Figure 5.7: Numerical approximation of the SRTM value using the twenty-four values around

Noise covariance matrix $\boldsymbol{C_{\nu\nu}}$: the full noise covariance matrix is composed by the covariance matrices of the ASTER noise with itself ($C_{\nu_A\nu_A}$) and of the SRTM noise with itself ($C_{\nu_S\nu_S}$); the noise of the ASTER is supposed uncorrelated with the SRTM one:

$$C_{ss} = \begin{bmatrix} C_{\nu_A\nu_A} & 0 \\ 0 & C_{\nu_S\nu_S} \end{bmatrix} \tag{5.34}$$

The used noise variances are those obtained from the empirical covariance model of each test area or, in some cases, the accuracy values from the comparison with the LiDAR DSM.

Covariance matrix between point of prediction and observations $\boldsymbol{C_{P0}}$: the point of prediction (P) belongs to the ASTER grid, since this fusion method aims at improving the ASTER DSM, while the observation points are the sparse ones.
The full cross-covariance matrix ($\underline{C}_{P0}$) is composed by the covariance matrix between the prediction point and the ASTER sparse ones ($\underline{C}_A(P)$) and the covariance matrix between the same prediction point and SRTM ones ($\underline{C}_S(P)$).

$$\underline{C}_{P0} = \begin{bmatrix} \underline{C}_A(P) \\ \underline{C}_S(P) \end{bmatrix} \tag{5.35}$$

The matrix $\underline{C}_A(P)$ contains the covariance values between the ASTER observation points and the prediction point, that are, as before, function of the distance between the points and computed using the empirical covariance model.
The covariances between the SRTM points and the prediction point, instead, is calculated with the same procedure used to obtain the values in the matrix C_{AS}.

5.4.3 Test region 1: hill

The first region considered is an hill (identified as number one in Figure 5.4) and covers an area of 1350 m × 1350 m (Figure 5.8), whose boundary are defined by the following coordinates (in WGS84-UTM32N): north 5075930 m, south 5074580 m, east 504810 m and west 503460 m.

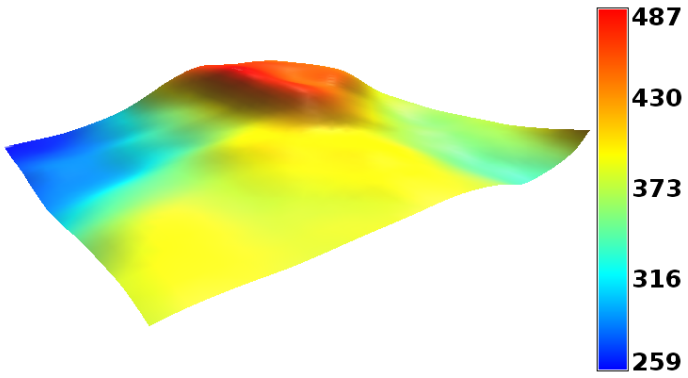

Figure 5.8: Region 1: hill

The ASTER sparse points falling in this area were extracted and used in VESPER to compute the empirical variogram and covariance model; Figure 5.9 shows the empirical variogram, the empirical variogram model obtained fitting the points with a suitable model and the empirical covariance model obtained from the variogram one.
The empirical variogram model (Figure 5.9) fits well the data until a certain distance, this happens because, from the perspective of a local analysis, the model was created using the points within 1200 m, distance at which the empirical variogram behaviour tends to change. This choice was done also because when the distance increase, the number of points useful for the variogram computation decreases, consequently the reliability of the empirical

variogram decreases as well.

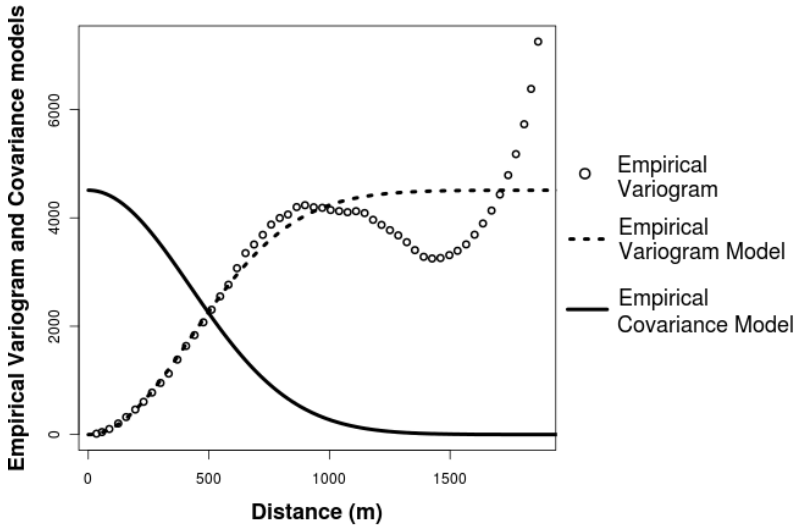

Figure 5.9: Region 1: empirical variogram, empirical variogram model and empirical covariance model (ASTER data)

VESPER gives the possibility to select the best fitting empirical variogram model among the following models: spherical, exponential, gaussian, linear with sell, stable, generalized Cauchy, double spherical and double exponential [Australian Centre for Precision Agriculture, 2006]. The model, for each test area, was chosen because its RMSE is the lower one, the RMSE value is computed as the mean of the squared difference between the interpolated model and the fitted observations.
This criterion was applied for all the test regions, so the model used in the fitting step was always the optimum one considering the RMSE value.
In this test area the optimum model was a gaussian one (RMSE of 160.5 m), corresponding to the empirical covariance model defined in Formula 5.36, where A and α are coefficients estimated by the VESPER software:

$$\begin{cases} y = Ae^{-\alpha d^2} \\ A = 4510.5 \\ \alpha = \dfrac{1}{597.7^2} \end{cases} \tag{5.36}$$

It is interesting to point out that the choice of a slightly different covariance function does not influence significantly the prediction, in particular, using an approximate covariance function, the estimation error is not significant,

as stated in [Sansó et al., 1999]. The empirical covariance model was used to compute the covariance values needed to fill up the collocation matrices; in particular, concerning the noise matrix, the empirical covariance model obtained by VESPER is characterized by a noise variance of 3.349 m^2, used for both the ASTER and the SRTM model.
The prediction on the ASTER grid with the collocation method was done using as input the SRTM and the ASTER sparse point datasets; not all the points available were used, in fact to predict the height value in a point only the points falling into a window, which dimension depends on the distance at which the signal information are no more significant, are considered. Practically, this distance correspond to the one at which the empirical covariance function is close to zero. In this way, only the points that can provide useful information in estimating the signal at the considered prediction point are used, reducing the computational burden.
In this test area the correlation length corresponds to 1200 m, so windows with dimension of 2400 m $\times$ 2400 m around the prediction point were taken into account.
The collocation was applied again to predict the ASTER grid using only the ASTER sparse point dataset; the result of this procedure was compared to the merged DSM to assess whether the use of both datasets provides improvements or not.
The results of the prediction step were then compared with the LiDAR DSM to evaluate their accuracies; Table 5.2 shows the LiDAR comparison results for the two collocation prediction products; it contains also the accuracies of the gridded ASTER DSM and the gridded SRTM one (evaluated on the 90 m cell grid).

Model (on the ASTER grid)	**Accuracy (m)**
SRTM (accuracy evaluated on the SRTM grid)	10.48
ASTER	10.82
ASTER prediction using collocation	12.54
Fusion by collocation prediction	12.44

Table 5.2: Hill: fusion results

The results in Table 5.2 show that the fusion procedure, in this test region, did not bring any improvement with respect to the original ASTER model.

Both the prediction of the ASTER grid alone and the fusion result have accuracies (12.54 m and 12.44 m) lower than the one of the original ASTER DSM (10.82 m).

5.4.4 Test region 2: hill

The morphology of the second test region is again a hill (identified as number two in Figure 5.4) and covers an area of 1380 m × 1380 m (Figure 5.10) whose boundary are defined by the following coordinates (in WGS84-UTM32N): north 5071400 m, south 5070020 m, east 504780 m and west 503400 m.

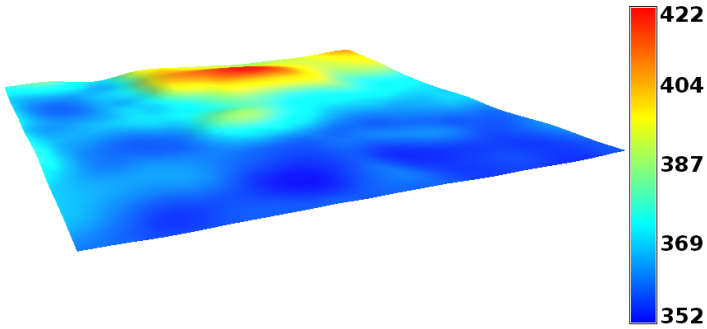

Figure 5.10: Region 2: hill

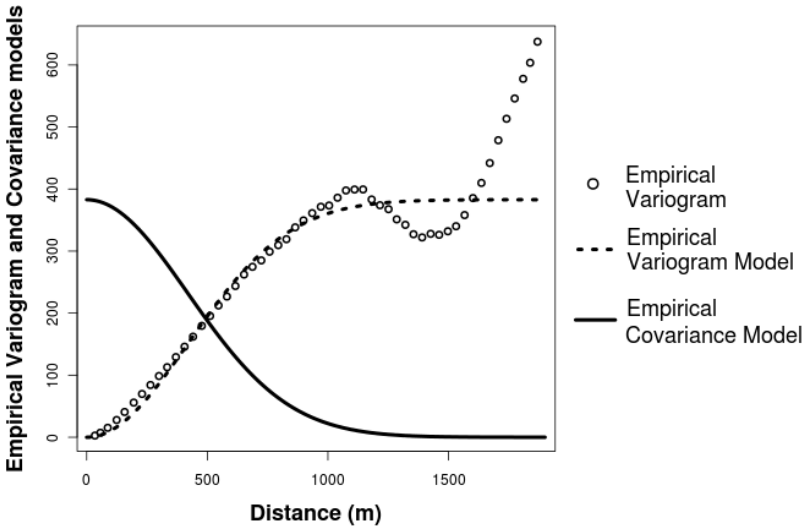

Figure 5.11: Region 2: empirical variogram, empirical variogram model and empirical covariance model (ASTER data)

Again, from the ASTER sparse points the variogram model was created and fitted using the VESPER software (Figure 5.11), and from the variogram the empirical covariance function was derived.
The best empirical covariance model chosen, a gaussian one (RMSE of 12.37 m), is defined in Formula 5.37, where A and α are coefficients estimated by the VESPER software:

$$\begin{cases} y = Ae^{-\alpha d^2} \\ A = 382.9 \\ \alpha = \dfrac{1}{592.6^2} \end{cases} \tag{5.37}$$

The comparison of the final product was also performed using as ground truth the photogrammetric DSM, since in this area the LiDAR one was not available. The accuracy of the photogrammetric DSM (2 m), however, guarantees reliable external validation results.
In this area the correlation length used to create the empirical variogram model and the prediction window is 1200 m, because after this distance the empirical variogram model does not fit any more the data, so for the prediction only the points falling into the 2400 m $\times$ 2400 m around the prediction point are used. The noise variance value from the covariance model is equal to 3.89 m^2, this value was used to identify the variance of both the ASTER and the SRTM noise.

Model (on the ASTER grid)	**Accuracy (m)**
SRTM (accuracy evaluated on the SRTM grid)	6.21
ASTER	9.87
ASTER prediction using collocation	10.42
Fusion by collocation prediction	10.40

Table 5.3: Hill: fusion results

In Table 5.3 the comparison results between the collocation predicted DSMs (the ASTER and the merged one) and the photogrammetric DSM are presented. The results show that, also in this hill region, the SRTM dataset did not provide information useful to improve the ASTER DSM accuracy. It is possible to conclude that in the first two regions, characterized by hill morphology, the fusion on the ASTER DSM grid is not recommended since the original ASTER DSM has a better accuracy than the SRTM one, so the

SRTM DSM does not provide any improvement to the merged DSM.

5.4.5 Test region 3: mountain

The third considered region is a mountainous one, displayed in Figure 5.12 and identified as number three in Figure 5.4, and covering an area of 1350 m × 1350 m which boundaries are defined by the following coordinates (in WGS84-UTM32N): north 5074910 m, south 5073560 m, east 508440 m and west 507090 m.

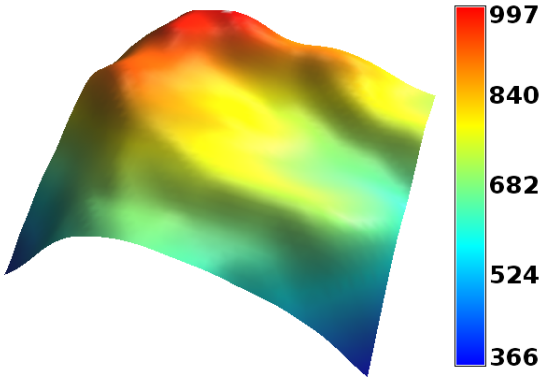

Figure 5.12: Region 3: mountain

As in the previous elaborations, the ASTER sparse points falling in this region were extracted and the empirical covariance model was obtained from the empirical variogram one (Figure 5.13). The empirical variogram was fitted, following the criterion specified in Section 5.4.3, with a gaussian model (RMSE of 902.5 m), the corresponding empirical covariance model is defined in Formula 5.38:

$$\begin{cases} y = Ae^{-\alpha d^2} \\ A = 13537 \\ \alpha = \dfrac{1}{338.9^2} \end{cases} \tag{5.38}$$

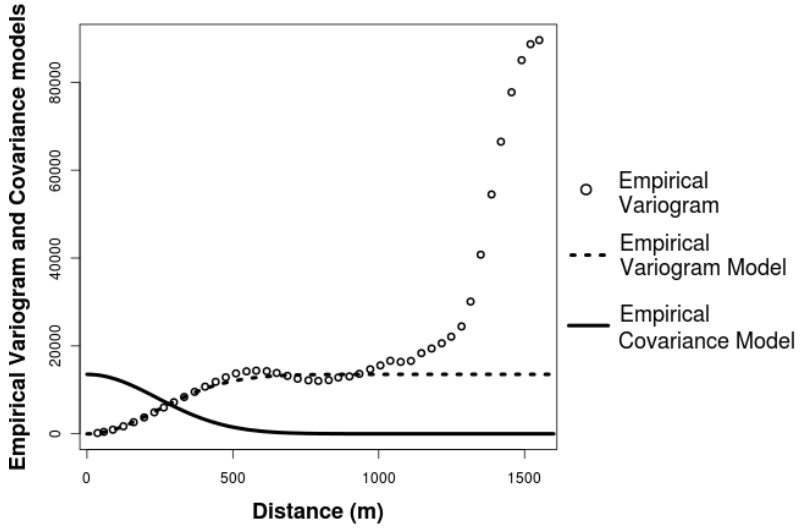

Figure 5.13: Region 3: empirical variogram, empirical variogram model and empirical covariance model (ASTER data)

Model (on the ASTER grid)	Accuracy (m)
SRTM (accuracy evaluated on the SRTM grid)	21.80
ASTER	15.32
ASTER prediction using collocation	15.38
Fusion by collocation prediction	15.44

Table 5.4: Mountain: fusion results

The noise variance value used, characterizing the empirical variogram model obtained, is the same for the ASTER and the SRTM datasets and it is equal to 34.15 m^2; in this case the window size considered for the collocation prediction is 2000 m $\times$ 2000 m, centred on the prediction point because after 1000 m the variogram model does not fit the empirical one.
The LiDAR comparison results, reported in Table 5.4, show that, also in the mountainous test area, the merging procedure did not improve the ASTER DSM.
This is mainly due to the fact that the SRTM dataset, in this area, has a worse accuracy than the ASTER one, so it does not give any contribution in

improving the height data.

5.4.6 Test region 4: mountain

The fourth region considered is again a mountainous one, represented in Figure 5.14 (number four in Figure 5.4), that covers an area of 1350 m × 1350 m, with boundaries defined by the following coordinates (in WGS84-UTM32N): north 5073260 m, south 5071910 m, east 506070 m and west 504720 m.

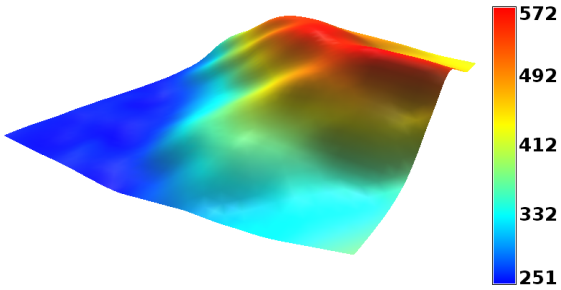

Figure 5.14: Region 4: mountain

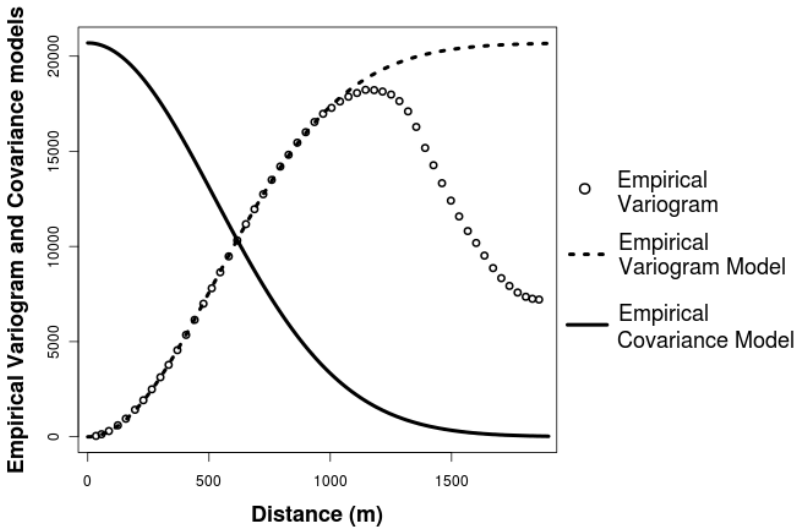

Figure 5.15: Region 4: empirical variogram, empirical variogram model and empirical covariance model (ASTER data)

Again the ASTER sparse points were used to obtain the empirical variogram model and then the empirical covariance one (Figure 5.13). The empirical variogram was fitted with a gaussian model (RMSE of 34.86 m), defined in Formula 5.39.

$$\begin{cases} y = Ae^{-\alpha d^2} \\ A = 17921 \\ \alpha = \dfrac{1}{664.4^2} \end{cases} \tag{5.39}$$

In the empirical covariance model the noise was characterized by a value of 7.545 m^2, that was used for both the ASTER and the SRTM noise matrix; the window size used for the collocation prediction is again 2000 m $\times$ 2000 m because, also in this test area, after 1000 m the empirical variogram model did not fit well the data.
The results obtained (Table 5.5) are similar to the one of the previous mountainous region, so the fusion result accuracy is worse than the original ASTER one; again, the problem is that the SRTM accuracy is far worse than the ASTER one, so the SRTM DSM does not provide any useful information to improve the ASTER DSM. Generally speaking, similar results should be expected in any areas characterized by steep slope because the SRTM DSM accuracy drops significantly within this kind of morphological features.

Model (on the ASTER grid)	**Accuracy (m)**
SRTM (accuracy evaluated on the SRTM grid)	15.73
ASTER	14.02
ASTER prediction using collocation	16.40
Fusion by collocation prediction	16.48

Table 5.5: Mountain: fusion results

5.4.7 Test region 5: plain

The fourth region is a plain one (identified as number five in Figure 5.4 and represented in Figure 5.16) and covers an area of 1350 m $\times$ 600 m (boundaries defined by the following coordinates in WGS84-UTM32N): north 5073500 m, south 5072150 m, east 506850 m and west 506250 m.
As before, the empirical covariance model was obtained using the ASTER sparse points falling into the region (Figure 5.17).

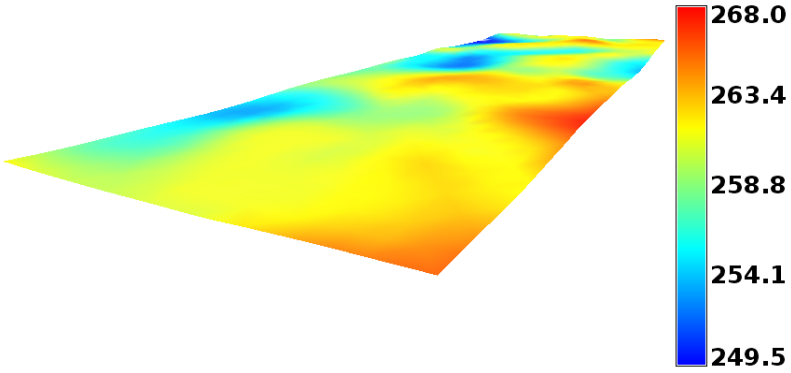

Figure 5.16: Region 5: plain

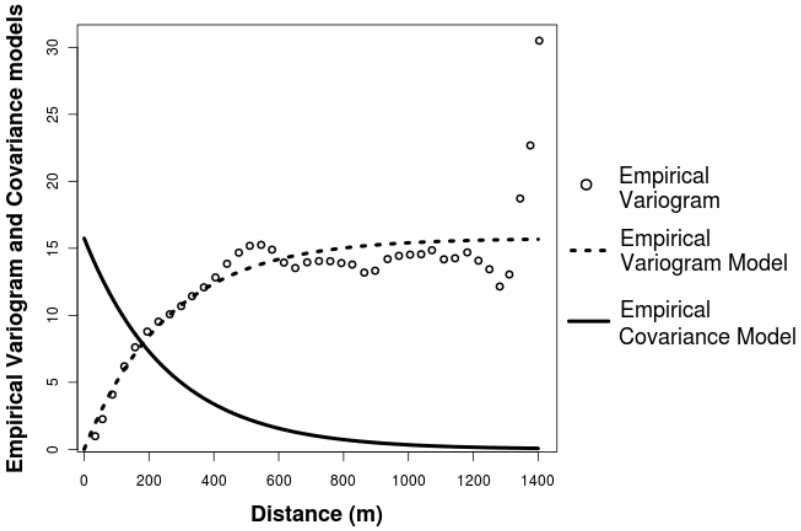

Figure 5.17: Region 5: empirical variogram, empirical variogram model and empirical covariance model (ASTER) data

The best empirical variogram model was an exponential one (RMSE from VESPER equal to 0.8839 m) and the corresponding empirical covariance model is defined in Formula 5.40:

$$\begin{cases} y = Ae^{-\alpha d} \\ A = 15.75 \\ \alpha = \dfrac{1}{260} \end{cases} \tag{5.40}$$

The correlation length used for the empirical variogram model definition is 1000 m, corresponding to a window of 2000 m $\times$ 2000 m around the point

to predict. A peculiarity of this empirical variogram model is that its noise variance is equal to zero; this may be due to the fact that the data, on which the empirical variogram was computed, were originally gridded. The noise variance in the variogram model tells how much the data are uncorrelated; probably in this case there is no uncorrelation because of the particular nature of the dataset.
Practically the value 0.0001 m^2 was used to avoid matrix singularity problems; this value was assigned both to the $\sigma^2_{\nu_A}$ and the $\sigma^2_{\nu_S}$.
The resulting DSMs were then compared to the LiDAR one to assess their accuracies, Table 5.6 shows the resulting accuracies.
In this test region the SRTM dataset brings an improvement on the ASTER one because it is more accurate (2.45 m against 7.04 m). Improvements of the ASTER by the SRTM are possible since the SRTM DSM has a better accuracy in the considered region, so it adds information to the ASTER DSM.

Model (on the ASTER grid)	**Accuracy (m)**
SRTM (accuracy evaluated on the SRTM grid)	2.45
ASTER	7.04
ASTER prediction using collocation	9.00
Fusion by collocation prediction	6.96

Table 5.6: Plain: fusion results using noise variances from the empirical covariance model

5.4.8 Test region 6: plain

The last region considered is a plain one (number six in Figure 5.4) and covers an area of 1290 m × 510 m which boundaries are defined by the following coordinates (in WGS84-UTM32N): north 5073500 m, south 5072150 m, east 506850 m and west 506250 m.

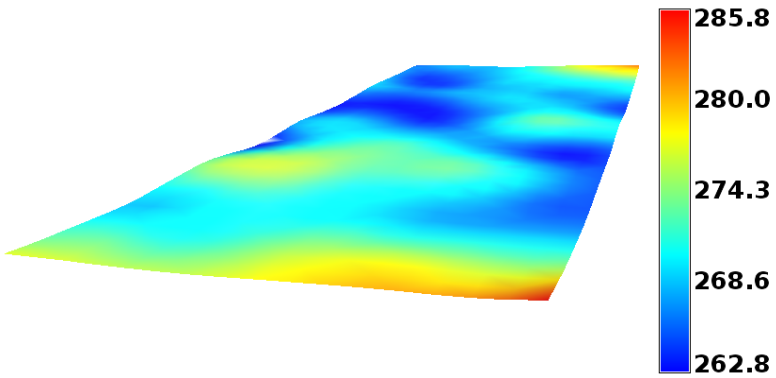

Figure 5.18: Region 6: plain

As before, the empirical covariance model was obtained using the ASTER sparse points falling into the region (Figure 5.19).

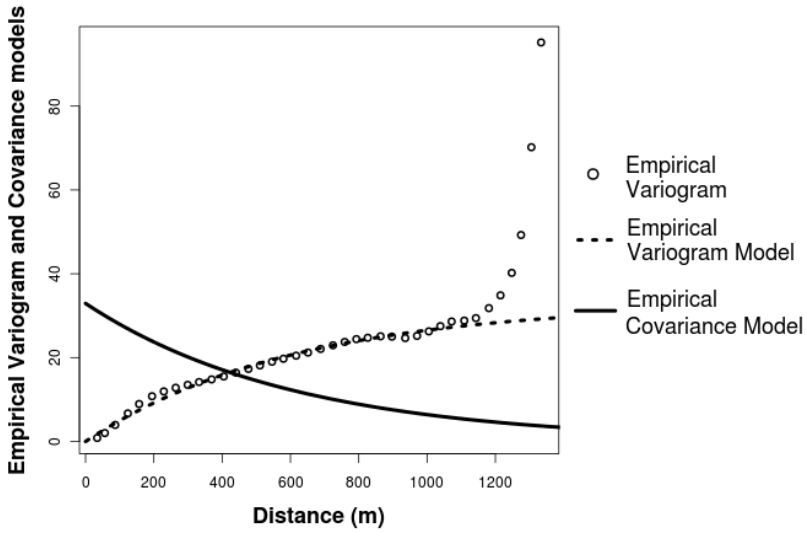

Figure 5.19: Region 6: empirical variogram, empirical variogram model and empirical covariance model (ASTER data)

The empirical variogram model chosen, because its RMSE (0.8238 m) was the lower one, was an exponential one, and the corresponding empirical covariance model is defined in Formula 5.41.

$$\begin{cases} y = Ae^{-\alpha d} \\ A = 32.94 \\ \alpha = \dfrac{1}{6} \end{cases} \tag{5.41}$$

The correlation length used is 1100 m, having so a window of 2200 m × 2200 m around the point to predict. Again the noise variance obtained from the empirical covariance model is equal to zero, so the value 0.0001 m^2 was used instead to avoid matrix singularity problems; this value was assigned both to the $\sigma^2_{\nu_A}$ and the $\sigma^2_{\nu_S}$.
The resulting DSMs were then compared to the LiDAR one to assess their accuracies, Table 5.7 contains the resulting accuracies.

Model (on the ASTER grid)	**Accuracy (m)**
SRTM (accuracy evaluated on the SRTM grid)	2.79
ASTER	6.77
ASTER prediction using collocation	9.99
Fusion by collocation prediction	7.35

Table 5.7: Plain: fusion results

This plain area does not confirm the results obtained in the fifth test area, in fact, even if the SRTM DSM has a greater accuracy than the ASTER model, the fusion does not bring improvements (accuracy of 7.35 m). These results confirm the fact that the collocation prediction is very area-dependent and it is not easy to find out which areas are better suited for its application.

5.4.9 Fusion on the ASTER grid with collocation: conclusion

The second fusion attempt was based on the use of the stochastic collocation method to predict the final DSM on the ASTER grid; its purpose was to test the possibility of improving a denser DSM (the ASTER one) using less dense information from another digital model with similar accuracy (the SRTM DSM).
The analysis was performed in six regions characterized by a specific morphology: hill, mountain and plain areas were considered.
The need to perform the computation on small regions was due both to the fact that the implemented method is not able to manage the whole dataset, and to the fact that it is time consuming.
The results on the test areas pointed out that the application of this merging

method is not worthy for all the dataset: in the mountain areas the SRTM accuracy is lower than the ASTER one, so the merged product is worse than the original one; in the hill areas the accuracies of the original DSMs are comparable, so the SRTM does not add significant information to the ASTER and the merged DSM has similar accuracy of the ASTER original model. The unique areas in which the fusion may represent an improvement with respect to the original ASTER DSM is the plain one: in correspondence with this morphology the SRTM DSM has a greater accuracy than the ASTER one, so it can provide additional information.
In conclusion the fusion on the ASTER grid is not advisable since improvements are possible only in areas where the SRTM accuracy is greater than the ASTER one.

5.5 Fusion on the SRTM grid using collocation

The fusion on the ASTER grid proved to be applicable but with bad results because improvements in the dataset are possible only in certain areas where the SRTM accuracy is greater than the ASTER one. To confirm this fact the collocation prediction was used to merge the two datasets on the SRTM grid on the same test area used previously: the expected result is an increasing of accuracy in the mountain areas and a decreasing of accuracy in the plain ones since the ASTER accuracy is greater in the steep slope areas than in the flat ones (opposite behaviour with respect to the SRTM).
The set up of the method is the same as the one used to predict in the ASTER grid (see section 5.4.2) and the empirical covariance function are the one obtained from the ASTER sparse points; the prediction was applied in the same regions used for the previous tests (Figure 5.20).
The resulting DSM were compared with the LiDAR or the photogrammetric DSMs to perform the external validation, the whole set of results is given in Table 5.8; this table contains also the accuracies of the DSM merged by the weighted average fusion procedure.

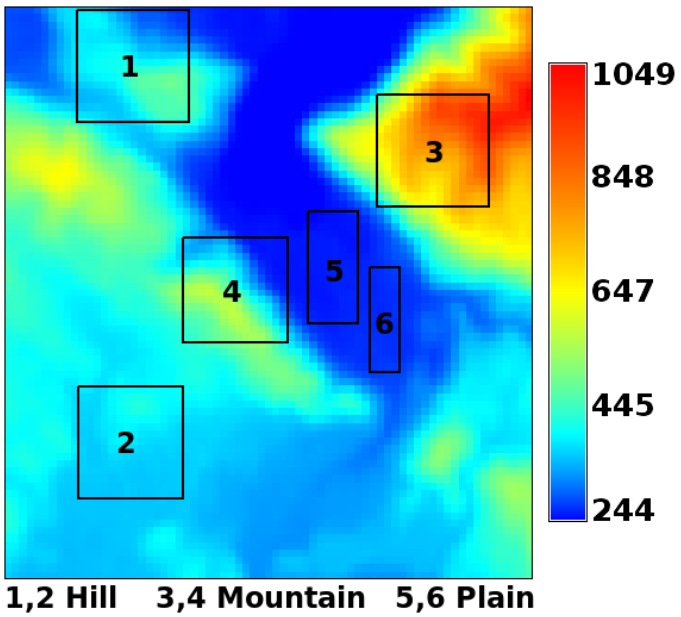

Figure 5.20: SRTM: testing area

	Accuracy (m)					
	Hill		Mountain		Plain	
Model (on the SRTM grid)	**1**	**2**	**3**	**4**	**5**	**6**
SRTM	10.42	6.28	19.23	16.30	2.47	2.94
ASTER (accuracy evaluated on the ASTER grid)	10.81	9.87	15.31	14.01	7.07	6.77
SRTM prediction using collocation	12.20	6.78	18.75	18.98	6.05	5.17
Fusion by collocation prediction	11.34	9.00	13.24	14.49	3.74	3.85
Weighted average fusion (nominal accuracy)	9.20	8.01	11.85	10.15	3.52	2.24
Weighted average fusion (accuracy from LiDAR)	9.07	7.78	11.69	10.06	3.29	2.17
Weighted average fusion (variable accuracy)	8.13	-	10.51	10.08	2.1	2.15

Table 5.8: Fusion on the SRTM grid: results

For all the six regions the covariance function and the noise variances used

to predict on the ASTER grid were used. The result in the first column of Table 5.8 shows that the collocation prediction of the merged DSM is an improvement with respect to the SRTM DSM, however its accuracy is lower with respect to the DSM obtained using the weighted fusion method.
Concerning the weighted fusion the results confirm what stated in Section 5.3.5, since the most accurate map with respect to the LiDAR DSM is the one obtained using variable weights depending on the slope gradient and aspect. The second region has a behaviour similar to the first one, unfortunately it is impossible to evaluate the weighted average fusion with variable accuracy since the LiDAR dataset did not cover this area, so the slope gradient and aspect classification was not available in the region.
Concerning the two mountainous regions the DSM resulting from the fusion with collocation have a better accuracy than the SRTM DSM (13.24 m and 14.49 m against 19.23 m and 16.30 m); unfortunately these improvements do not justify the use of the collocation prediction method since the weighted average merging provides more accurate DSMs (accuracy respectively of 10.51 m and 10.08 m).
The last two areas refers to the a plain morphology; in both cases the SRTM DSM has a higher accuracy than the ASTER one, for this reason, the improvement derived from the fusion is unimportant, so the fusion results are not an actual alternative to the SRTM dataset; however the accuracy of DSM merged with collocation is greater than the one of two DSMs obtained with the weighted average fusion using the nominal accuracies.

Chapter 6

Analysis of DSMs from radargrammetry

This last chapter proposes another example of DEM validation and fusion applied on models obtained with the radargrammetric method from data generated by the COSMO-SkyMed satellites. In this analysis the fusion step is applied on couples of DSMs obtained from images produced with ascending and descending satellite orbits; each model was validated with respect to the LiDAR data and different merging approaches were tried.

6.1 COSMO-SkyMed mission

COSMO-SkyMed (COnstellation of small Satellites for Mediterranean basin Observation) is a satellite mission for earth observation, commissioned and founded by Italian Space Agency (ASI) and Italian Ministry of Defense (MoD) and it is conceived for both civilian and defence use [Italian Space Agency, 2011].
The system consists of a constellation of four low Earth orbit mid-sized satellites, each equipped with a synthetic aperture radar (SAR) operating at the X-band (from 7 GHz to 12.5 GHz).

6.1.1 Mission and satellites: overview

The SAR was chosen as a multi-mode sensor operating in three main modality (Figure 6.1[1]):

[1]From COSMO-SkyMed System Description & User Guide

- Spotlight mode: acquisition of small areas of about 10 km × 10 km with resolution of 1 m × 1 m;
- Stripmap mode: the most common imagining mode, the swath is around 30-40 km and the resolution varies between 3 m and 15 m;
- ScanSAR mode: it covers huge areas, the swath varies between 100 km and 200 km, while the resolution is between 30 m and 100 m.

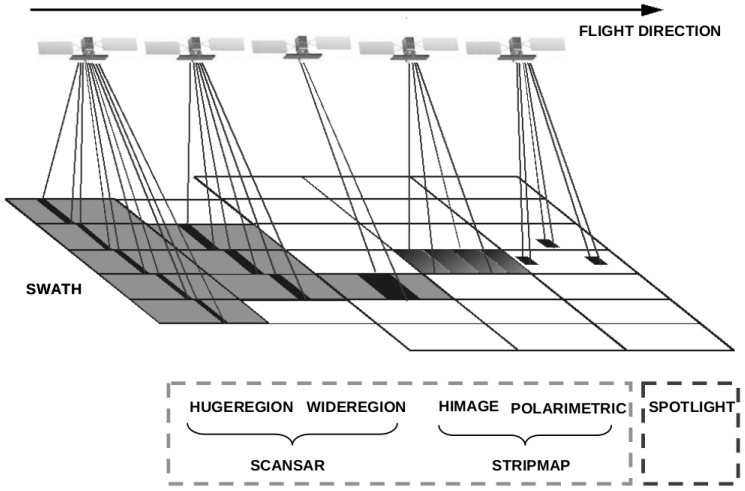

Figure 6.1: COSMO-SkyMed acquisition mode

The constellation consists of four medium sized satellites, the characteristics of their orbit are summarized in Table 6.1.

Orbit characteristics	
Orbit type	Sun-synchronous orbit (SSO)
Inclination	97.86°
Revolutions/day	14.8125
Orbit cycle	16 days
Eccentricity	0.00118
Semi major axis	7003.52 km
Number of satellites	4
Phasing	90°

Table 6.1: Satellite orbit characteristics

In the nominal constellation orbital configuration the four satellites are equi-phased in the same orbital plane; this configuration is conceived to achieve the best compromise between cost and performances, since it allows to access the same target on Earth at least twice a day under different observing conditions (incidence angle). The interferometric satellite configuration, instead, has the aim to produce three-dimensional SAR images by combining two radar measurements of the same point on the ground.
The architecture of the satellite consists of:

- Integrated Control Subsystem (ICS): the controlling system on board for the collection and distribution of information such telemetry, on board data and timing;
- Telecommands Protection System (TPS): provides on-board decryption of the telecommands received from the ground;
- Telemetry Tracking & Command (TT&C): provides the two ways communication links between the satellite and the TT&C ground station;
- Electric Power Subsystem (EPS): composed of solar array wings, drive motors to orientate the Solar Array wings, a power control unit and the SAR antenna power supply;
- PRopulsion Subsystem (PRS): includes six thrusters arranged in two independent branches of three each;
- THermal Control subsystem (THC): consists in the elements that insulate the external surface of the satellite;
- SAR instrument: an X-band radar operating in multi-resolution and multi-polarization on a wide area access region
- Payload Data Handling and Transmission (PDHT): manages all the data generated by the SAR system.

6.2 Radargrammetry

A DEM can be extracted from SAR data by interferometry or radargrammetry (for further details see Section 1.1.4), the former uses phases differences between two signals contained in the SAR images to obtain terrain elevation, the latter analyses the signal amplitude and uses stereoscopy (like in photogrammetry) on the optical images.
Usually the radargrammetry is employed with stereoscopic pairs acquired

from the same side but with different incidence angles; this approach was first used in the 1950s; then, due to the fact that SAR images had high resolution in phase but low resolution in amplitude, the interferometric approach has been usually preferred to the radargrammetric one. In the last decade new SAR products, characterized by a very high resolution, became available (e.g TerraSAR-X, Radarsat-2), so some experimentation using the radargrammetric analysis were performed again [Raggam et al., 2010, Toutin and Chenier, 2009].
The image analysis is analogue to the one in photogrammetry, forming a stereo model for 3D measurement; the images contain the amplitude information and their grey tones depend the imaged surface, since radiation is reflected according to geometrical and physical terrain characteristics.
The best geometric configuration for radargrammetry consists in a target observed from two different points of view with a large base and different look angles.
The radargrammetric analysis can be implemented both in an interactive approach or an automated one [Crosetto and Aragues, 1999]. In the former the operator has to capture manually the data, while in the latter algorithms are adopted to extract pairs of homologous points, so the operator has only to supervise the matching operation.
In the following section the operations, performed by the Geodesy and Geomatic Area at La Sapienza University of Rome, to extract homologous points from the available dataset are described.

6.2.1 Datasets extraction

Two couples of COSMO Spotlight images in zero Doppler/slant range projection (two from ascending orbits and two from descending ones) were available in the area of Como under analysis (see Table 6.2 for their characteristics); the data from the COSMO-SkyMed were too few to apply an interferometric analysis, but they were suitable for a radargrammetric one.
The images were processed at La Sapienza University of Rome to obtain, in two test region, two datasets of points that were then interpolated to generate the DSMs.
The radargrammetric analysis consists in two main steps:

- geometric aspect: image orientation (rigorous models or RPCs);
- homologous points search: image matching.

	Image 1	**Image 2**	**Image 3**	**Image 4**
Acquisition date	24/06/2011	28/06/2011	17/06/2011	07/08/2011
Dimension (km^2)	10 × 10	10 × 10	10 × 10	10 × 10
Average incidence angle (deg)	27.8	55.4	50.8	28.9
Orbit	descending		ascending	
Look side	right			
Base to height ratio (B/H)	0.8		0.6	

Table 6.2: Images from COSMO-SkyMed: characteristics

The image orientation consists in the determination of the sensor-object stereo model to perform a 3D reconstruction; the object position is given by the intersection of two radar rays with different look angles. The model is based on two fundamental equations: the equation representing the zero-Doppler projection and the slant range constrain [Capaldo et al., 2011b].
The satellite orbit was modelled as circular arc, since the orbital arc, related to image acquisition in Spotlight mode, is quite short. The orbital parameters were estimated in a least square adjustment using orbital state vector available in the image metadata.
The model was then reconstructed using the SISAR software, developed by the team of Geodesy and Geomatic Area at La Sapienza University of Rome using a RPFs approach [Crespi et al., 2007]. The rational polynomial functions model (RPFs) relates the object point coordinates to the pixel ones in the form of ratios of polynomial expressions whose coefficients (RPCs) are often supplied with the imagery [Crespi et al., 2010, Capaldo et al., 2011b].
Once the image orientation step is concluded, and before searching the homologous points, an additional operation was performed to reduce the noise level in the images: in fact, SAR imagery is affected by a high level of noise, in particular the largest source of noise is the speckle one which gives a grainy appearance to the SAR image preventing target recognition [Capaldo et al., 2011a]. The noise was reduced using the adaptive Lee filter on a 7 x 7 pixels window.
This filter was designed by Lee [Lee, 1980] as a combination of an additive and multiplicative white noise filtering. The basic assumption of this approach is that the sample mean and variance of a pixel is equal to the local mean and variance of all the pixels within a fixed range surrounding it; various

tests [Shi and Ko, 1994, Yu and Acton, 2002] proved the effectiveness in the speckle noise removal. This filter [Lopes et al., 1990] can be formulated as:

$$\begin{aligned} &\widehat{R}(p) = I(p)\,W(p) + \overline{I}(p)\,(1 - W(p)) \\ &\text{where } W(p) = 1 - \frac{C_u^2}{C_I^2} \\ &\text{and } C_u = \frac{\sigma_u}{\overline{u}};\; C_I(p) = \frac{\sigma_I(p)}{\overline{I}(p)} \end{aligned} \tag{6.1}$$

in Formula 6.1 p identifies the single pixel to which the filter is applied, R corresponds to the actual terrain reflectivity, I to the image corrupted by the speckle noise (u). $C_I(p)$ and C_u are respectively the image and the speckle noise variation coefficients, while W is the weight function applied in the noise reduction.
Once filtered, the images were suitable for the final step of the radargrammetric analysis, consisting in the image matching.
To carry on this step, usually, one of the two classical matching strategies is used:

- Area Based Matching (ABS): the primitive to be searched is a small window covering some pixels, the matching criterion is the cross-correlation coefficient between the primitive and its matching area;

- Feature Based Matching (FBM): the primitives to be searched are some features in the image, like corners, edges, etc...

Unfortunately neither method was suitable for SAR images matching, due to the complex radiometry of SAR image and the possible presence of geometrical deformations (foreshortening and layover), so a new approach was developed by the team of Geodesy and Geomatic Area at La Sapienza University of Rome.
The matching method is based on a coarse-to-fine hierarchical solution with a combination of geometrical constraints and an ABM algorithm [Capaldo et al., 2011a,b].
The homologous points are identified at first by the cross-correlation criterion and then improved with the least squares matching; these are the main methods to assess similarities in an ABM approach. The algorithm has a pyramidal structure, at first the images resolutions are reduced by a certain factor and then progressively they are restored to the original values. At each step an intermediate model is extracted and and it is modelled by the triangular irregular network (TIN) using a 2D Delauney triangulation method. A Voronoi polygons median filter is applied on the model to reduce spikes.

The model is refined at each step of the pyramid until the final one, in which the spatial resolutions correspond to the original ones. With this approach at first larger structures are detected (pyramid steps corresponding to lower resolutions), while restoring progressively the original resolution allows the detection of smaller details that are added to the coarse surface. From the two stereo-couples two point wise dataset were extracted: for each test an ascending and a descending data sets were available; it is necessary to point out that in the matching step all the points characterized by a correlation coefficients lower than 0.75 were not included in the data sets.

6.3 Fusion methods

The analysis of the radargrammetric data was performed in two test areas in which the datasets of matched points were provided. In each area two point-wise datasets were available: the former from an ascending orbit and the latter from a descending one; each dataset provided, for each point, the height value and the correlation coefficient from the image matching step. As said in Section 6.2.1, the points with correlation coefficient lower than 0.75 were not included in the datasets.
The aim of this analysis is the assessment of the best procedure to merge radar data obtained from different orbit orientation.
The availability of two point-wise datasets and their correlation coefficients allowed the test of different approaches in the data fusion:

- merging of the point-wise datasets and interpolation on the resulting set of points;
- fusion using as constant vertical accuracies the ones derived from the LiDAR DSM comparison;
- fusion using the accuracies derived from the slope gradient and aspect analysis;
- application of the above strategies on the point-wise datasets filtered using the correlation value (i.e. removing the points with correlation lower 0.85).

The DSMs obtained from the first fusion methods were internally validated following the procedure described in Section 3.2, each DSM was compared to the LiDAR DSM, taken again as ground truth.
In the following Sections the results obtained in the two test area are described.

6.4 First test area

The first area of analysis covers a region near the lake of Como; since the radargrammetric method does not provide points on water bodies, the area covered by the lake was cut out from all the digital surface models produced on this area; Figure 6.2 shows the LiDAR DSM in the region under analysis; as done previously, the LiDAR DSM was used for validating the radargrammetric models. Figure 6.2 shows also the ascending (blue) and descending (violet) point-wise dataset, it is evident that their disposition is not homogeneous over the area.

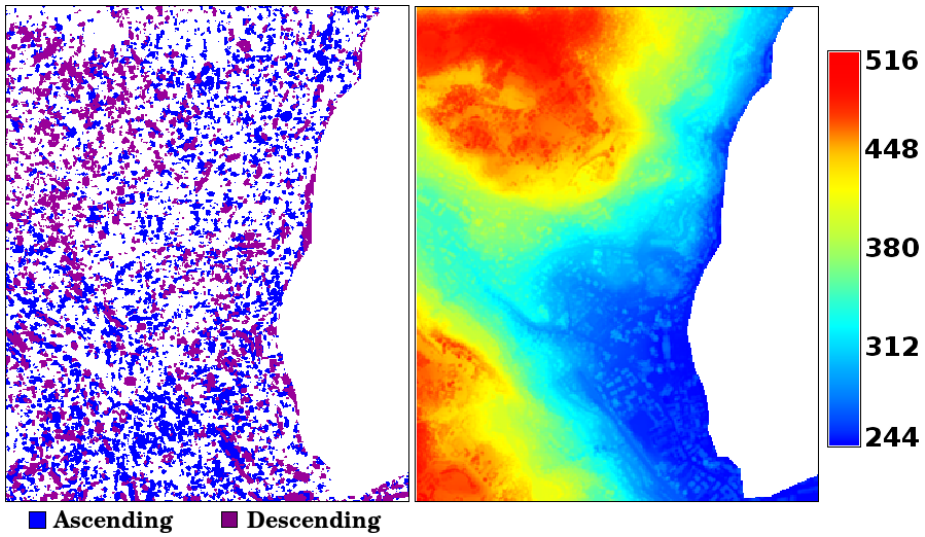

Figure 6.2: First area: radargrammetric points and LiDAR DSM

In the first analysis all the points belonging to the ascending and descending orbit images were used for the elaborations. At first the two datasets were interpolated separately, using the bilinear method, to obtain two DSMs. The two point-wise datasets were also merged and then this whole set of points that was interpolated using bilinear splines; of course, this corresponds to data fusion, in particular it is interesting to evaluate, in the radargrammetric field, if it is more advisable to merge the data before or after the interpolation. To generate the ascending DSM 230004 points were interpolated, while for the descending one 132287 points were considered. In the following they are referred as: DSM_A (Figure 6.3 on the left) the one obtained from the ascending dataset only, DSM_D (Figure 6.3 on the right) the one from the descending dataset and DSM_{AD} (Figure 6.4) the one obtained from the interpolation of the merged dataset.

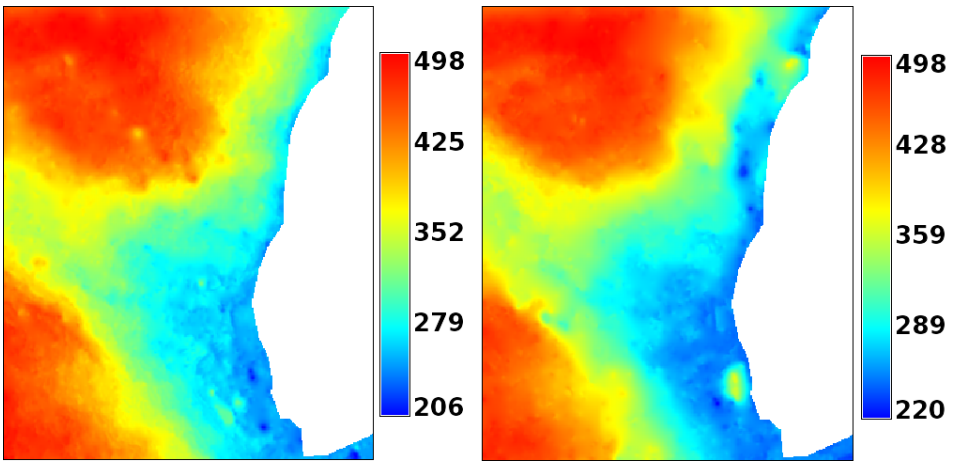

Figure 6.3: First area: DSM_A (left) and DSM_D (right)

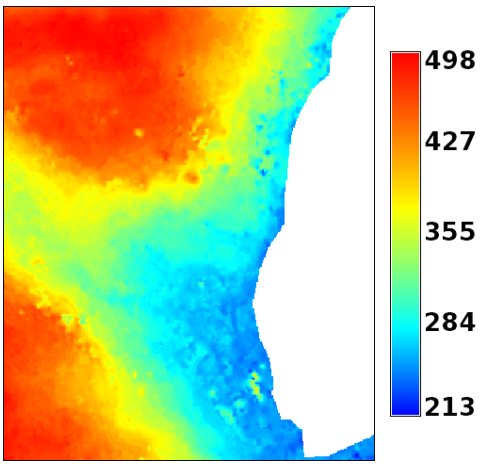

Figure 6.4: First area: DSM_{AD}

6.4.1 Validation and ANOVA analysis

The three digital models were internally validated following the procedure described in Section 3.2, each model was validated using the bilinear interpolation method with a 3×3 window and an α value of 0.0002 (settings obtained from the execution of r.outldetopt, see Section 3.2.2 for details); Table 6.3 contains the information regarding the number of outliers found. The outliers are, for all the three maps, spread in the whole area, so they are not caused by a particular feature; they are characterized by height values covering the whole height field.

Model	Outlier count	Total cell count	Percentage of outlier
DSM_A	14	106134	0.013%
DSM_D	19	106134	0.018%
DSM_{AD}	30	106134	0.027%

Table 6.3: Internal validation: results

The comparison with the LiDAR DSM was performed after the outlier removal step; the statistics were computed in a LE95 approach: only the 95% of data were used; for each DSM is then indicated the accuracy and the LE95 value corresponding to the difference value used ad threshold to exclude the data.

- DSM_A: accuracy 7.56 m; LE95 20.24 m
- DSM_D: accuracy 9.65 m; LE95 30.34 m
- DSM_{AD}: accuracy 7.24 m; LE95 19.72 m

From these first results it is possible to observe that the interpolation of the whole dataset is better than the one of the descendent orbit data only; this happens because less points are available for the descending DSM interpolation (around an half of the ascending available points).

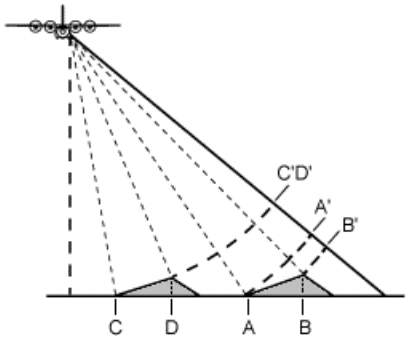

Figure 6.5: Foreshortening example

The extraction of a lower number of points from the descending stereo-couple is caused by the major presence of foreshortening distortion that influence the detection of homologous points; this effect is a typical feature of the SAR images. Foreshortening happens because the relative position of points in a

SAR image is given by the time delay between the radar echoes received from them. Figure 6.5 shows an example of this effect, it is evident that, in case of slopes, two points may be detected with a relative distance lower than the actual one.
The external validation step included also the ANOVA analysis to assess possible dependences on the terrain morphology; the results, in terms of accuracies of the single gradient-aspect classes, were also used in the merging procedure as weight. The analysis of variance was performed as described in Chapter 4, in this case eight slope aspect classes of 45° each were considered, the four slope gradient classes were defined, as done in Chapter 4, using the gradient map 25%, 50% and 75% percentiles: 15°, 27° and 40°.
Figure 6.6 shows, from left to right, the slope gradient and aspect classifications, while Figure 6.7 shows the combination of classes used in the ANOVA. The ANOVA results (Table 6.4) show that all the three models depends on both slope gradient and aspect.

	$\mathbf{DSM_A}$	$\mathbf{DSM_D}$	$\mathbf{DSM_{AD}}$
H_0: slope gradient has no influence			
Degrees of freedom	v_1=3,v_2=21		
F_{teo} with $\alpha = 0.01$	4.87		
F_{teo} with $\alpha = 0.05$	3.07		
F_{emp}	35.16	26.29	38.43
H_0: slope aspect has no influence			
Degrees of freedom	v_1=7,v_2=21		
F_{teo} with $\alpha = 0.01$	3.64		
F_{teo} with $\alpha = 0.05$	2.49		
F_{emp}	17.58	22.16	8.8

Table 6.4: ANOVA results

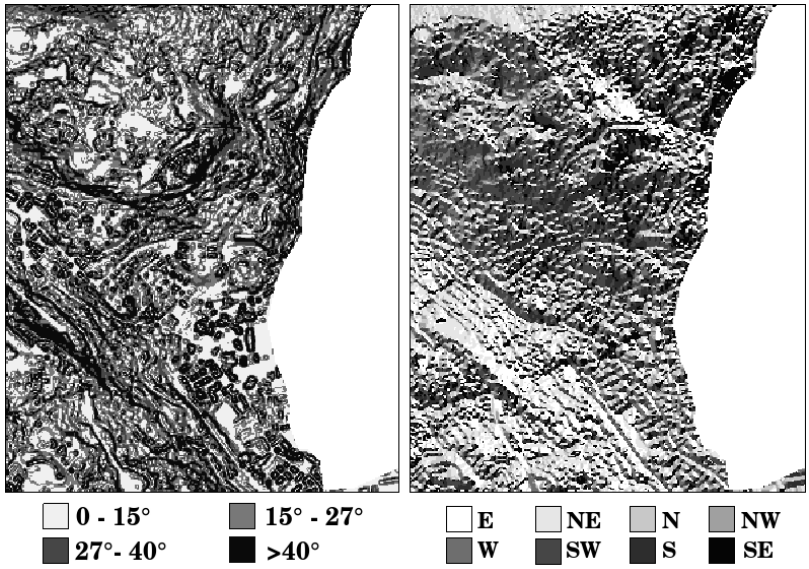

Figure 6.6: Slope gradient (left) and aspect (right) classifications

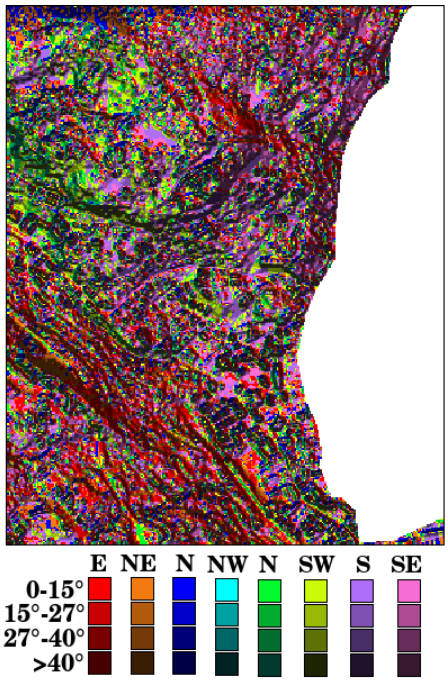

Figure 6.7: Combination of slope gradient and aspect classes

Table 6.6, 6.7 and 6.8 display the accuracies (in meters) of the ANOVA

classes with respect to the LiDAR DSM respectively of the DSM_A, DSM_D and DSM_{AD}; Table 6.5 shows the absolute frequency of the different ANOVA classes, the frequencies depends on the slope gradient and aspect classification, so they are the same for each DSM analized.
It is interesting to notice that the data from the ascending and the descending orbits present different degree of accuracy: the standard deviations of the DSM_A are all around the 10 m, while the ones of the DSM_D are higher and more variable (from 10 m to 20 m). If the two point-wise dataset are merged (DSM_{AD}) the errors caused by the points from the descending orbit image are mitigated thanks to the ascending orbit points (Table 6.8).

		Aspect							
		N	NW	W	SW	S	SE	E	NE
Gradient	0 - 15°	1759	1566	1845	2387	2940	3044	2827	2338
	15° - 27°	1779	1467	1794	2632	3357	3665	3550	2533
	27° - 40°	1759	1318	1629	2518	3387	3835	3934	2718
	> 40°	1448	1082	1420	2348	2999	3678	3982	2853

Table 6.5: Area 1: absolute frequencies

		Aspect							
		N	NW	W	SW	S	SE	E	NE
Gradient	0 - 15°	10.00	9.62	9.48	8.72	8.99	9.11	9.66	10.07
	15° - 27°	9.39	9.21	9.61	9.53	9.83	9.35	8.53	9.15
	27° - 40°	9.08	9.05	10.39	9.98	10.30	9.52	8.46	9.12
	> 40°	10.84	10.42	11.65	11.62	11.25	9.86	9.54	11.46

Table 6.6: DSM_A: class standard deviation values [m]

		Aspect							
		N	NW	W	SW	S	SE	E	NE
Gradient	0 - 15°	13.37	14.47	12.50	11.39	11.32	11.74	11.83	10.72
	15° - 27°	13.11	15.51	13.18	11.64	12.74	14.81	14.00	13.33
	27° - 40°	12.44	15.11	13.87	12.08	14.64	16.57	15.61	14.25
	> 40°	11.56	12.21	15.01	11.75	16.27	19.58	18.20	15.21

Table 6.7: DSM_D: class standard deviation values [m]

		Aspect							
		N	NW	W	SW	S	SE	E	NE
Gradient	0 - 15°	9.98	10.77	9.51	8.76	8.34	9.18	9.92	8.95
	15° - 27°	9.43	10.39	9.37	9.19	10.16	9.69	9.14	9.40
	27° - 40°	8.98	9.47	10.85	9.44	10.37	10.21	9.56	9.34
	> 40°	10.05	9.92	11.55	10.51	11.96	11.45	10.73	10.72

Table 6.8: DSM_{AD}: class standard deviation values [m]

6.4.2 Fusion tests

As introduced before, some fusion strategies were applied to the DSM from radargrammetric data to find a way to merge data from ascending and descending orbits.
Some weighted average fusion methods were tried; the collocation was not considered as a possible choice since the results obtained in Chapter 5 did not bring any significant improvement with respect to the original model. Another problem in the collocation application consists in the amount of data processable by the algorithm and the long execution time.
The test performed cover the fusion methods listed in Section 6.3.

Fusion using the standard deviation from the LiDAR DSM comparison: the first fusion attempt is a simple weighted average fusion using, as weights, the accuracies obtained from the LiDAR DSM comparison.
The merged result, for each cell (F in Formula 6.2), was computed in the following way:

$$F = \frac{\frac{DSM_A}{\sigma_A^2} + \frac{DSM_D}{\sigma_D^2}}{\frac{1}{\sigma_A^2} + \frac{1}{\sigma_D^2}} \tag{6.2}$$

The accuracy of the merged DSM, computed with respect to the LiDAR DSM, is 6.87 m (computed with LE95 of 17.53 m), so it is an improvement with respect to both the ascending and descending interpolated DSMs.

Fusion using the accuracies from the slope gradient and aspect classification: this fusion approach, described also in Section 5.3.4, uses as weight the accuracies obtained, for each slope gradient and aspect class,

from the comparison with the LiDAR DSM (in this case the Tables 6.6, 6.7 and 6.8).
The shortcoming of this method is the necessity to have another digital model on which the gradient and aspect maps are computed. The accuracy of the resulting DSM, obtained from the comparison with the LiDAR DSM is 6.80 m (LE95 of 17.39 m), so, also in this case, this methods provides significant improvement with respect to the original data.
In this case there is not significant improvement with respect to the fusion done using a constant accuracy value obtained from the comparison with the LiDAR DSM; this happens because these data do not have highly variable accuracies among the slope gradient and aspect classes.

6.4.3 ANOVA and fusion of the data filtered on the coherence value

As introduced in Section 6.3, the radargrammetric points were provided with a coherence value associated. This value represents the reliability of the point extracted in the image matching step; points with coherence lower than 0.75 were excluded a priori, since they were not reliable enough.
The previous fusion tests were done on digital surface models generated interpolating the whole point-wise dataset. This test was done to find out if removing less reliable points could bring improvements with respect to the results previously obtained.
In the following the results obtained filtering the points with coherence value greater than 0.85 are presented; the interpolation procedure was analogue to the one that was used to produce the ascending and descending DSM analysed previously, so again two 5 m cell spaced DSMs, from the ascending and the descending datasets, were created. The ascending DSM ($DSM_{A-0.85}$) was created interpolating 65769 points, the descending one ($DSM_{D-0.85}$) interpolating 43767 points (from left to right in Figure 6.8), while the $DSM_{AD-0.85}$ (6.9) was created using the two datasets.
The external validation, performed by comparing the DSMs with the LiDAR one, produced the following results in a LE95 approach:

- $DSM_{A-0.85}$: accuracy 7.37 m; LE95 18.90 m
- $DSM_{D-0.85}$: accuracy 9.20 m; LE95 22.04 m
- $DSM_{AD-0.85}$: accuracy 6.77 m; LE95 17.37 m

The ANOVA analysis was carried on also on these DSMs.

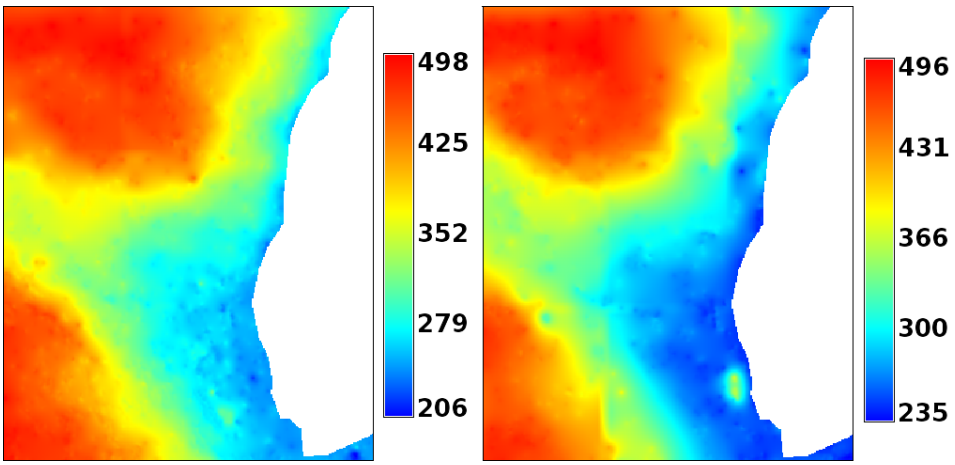

Figure 6.8: First area: $DSM_{A-0.85}$ (left) and $DSM_{D-0.85}$ (right)

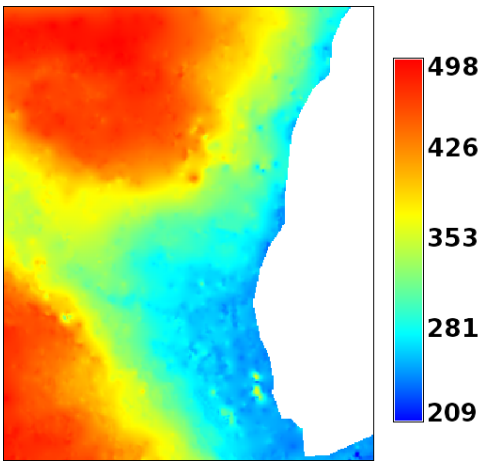

Figure 6.9: First area: $DSM_{AD-0.85}$

ANOVA: the analysis was carried on as in Section 6.4.1, using the same slope gradient and aspect classification (see Figure 6.6 and Figure 6.7); Table 6.10, 6.11 and 6.12 contain the accuracies of the classes, the absolute frequencies, depending only on the slope gradient and aspect classification are the same as in Table 6.5.
The accuracies of the data filtered upon the coherence value have accuracies similar to the non filtered DSMs (see Table 6.6, 6.7 and 6.8); again, the descendent DSM has lower accuracies with respect to the ascending one.
The ANOVA results, presented in Table 6.9, show that the three filtered DSMs

have dependencies on both the slope gradient and the aspect; comparing this analysis with the one done on the DSM from the whole dataset the results are almost similar, the only main difference is the slope gradient dependence of the ascending DSM: after the filtering its entity is much lower.

	$\mathbf{DSM_{A-0.85}}$	$\mathbf{DSM_{D-0.85}}$	$\mathbf{DSM_{AD-0.85}}$
H_0: slope gradient has no influence			
Degrees of freedom	v_1=3,v_2=21		
F_{teo} with $\alpha = 0.01$	4.87		
F_{teo} with $\alpha = 0.05$	3.07		
F_{emp}	8.74	30.95	26.77
H_0: slope aspect has no influence			
Degrees of freedom	v_1=7,v_2=21		
F_{teo} with $\alpha = 0.01$	3.64		
F_{teo} with $\alpha = 0.05$	2.49		
F_{emp}	23.01	17.18	5.02

Table 6.9: Filtered data: ANOVA results

		Aspect							
		N	NW	W	SW	S	SE	E	NE
Gradient	0 - 15°	9.90	9.26	9.29	8.98	8.64	8.99	9.56	9.92
	15° - 27°	9.58	9.05	9.38	9.08	9.25	9.05	8.40	9.22
	27° - 40°	8.96	9.08	10.35	9.64	9.47	9.03	7.90	9.06
	> 40°	9.92	9.28	10.29	10.49	10.07	9.28	8.41	10.38

Table 6.10: $DSM_{A-0.85}$: class standard deviation values [m]

		Aspect							
		N	NW	W	SW	S	SE	E	NE
Gradient	0 - 15°	12.38	13.68	11.48	10.35	10.08	10.63	10.93	9.93
	15° - 27°	12.75	14.24	12.14	10.74	11.54	13.13	12.95	12.58
	27° - 40°	11.92	14.33	13.07	11.31	13.13	13.53	13.65	13.08
	> 40°	11.48	11.21	14.07	11.31	14.33	15.97	15.04	14.09

Table 6.11: $DSM_{D-0.85}$: class standard deviation values [m]

		Aspect							
		N	NW	W	SW	S	SE	E	NE
Gradient	0 - 15°	9.13	9.86	8.24	7.69	7.75	8.18	8.87	8.80
	15° - 27°	8.91	9.40	8.19	8.15	8.65	8.70	8.58	8.85
	27° - 40°	8.44	8.52	9.65	8.64	9.04	8.65	8.26	8.87
	> 40°	9.17	8.59	10.35	9.45	10.47	9.76	9.30	9.80

Table 6.12: $DSM_{AD-0.85}$: class standard deviation values [m]

Fusion tests: the ascending and descending DSMs were merged applying the same strategies considered in Section 6.4.2. In the first approach the accuracies from the external validation step were used for weighting the DSMs to be fused, obtaining a DSM which accuracy is 7.04 m (LE95 of 16.70 m). The fusion based on the variable weights from the slope gradient and aspect classification provided a DSM with accuracy of 6.97 m (LE95 16.96 m). From these results it is possible to conclude that the filtering on the basis of the coherence value does not improve the DSM accuracy.

6.5 Second test area

Radargrammetric data were available also in a second area covering part of the Como area (Figure 6.10). In this area two point-wise datasets (ascending and descending) were available, too; it is interesting to point out that the datasets of this area and the ones of the first area were extracted from the same COSMO-SkyMed images, consequently the ascending and descending derived DSMs in this second region should have the same characteristics of the DSMs analysed in Section 6.4.

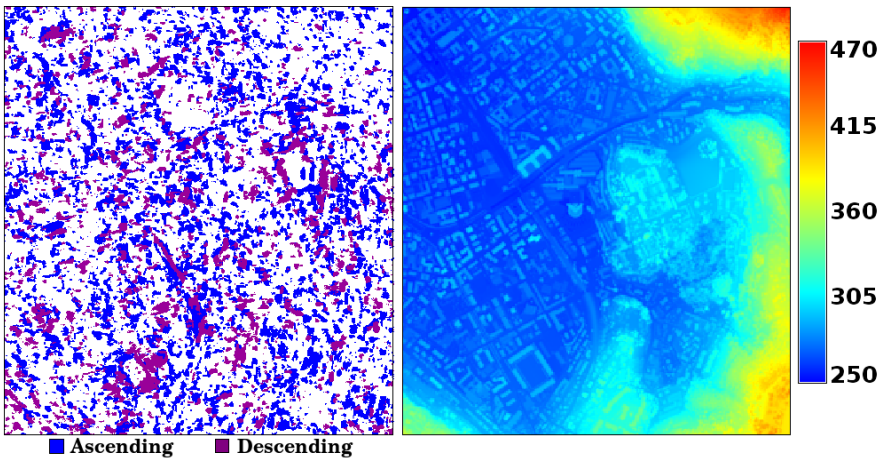

Figure 6.10: Second area: radargrammetric points and LiDAR DSM

As before the DSM from ascending data is referred as DSM_A (on the left in Figure 6.11), the one from descending data as DSM_D (on the right in Figure 6.11) and the one obtained from the interpolation of the merged point datasets as DSM_{AD} (Figure 6.12). DSM_A was created interpolating 251341 points, while for DSM_D 89668 points were present in the area; again the number of points belonging to the descending dataset is less than a half of the points belonging to the ascending one.

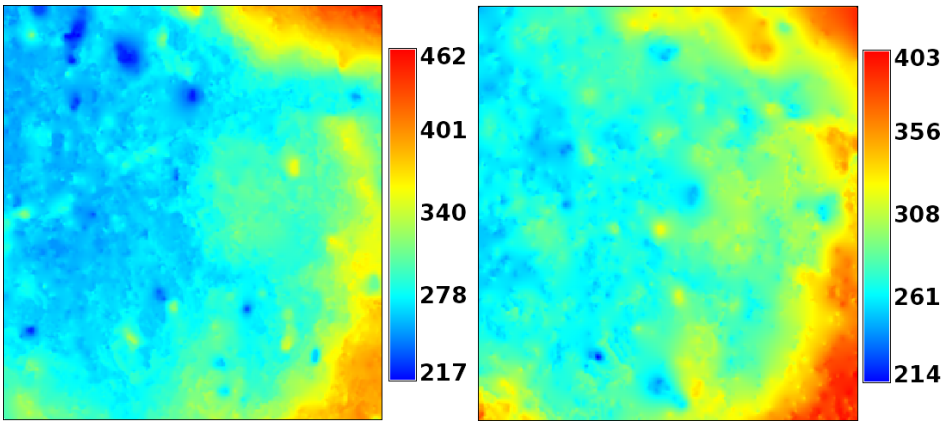

Figure 6.11: Second area: DSM_A (left) and DSM_D (right)

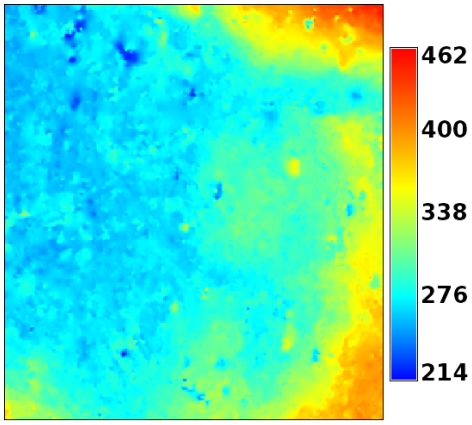

Figure 6.12: Second area: DSM_{AD}

6.5.1 Validation and ANOVA analysis

The three DSMs were internally validated following the procedure presented in Section 3.2. Each digital model was validated using a bilinear method with a window of dimension 3×3 pixel and a significance level α equal to 0.0002. Table 6.13 indicates, for each model, the number of outliers found. The outliers, also in this region, are not localized in a particular area but they are spread in the whole region; their heigh value, also, covers the whole height field of the model. The external validation, done after the outlier removal step, corresponding to the comparison with the LiDAR DSM, provided the following results (in a LE95 approach):

- DSM_A: accuracy 8.70 m; LE95 23.88 m
- DSM_D: accuracy 11.54 m; LE95 33.08 m
- DSM_{AD}: accuracy 8.70 m; LE95 22.76 m

Model	Outlier count	Total cell count	Percentage of outlier
DSM_A	14	76560	0.031%
DSM_D	19	76560	0.013%
DSM_{AD}	36	76560	0.047%

Table 6.13: Internal validation: results

The accuracies obtained are similar to the corresponding ones in the first area; they confirm that the data from the descending orbit are less accurate with respect to the data from the ascending orbit. Again, the interpolation of the merged point-wise datasets is an improvement with respect the descending DSM but not with respect the ascending one.

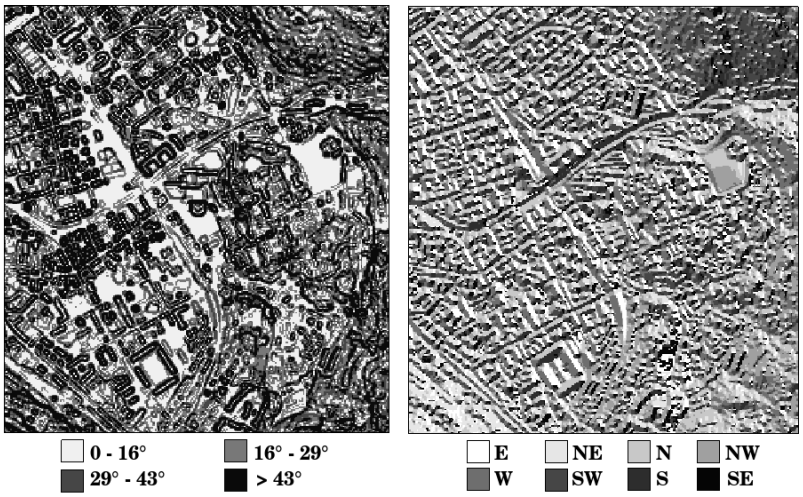

Figure 6.13: Slope gradient (left) and aspect (right) classifications

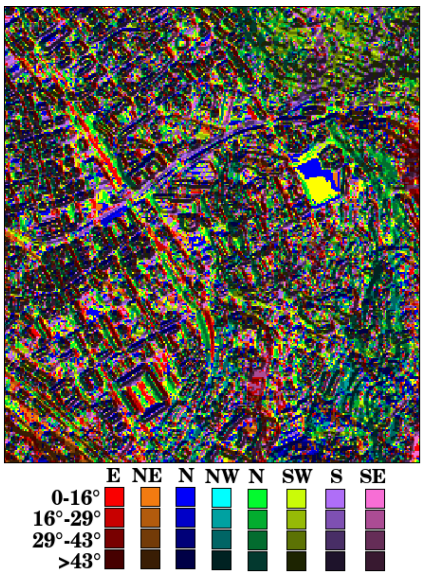

Figure 6.14: Combination of slope gradient and aspect classes

The last analysis concerning the validation step is the ANOVA one. The procedure is the same as in Section 6.4.1; the slope gradient and aspect maps were computed on the 5 m cell spacing resampled LiDAR DSM, the aspect map was classified in eight classes each covering 45°, the gradient was dividend in four classes on the basis of the gradient map 25%, 50% and 75% percentiles (16°, 29° and 43°). Figure 6.6 displays the slope gradient and aspect classifications, while Figure 6.14 shows the combination of the two classifications. The three models show dependences on both the gradient and the aspect (see Table 6.14), in particular the DSM_A is more dependent on the slope gradient while the DSM_D shows the opposite behaviour. The ANOVA produced similar results for the ascending and descending DSMs in the first area under analysis.

	$\mathbf{DSM_A}$	$\mathbf{DSM_D}$	$\mathbf{DSM_{AD}}$
H_0: slope gradient has no influence			
Degrees of freedom	v_1=3,v_2=21		
F_{teo} with $\alpha = 0.01$	4.87		
F_{teo} with $\alpha = 0.05$	3.07		
F_{emp}	61.83	7.84	32.39
H_0: slope aspect has no influence			
Degrees of freedom	v_1=7,v_2=21		
F_{teo} with $\alpha = 0.01$	3.64		
F_{teo} with $\alpha = 0.05$	2.49		
F_{emp}	11.18	85.66	10.53

Table 6.14: ANOVA results

Considering the ANOVA classes accuracies (Table 6.16, 6.17 and 6.18) the DSM_A seems more accurate than the DSM_D, in fact for the former model the accuracies varies in the range of 10 m - 14 m, while the accuracies of the latter varies between 12 m and 25 m; Table 6.15 contains the absolute frequencies of the classes.

		Aspect							
		N	NW	W	SW	S	SE	E	NE
Gradient	0 - 16°	2691	2690	2719	2129	2114	1724	2189	2177
	16° - 29°	2393	2449	2821	2151	2049	1587	2011	1854
	29° - 43°	2310	2513	3003	2394	2137	1511	2048	1873
	> 43°	3263	2843	3843	2803	2851	1971	2917	2532

Table 6.15: Area 2: absolute frequencies

		Aspect							
		N	NW	W	SW	S	SE	E	NE
Gradient	0 - 16°	10.69	13.28	10.20	10.87	10.01	9.75	9.93	10.21
	16° - 29°	10.63	10.66	10.36	11.12	10.59	10.49	10.69	11.27
	29° - 43°	10.83	11.31	10.86	10.99	11.42	11.84	11.72	12.39
	> 43°	13.51	13.04	12.30	12.68	12.38	12.53	12.99	14.05

Table 6.16: DSM_A: class standard deviation values [m]

		Aspect							
		N	NW	W	SW	S	SE	E	NE
Gradient	0 - 16°	13.57	13.18	15.59	16.34	14.99	14.61	12.86	13.79
	16° - 29°	13.30	15.48	17.72	24.95	17.88	15.69	12.93	12.54
	29° - 43°	13.55	14.45	18.39	25.46	17.67	15.55	13.08	12.68
	> 43°	13.64	15.78	16.95	21.13	15.33	14.03	12.83	14.36

Table 6.17: DSM_D: class standard deviation values [m]

		Aspect							
		N	NW	W	SW	S	SE	E	NE
Gradient	0 - 16°	10.40	12.90	10.55	10.78	10.01	10.11	9.69	10.64
	16° - 29°	10.70	11.03	10.36	13.24	10.87	10.78	10.15	10.56
	29° - 43°	10.91	10.81	10.74	11.66	11.41	11.43	11.43	11.76
	> 43°	12.81	12.64	12.19	12.60	11.98	11.90	12.37	13.12

Table 6.18: DSM_{AD}: class standard deviation values [m]

6.5.2 Fusion tests

The same fusion tests applied to the data of the first area were applied to this second region. Knowing that these ascending and descending datasets were obtained from the same COSMO-SkyMed images used to generate the first area dataset, the fusion results should confirm the one obtained before (see Section 6.4.2).

Fusion using the standard deviation from the LiDAR DSM comparison: this fusion was done using, as weights, the accuracies obtained in the external validation step.
The ascending DSM weights was 8.70 m while the descending DSM one was 11.54 m; the DSM resulting from the fusion step had an accuracy of 8.38 m (computed with LE95 of 21.37 m).

Fusion using the accuracies from the slope gradient and aspect classification: this fusion method uses as weight the accuracies of the gradient and aspect classes used in the ANOVA analysis. The merged DSM has an accuracy of 8.18 m (LE95 of 20.96 m); also in this test area this method is effective as the one that uses as unique accuracy value the one obtained from the LiDAR comparison.

6.5.3 ANOVA and fusion of the data filtered on the coherence value

As done for the first area, the points with coherence value lower than 0.85 were excluded from the interpolation step; as before three DSMs were created: the ascending one ($DSM_{A-0.85}$) from the interpolation of 75041 points (on the left in Figure 6.15), the descending one ($DSM_{D-0.85}$) from the interpolation of 21522 points (on the left in Figure 6.15) and the $DSM_{AD-0.85}$ (Figure 6.16) from the interpolation of the previous datasets merged.
The external validation, performed by comparing the DSMs with the LiDAR one, produced the following results in a LE95 approach:

- $DSM_{A-0.85}$: accuracy 8.10 m; LE95 21.30 m
- $DSM_{D-0.85}$: accuracy 11.08 m; LE95 33.20 m
- $DSM_{AD-0.85}$: accuracy 7.98 m; LE95 22.19 m

The ANOVA analysis was carried on also on these DSMs.

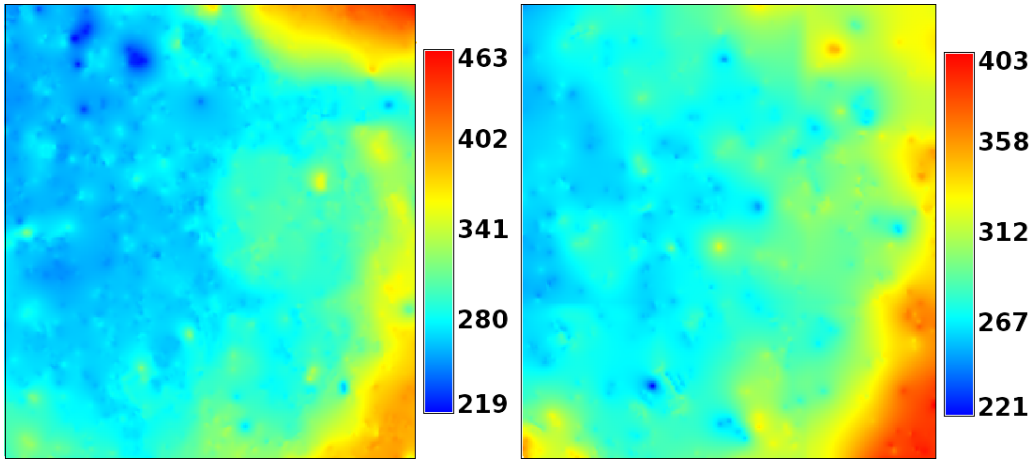

Figure 6.15: Second area: $DSM_{A-0.85}$ (left) and $DSM_{D-0.85}$ (right)

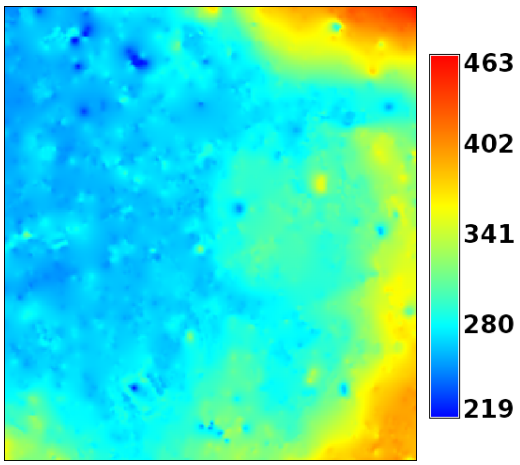

Figure 6.16: Second area: $DSM_{AD-0.85}$

ANOVA: the analysis was carried on as in the other test, using the same slope gradient and aspect classification (see Figure 6.13 and Figure 6.14); Table 6.20, 6.21 and 6.22 contain the accuracies of the classes, the absolute frequencies, depending only on the slope gradient and aspect classification are the same as in Table 6.15.
The ANOVA results (Table 6.19) show that the three DSMs have dependencies on both the slope gradient and the aspect; as for the first area, comparing the two ANOVA results (before and after the coherence filtering) it is possible to conclude that they are similar, a part the slope gradient dependence of the

ascending DSM that decreases after the filtering.

	$\mathbf{DSM_{A-0.85}}$	$\mathbf{DSM_{D-0.85}}$	$\mathbf{DSM_{AD-0.85}}$
H_0: slope gradient has no influence			
Degrees of freedom	v_1=3,v_2=21		
F_{teo} with $\alpha = 0.01$	4.87		
F_{teo} with $\alpha = 0.05$	3.07		
F_{emp}	35.92	9.80	24.37
H_0: slope aspect has no influence			
Degrees of freedom	v_1=7,v_2=21		
F_{teo} with $\alpha = 0.01$	3.64		
F_{teo} with $\alpha = 0.05$	2.49		
F_{emp}	11.15	97.45	9.07

Table 6.19: Filtered data: ANOVA results

		Aspect							
		N	NW	W	SW	S	SE	E	NE
Gradient	0 - 16°	9.94	12.54	9.26	9.57	8.74	8.62	9.09	9.37
	16° - 29°	9.39	9.21	9.61	9.53	9.83	9.35	8.53	9.15
	29° - 43°	9.86	9.85	9.88	9.74	10.23	10.31	10.60	11.38
	> 43°	12.36	11.70	11.11	11.20	10.95	10.85	11.67	12.80

Table 6.20: $DSM_{A-0.85}$: class standard deviation values [m]

		Aspect							
		N	NW	W	SW	S	SE	E	NE
Gradient	0 - 16°	14.64	13.90	17.35	18.63	16.45	16.24	13.42	14.70
	16° - 29°	13.92	16.98	21.43	31.30	22.36	18.27	13.75	13.69
	29° - 43°	14.28	16.11	22.50	33.51	22.06	17.80	13.11	12.63
	> 43°	12.41	15.38	19.25	27.61	19.64	15.63	12.07	13.39

Table 6.21: $DSM_{D-0.85}$: class standard deviation values [m]

		Aspect							
		N	NW	W	SW	S	SE	E	NE
Gradient	0 - 16°	9.96	12.21	9.33	9.37	8.73	8.69	8.69	9.72
	16° - 29°	9.48	9.52	9.37	11.88	9.47	9.26	9.44	9.94
	29° - 43°	9.87	9.73	9.81	10.09	10.07	10.07	10.37	10.86
	> 43°	12.04	11.49	11.12	11.23	10.62	10.64	11.11	12.02

Table 6.22: $DSM_{AD-0.85}$: class standard deviation values [m]

Fusion tests: the results obtained from the fusion confirms the ones obtained for the first region. The merged DSM, obtained using as weights the accuracies from the LiDAR comparison, has an accuracy of 8.16 m (LE95 20.63 m), while the one obtained using variable weights, in function of terrain morphology, has an accuracy of 7.95 m (LE95 20.15 m).

6.6 Fusion results: summary

Different fusion approach were tried on the radargrammetric derived datasets available, they are reported in Table 6.23 to better allow their comparison.

	Accuracy (m)	
Model	**Area 1**	**Area 2**
DSM_A	7.56	8.70
DSM_D	9.65	11.54
DSM_{AD}	7.24	8.70
Fusion with constant vertical accuracy from the LiDAR DSM comparison	6.87	8.38
Fusion with variable vertical accuracy from gradient and aspect classes	6.80	8.18
$DSM_{A-0.85}$	7.37	8.10
$DSM_{D-0.85}$	9.20	11.08
$DSM_{AD-0.85}$	6.77	7.98
Fusion with constant vertical accuracy from the LiDAR DSM comparison	7.04	8.16
Fusion with variable vertical accuracy from gradient and aspect classes	6.97	7.95

Table 6.23: Fusion summary

It is useful to remark that the ascending and descending data do not have the same accuracies, in fact the DSMs from ascending data (DSM_A) have accuracies around 11 m - 15 m for both the areas, while the descending generated ones (DSM_D) are less precise, in fact their accuracies are between 15 m and 26 m.
The DSMs were merged in various way: at first a fusion of the original data was tried, so the point-wise datasets were at first merged and then interpolated (DSM_{AD}); the accuracies of the resulting models varies from 7.24 m (first area) and 8.70 m (second area). These results proves that this kind of approach is an improvement with respect to the worse data (the descending ones) but it produce worst results than the ascending DSMs taken alone.
If other information are supplied, like a more accurate DSM, another fusion choice is the one based on the accuracies from the slope gradient and aspect classification or the use of an unique accuracy value obtained from the comparison with the more accurate DSM. The former method, proved to be an efficient choice for the SRTM DSM (see Section 5.3.5), is suggested if the morphological classes obtained after the gradient and aspect classification have different accuracies; the latter is useful if the accuracies belonging to different morphology classes have the order of magnitude; in this situation the two methods provide similar results, so the one based on a constant error map is the most suitable, also because it is easier to implement.

Conclusions

The main topic of this thesis consisted in the analysis of digital surface models (DSMs); in particular a validation and fusion procedure was studied, implemented and tested on two globally available models, the SRTM and the ASTER ones; in the last chapter the analysis was also performed on the data obtained from a radargrammetric procedure. The assessment of the model accuracies was always made in comparison with a more accurate LiDAR DSM, taken as ground truth; for this reason Chapter 2 is dedicated on the analysis of LiDAR data and on the interpolation of the model used as reference.
Concerning the validation step, two different levels of investigation were considered and proved to be useful. In particular, the DSMs were validated at first internally by using three algorithms developed for the GRASS GIS software and then externally by comparing them with the most accurate LiDAR DSM; the former procedure helps in the outlier detection, while the latter allows for a reliable estimation of the model accuracy. Furthermore, before attempting the fusion step, a two ways ANOVA (ANalysis Of VAriance) was performed on the models to evaluate dependencies on the slope gradient and aspect.
Concerning the fusion step, which involved the SRTM and ASTER DSMs, two main methods were applied: a weighted average to improve the SRTM grid and a collocation approach to improve the ASTER one. The choice between the two different methods was driven by the different data characteristics of the two DSMs. On the radargrammetric data, instead, only the weighted average approach was tested.
In conclusion, the validation and the ANOVA procedures revealed to be useful tools in the data analysis and can be easily applied to different digital models; moreover they provide useful information also for the subsequent fusion step (e.g. the accuracies of the ANOVA classes). The validation step, in general, is necessary before attempting the data merging, mainly because knowing the accuracies of the models to be merged it is possible to choose the optimum fusion approach.
Concerning the SRTM and ASTER DSM fusion, the best approach consisted

in the SRTM grid improvement by means of a weighted average fusion, in particular using as error map the one containing the variable vertical accuracies from the ANOVA analysis. On the other hand, the collocation approach, which was used to improve the ASTER grid, did not provide as good results as expected: the implemented algorithm is time consuming and the covariance model strongly depends on the region morphology and so does the collocation prediction. Tests proved that the best results could be obtained where the SRTM model is more accurate than the ASTER one, that is mainly in flat areas; in other areas the fusion results were not an improvement with respect to the original ASTER model.
As already written, the availability of radargrammetric data, produced by COSMO-SkyMed stereo-couples, allowed other fusion tests, in this case, the models had the same characteristics and there was the need to find the best method to merge data from ascending and descending orbits.
Different approaches were tried, before and after the point-wise dataset interpolations. The best accuracies were obtained with the weighted average fusion of the interpolated models; since the use of the accuracies obtained from the LiDAR DSM comparison and the use of the ones from the ANOVA analysis provides similar results, the best choice is the former one, also because it is easier to implement than the ANOVA based one. In case more accurate models (such as the LiDAR one) are not available, the best merging method consists in the fusion of the point-wise datasets and their interpolation.
All in all, the obtained results confirm that the processing chain proposed in this thesis for the DSM validation and fusion can be successfully applied to different types of data with the obvious recommendation of choosing the proper analysis method according to the specific data characteristics.

Acknowledgements

This work was done in team with Ing. Maddalena Gilardoni within the ASI project: "On the Exploitation and Validation of COSMO-SkyMed Interferometric SAR data for Digital Terrain Modelling and Surface Deformation Analysis in Extensive Urban Areas (ID: 1441)"

I would like to thank Regione Lombardia, having provided the LiDAR raw dataset in the Como area and OGS, in particular Michela Vellico, for the LiDAR data preprocessing and for providing the TerraScan automatic and semi-automatic classification.

Thanks to Dr. Ing. Damiano Triglione for the help in modifying and updating r.outldetect and to Ing. Marco Negretti who made r.outldetect and r.outldetopt work within GRASS 5.4.1.

Thanks to the team of Geodesy and Geomatic Area at La Sapienza University of Rome, in particular to Andrea Nascetti, for providing the elaborated radargrammetric data.

Thanks also to Dr. Ing. Mirko Reguzzoni, he knows why.

Bibliography

F. Ackermann. Airborne laser scanning - present status and future expectations. *ISPRS Journal of Photogrammetry & Remote Sensing*, 54:64–67, 1999.

P. Audenino, L. Rognant, J.M. Chassery, and J.G. Planes. Fusion strategies for high resolution urban DEM. *IEEEISPRS Joint workshop on Remote Sensing and Data Fusion over Urban Areas*, pages 90–94, 2001.

G. Aumann, H. Ebner, and L. Tang. Automatic derivation of skeleton lines from digitized contours. *ISPRS Journal of Photogrammetry & Remote Sensing*, 46:259–268, 1991.

ACPA Australian Centre for Precision Agriculture. Vesper User Manual - Vesper 1.6. Technical report, Australian Centre for Precision Agriculture, 2006.

P. Axelsson. Processing of laser scanner data algorithms and applications. *ISPRS Journal of Photogrammetry & Remote Sensing*, 54:138–147, 1999.

B. Bajata, S. Rathb, and D. Blagojevica. Numerical method for uncertainty assessment of the topographic parameters derived from DEMs. *ISPRS Journal of Photogrammetry & Remote Sensing*, 54:199–214, 1999.

E. P. Baltsavias. Airborne laser scanning: basic relations and formulas. *ISPRS Journal of Photogrammetry & Remote Sensing*, 54:199–214, 1999a.

E. P. Baltsavias. A comparison between photogrammetry and laser scanning. *ISPRS Journal of Photogrammetry & Remote Sensing*, 54:83–94, 1999b.

E. P. Baltsavias. Airborne laser scanning: existing systems and firms and other resources. *ISPRS Journal of Photogrammetry & Remote Sensing*, 54: 164–198, 1999c.

F. Bretar and N. Chehata. Digital terrain model on vegetated areas: Joint use of airborne LiDAR data and optical images. *Photogrammetric Image Analysis*, 36(3/W49A):19–24, 2007.

M. A. Brovelli and M. Cannata. Digital terrain model reconstruction in urban areas from airborne laser scanning data: The method and the example of the town of Pavia (Northern Italy). *International Archives Photogrammetry & Remote Sensing*, 34:43–48, 2002.

M. A. Brovelli and S. Lucca. Inverse calibration of lidar filtering parameters: Ucode/grass integration. In *Proceedings of ISPRS Hannover Workshop "High-resolution Earth Imaging for Geospatial Information"*, 2009.

M. A. Brovelli and S. Lucca. Filtering LiDAR with GRASS: overview of the method and comparisons with Terrascan. *Rivista Italiana Telerilevamento*, 43(2):93–105, 2011.

M. A. Brovelli and S. Lucca. Comparison GRASS-LiDAR modules TerraScan with respect to vegetation filtering. *Applied Geomatics*, In print, 2012.

M. A. Brovelli, F. Sansó, and D. Triglione. Different approaches for outliers detection in digital terrain models and gridded surfaces within the GRASS geographic information system environment. *The International Archives of Photogrammetry and Remote Sensing*, 32:1–8, 1999.

M. A. Brovelli, M. Reguzzoni, F. Sansò, and G. Venuti. Modelli altimetrici del terreno per mezzo di interpolatori a spline. In *Bollettino della SIFET*, volume Supplemento speciale al n.2/2001, pages 55–71. 2001.

M. A. Brovelli, M. Cannata, and U. M. Longoni. LiDAR data filtering and DTM interpolation within GRASS. *Transaction in GIS*, 8(2):155–174, 2004.

P. Capaldo, M. Crespi, F. Fratarcangeli, A. Nascetti, and F. Pieralice. DSM generation from high resolution COSMO-SkyMed imagery with radargrammetric model. In *Proceedings of ISPRS Hannover Workshop - High-Resolution Earth Imaging for Geospatial Information*, 2011a.

P. Capaldo, M. Crespi, F. Fratarcangeli, A. Nascetti, and F. Pieralice. High-Resolution SAR radargrammetry: a first application with COSMO-SkyMed SpotLight imagery. 8:1100–1104, 2011b.

M. Crespi, F. Fratarcangeli, F. Giannone, and F. Pieralice. SISAR: a rigorous orientation model for synchronous and asynchronous pushbroom sensors imagery. In *ISPRS Hanover Workshop 2007: High-Resolution Earth Imaging for Geospatial Information*, 2007.

M. Crespi, P. Capaldo, , F. Fratarcangeli, A. Nascetti, and F. Pieralice. DSM generation from very high optical and radar sensors: problems and potentialities along the road from the 3D geometric modelling to the surface model. In *Geoscience and Remote Sensing Symposium (IGARSS), IEEE International*, pages 3596–3599, 2010.

M. Crosetto and F. P. Aragues. Radargrammetry and SAR interferometry for DEM generation: validation and data fusion. In *Proceedings of CEOS SAR Workshop, ESA-CNES, Toulouse, France*, 1999.

G. W. Davidson and R. Bamler. Multiresolution phase unwrapping for SAR interferometry. *IEEE Transactions on Geoscience and Remote Sensing*, 37: 163–174, 1999.

N. El-Sheimy, C. Valeo, and H. Ayman. *Digital terrain modeling - Acquisition, Manipulation, and Application.* 2005.

T. G. Farr, P. A. Rosen, E. Caro, Crippen R., R. Duren, S. Hensley, M. Kobrick, M. Paller, E. Rodriguez, L. Roth, D. Seal, S. Shaffer, J. Shimada, and J. Umland. Interferometric SAR phase unwrapping using Green's formulation. *Reviews of Geophysics*, 45, 2007.

G. Fornaro, G. Franceschetti, and R. Lanari. Interferometric SAR phase unwrapping using Green's formulation. *IEEE Transactions on Geoscience and Remote Sensing*, 34:720–727, 1996.

P. Gamba, F. Dell'Acqua, and B. Houshmand. Comparison and fusion of lidar and infsar digital elevation models over urban areas. *International Journal of Remote Sensing*, 24:4289–4300, 2003.

G. Goncalves, P. Julien, S. Riazanoff, and B. Cervelle. Preserving cartographic quality in DTM interpolation from contour lines. *ISPRS Journal of Photogrammetry & Remote Sensing*, 56:210–220, 2002.

T. Guo-an, J. Strobl, G. Jian-ya, Z. Mu-dan, and C. Zhen-jiang. Evaluation on the accuracy of digital elevation models. *Journal of Geographical Science*, 11:209–216, 2001.

M. Hahn and F. Samadzadegan. Integration of DTMs using wavelets. *The International Archives of Photogrammetry and Remote Sensing*, 32:90–96, 1999.

T. Hind, J. Parrot, and R. Alvarez. DEM generation by contour line dilation. *Computers & Geosciences*, 25:775–783, 1999.

ISO/TC211. Text for DIS 19113, Geographic information - Quality principles, as sent to ISO Central Secretariat for issuing as Draft International Standard. Technical report, ISO/TC 211, 2008.

ASI Italian Space Agency. COSMO-SKyMed System Description & User Guide. Technical report, Italian Space Agency (ASI), 2011.

D. James. Fusing LiDAR and IFSAR DEMs: a seven step methodology. Technical report, Topographic Engineering Center ERDC, 2003.

W. Karel and K. Kraus. Quality Parameters of Digital Terrain Models. *EuroSDR Publication*, 2007.

W. Karel, N. Pfeifer, and C. Briese. DTM quality assessment. *International Archives Photogrammetry & Remote Sensing*, 36:7–12, 2006.

W. Knopfle, G. Strunz, and A. Roth. Mosaiciing of digital elevation models derived by SAR interferometry. *IAPRS "GIS-between Vision and Applications"*, 32:306–313, 1998.

K. R. Koch. *Parameter Estimation and Hypothesis Testing in Linear Models*. Springer, 1997.

J. S. Lee. Digital Image Enhancement and Noise Filtering by Use of Local Statistics. *IEEE Transactions on Pattern Analysis and Machine Intelligence*, 2:165–168, 1980.

Z. Li, Q. Zhu, and C. Gold. *Digital terrain modeling - Principles and Methodology*. 2005.

A. Lopes, R. Touzi, and E. Nezry. Adaptive Speckle Filters and Scene Heterogeneity. *IEEE Transactions on Geoscience and Remote Sensing*, 28: 992–1000, 1990.

S. Lucca. Calibrazione inversa dei parametri del filtraggio di dati LiDAR: integrazione UCODE-GRASS e verifiche sperimentali. Master's thesis, Politecnico di Milano, 2008.

R. Ludwig and P. Schneider. Validation of digital elevation models from SRTM X-SAR for applications in hydrology modeling. *ISPRS Journal of Photogrammetry & Remote Sensing*, 60:339–358, 2006.

L. Matikainen, H. Kaartinen, and J. Hyyppa. Classification tree based building detection from laser scanner and aerial image data. In *ISPRS Workshop on Laser Scanning and SilviLaser*, volume 36, pages 280–287, 2007.

METI/ERSDAC, NASA/LPDAAC, and USGS/EROS. ASTER Global DEM validation - Summary report. Technical report, ASTER GDEM Validation Team, 2009.

E. M. Mikhail and J. S. Bethel. *Introduction to modern photogrammetry.* 2001.

G. C. Miliaresis. The landcover impact on the aspect/slope accuracy dependence of the SRTM-1 elevation data for the Humboldt range. *Sensors*, 8: 3134–3149, 2008.

G. C. Miliaresis and V.E. P. Charalampos. Vertical accuracy of the SRTM DTED level 1 of Crete. *ISPRS Journal of Applied Earth Observation and Geoinformation*, 7:49–59, 2005.

H. Mitasova and M. Neteler. GRASS as Open Source Free Software GIS: Accomplishments and Perspectives. *Transaction in GIS*, 8(2):145–154, 2004.

H. Papasaika, D. Poli, and E. Baltsavias. Fusion of digital elevation models from various data sources. In *IEEE, The International Conference on Advanced Geographic Information Systems & Web Services*, 2009.

E. P. Poeter and M. C. Hills. Documentation of UCODE, a computer code for universal inverse modelling. Technical report, USGS, 1998.

E. P. Poeter, M. C. Hills, E. R. Banta, S. Mehl, and S. Christensen. UCODE_2005 and six other computer codes for universal sensitivity analysis, calibration and uncertainty evaluation. *Modeling Techniques, Section A. Ground Water*, 6(11), 2008.

B. Rabus, M. Eineder, A. Roth, and Bamler R. The shuttle radar topography mission - a new class of digital elevation models acquired by spaceborne radar. *ISPRS Journal of Photogrammetry & Remote Sensing*, 57:241–262, 2003.

H. Raggam, K. Gutjahr, R. Perko, and M. Schardt. Assessment of the Stereo-Radargrammetric Mapping Potential of TerraSAR-X Multibeam Spotlight Data. *IEEE Geoscience and Remote Sensing*, 48:971–977, 2010.

A. Roth, W. Knopfle, G. Strunz, M. Lehner, and P. Reinartz. Towards a global elevation product: combination of multi-source digital elevation models. In *Proceedings of Joint International Symposium on Geospatial Theory, Processing and Applications*, 2002.

F. Sansó. *Statistical methods in physical geodesy.* Springer, 1986.

F. Sansó. *Il trattamento statistico dei dati*, chapter 5: L'inferenza per le stime della teoria dei minimi quadrati. Clup, 1993.

F. Sansó, C. C. Tscherning, and G. Venuti. A theorem of insensitivity of the collocation solution to variations of the metric of the interpolation space. In *Geodesy Beyond 2000. The challenges of the First Decade, IAG General Assembly*, pages 233–240, 1999.

J. Secord and A. Zakhor. Tree detection in urban regions using aerial LiDAR and image data. *Geoscience and Remote Sensing Letters*, 4:196–200, 2007.

Z. Shi and B. F. Ko. A Comparison of Digital Speckle Filters. In *Geoscience and Remote Sensing Symposium, IGARSS '94. Surface and Atmospheric Remote Sensing: Technologies, Data Analysis and Interpretation*, 1994.

G. Sithole. *Segmentation and classification of Airborne Laser Scanner data.* PhD thesis, ITC-Enschede, Nederland, 2005.

E. Steinle and T. Vogtle. Automated extraction and reconstruction of buildings in laserscanning data for disaster management. *Automatic extraction of mad-made objects from aerial and space images (III)*, pages 309–318, 2001.

F. Tarsha-Kurdi, T. Landes, P. Grussenmeyer, and E. Smigiel. New approach for automatic detection of buildings in airborne laser scanner data using first echo only. In *Symposium of ISPRS Commission III Photogrammetric Computer Vision PCV '06*, volume 36, pages 20–22, 2006.

TerraSolid. TerraScan Users Guide. Technical report, TerraSolid Limited, 2011.

T. Toutin. Error Tracking of Radargrammetric DEM from RADARSAT Images. *IEEE Transactions on Geoscience and Remote Sensing*, 37:2227–2238, 1999.

T. Toutin. Three-Dimensional Topographic Mapping With ASTER Stereo Data in Rugged Topography. *IEEE Transactions on Geoscience and Remote Sensing*, 40:2241–2247, 2002a.

T. Toutin. Impact of terrain slope and aspect on radargrammetric DEM accuracy. *ISPRS Journal of Photogrammetry & Remote Sensing*, 57:228–240, 2002b.

T. Toutin. ASTER DEMs for geomatic and geoscientific applications: a review. *International Journal of Remote Sensing*, 29:1855–1875, 2008.

T. Toutin and R. Chenier. 3D radargrammetric modeling of RADARSAT-2 Ultrafine Mode: preliminary results of the geometric calibration. *IEEE Geoscience and Remote Sensing Letters*, 2009.

T. Toutin and L. Gray. State-of-the-art of elevation extraction from satellite SAR data. *ISPRS Journal of Photogrammetry & Remote Sensing*, 55:13–33, 2000.

D. Tovari and N. Pfeifer. Segmentation based robust interpolation - a new approach to laser data filtering. In *Proceedings of the ISPRS Workshop Laser scanning*, volume 36, pages 79–84, 2005.

D. Triglione. Metodi e algoritmi di validazione di terreni digitali con GRASS. Master's thesis, Politecnico di Milano, 1999.

B. Vrscaj, J. Daroussin, and L. Montanerella. SRTM as a possible source of elevation information for soil-landscape modelling. In R. J. Peckham and G. Jordan, editors, *Digital terrain modelling - Developement and applications in a policy support environment*, pages 99–120. Springer, 2007.

H. Wackernagel. *Multivariate Geostatistics*. Springer, 1998.

L. Wald. Some terms of reference in data fusion. *IEEE Transactions on Geoscience and Remote Sensing*, 37:1190–1193, 1999.

A. Wehr and U. Lohr. Airborne laser scanning - an introduction and overview. *ISPRS Journal of Photogrammetry & Remote Sensing*, 54:68–82, 1999.

R. Welch, T. Jordan, H. Lang, and H. Murakami. ASTER as a Source for Topographic Data in the Late 1990s. *IEEE Transactions on Geoscience and Remote Sensing*, 36:1282–1289, 1998.

B. M. Whelan, A. B. McBratney, and B. Minasny. VESPER 1.5 - Spatial prediction software for precision agriculture. In *Proceedings of the 6th International Conference on Precision Agriculture*, 2002.

Y. Yu and S. T. Acton. Speckle Reducing Anisotropic Diffusion. *IEEE Transactions on Image Processing*, 11:1260–1270, 2002.